A detailed combined experimental and theoretical study on dimethyl ether/propane blended oxidation

Validated Kinetic Model for the Oxidation of Dimethyl Ether/Propane Blends: Rapid Compression Machine Experiments and Pressure-Dependent Rate Calculations

Enoch E. Dames[a], Andrew S. Rosen[a], Bryan W. Weber[b], Connie W. Gao[a], Chih-Jen Sung[b], William H. Green[a]*

[a]*Department of Chemical Engineering, Massachusetts Institute of Technology, Cambridge, MA, USA*

[b]*Department of Mechanical Engineering, University of Connecticut, Storrs, CT, USA*

Abstract: In this work, a binary fuel model for dimethyl ether (DME) and propane is developed, with a focus on engine-relevant conditions (10–50 atm and 550–2000 K). New rapid compression machine (RCM) data are obtained for the purpose of further validating the binary fuel model, identifying reactions important to low temperature propane and DME oxidation, and understanding the ignition-promoting effect of DME on propane. It is found that the simulated RCM data for DME/propane mixtures is very sensitive to the rates of C_3H_8 + OH, which acts as a radical sink relative to DME oxidation, especially at high relative DME concentrations. New rate evaluations are conducted for the reactions of C_3H_8 + OH = *products* as well as the self-reaction of methoxymethyl peroxy (in competition with RO_2 = QOOH isomerization) of $2CH_3OCH_2O_2$ = *products*. Accurate phenomenological rate constants, $k(T,P)$, are computed by RRKM/ME methods (with energies obtained at the CCSD(T)-F12a/cc-pVTZ-F12 level of theory) for several radical intermediates relevant to DME. The model developed in this work (120 species and 700 reactions) performs well against the experimental targets tested here and is suitable for use over wide range of conditions. In addition, the reaction mechanism generator software, RMG, is used to explore cross-reactions between propane and DME radical intermediates. These cross-reactions did not have a significant effect on simulations of the conditions modeled in this work, suggesting that kinetic models for high- and low-reactivity binary fuel mixtures may be assembled from addition of their corresponding submodels and a small molecule foundation model.

Keywords: dimethyl ether, propane, binary fuel blends, kinetic model, rapid compression machine, low temperature combustion

*Corresponding author: William H. Green, whgreen@mit.edu

Commented [AR1]: We can only have a maximum of 6 keywords. Jackie added in "binary fuel blends" so we need to figure out which one to remove. Maybe low T combustion? Not sure.

1. Introduction

Dimethyl ether (DME, CH_3OCH_3) is widely known to be a good transportation fuel, in part because it can act as a drop-in replacement for diesel while reducing soot, carbon monoxide (CO), and unburned hydrocarbon emissions [1]. As a fuel additive to conventional fossil fuel in internal combustion engines, DME has the potential to greatly reduce particulate (soot) formation [2]. Fuel additives have been studied for their potential to control ignition timing of homogeneous-charge compression-ignition (HCCI) engines, stratified-charge compression-ignition (SCCI) engines, and reactivity-controlled compression-ignition (RCCI). In combination with intelligent fuel mixture and composition design, these advanced engines offer the prospect of cleaner burning and higher thermal efficiencies [3][4][5][6]. Many of these future engines may rely on dual fuel systems or those with adjustable concentrations of fuel additives that advance combustion [7]. However, these same engines will also rely more heavily on fundamental knowledge of the underlying combustion chemistry that drives the low temperature autoignition of fuel mixtures with both high- and low-reactivity components.

The promoting effect of DME on fuels such as methane (CH_4) under conditions of both low and high temperature combustion has been studied in some detail [8][9]. Under high temperature regimes, the rapid build-up of radicals formed from DME promotes methane ignition, as noted by Chen et al. [8]. Although there is a nonlinear ignition enhancement, the laminar flame speeds of DME/methane mixtures are linearly proportional to the DME fraction [8]. The ignition promoting effect of DME on high-octane fuels is of particular importance for controlling ignition timing in internal combustion engines. Fundamental kinetic studies of fuel blends and quantification of ignition enhancement may therefore be useful in modeling, optimizing, and ultimately developing more advanced and cleaner combustion engines.

Dual-fuel combustion embodies a conceptually novel approach to internal combustion engine technology, relying on mixtures of high-octane fuels and high-cetane fuels as well as their synergistic combustion characteristics in order to achieve high thermal efficiencies. These engines can be made from retrofitted diesel engines with modified intake manifolds to allow for high reactivity vapor fuel mixing into the engine piston. For example, recent work [4] has identified a mixture of 20% DME with 30% propane (by mass) in concert with diesel fuel combustion, resulting in over 50% brake thermal efficiency (BTE) in a modified rail diesel engine, compared

to a baseline BTE of 37%. The authors found that propane substitution delayed DME's early autoignition and shifted the combustion process closer to top dead center and that autoignition of the fumigated fuels led to the diesel fuel igniting much earlier compared to the baseline diesel condition due to an increase in the bulk cylinder temperature [4]. In addition, DME has been investigated as an additive for ignition control in HCCI engines [1][7]. The combustion kinetics of fuel blends has also received wide attention in efforts to understand the oxidation and pyrolysis of primary reference fuels [10]. As a result, studies of DME combustion abound in the literature. Recent work (see Table 1) includes studies of premixed and non-premixed flames, homogeneous ignition experiments, and studies in homogeneous flow reactors.

The uncertainties in low temperature (400–900 K) DME oxidation kinetics primarily involve the first and second O_2 additions (typically denoted R + O_2 = RO_2 and QOOH + O_2 = O_2QOOH, respectively) to radical derivatives of DME as well as the fate of ketohydroperoxide, HO_2CH_2OCHO (hydroperoxymethylformate), all of which can serve to generate OH radicals, thereby promoting heat release and ignition. Tomlin et al. [11] have clearly illustrated the need for further work in this area by pointing out that several literature models such as [12][13][14] fail to accurately reproduce earlier rapid compression machine (RCM) ignition delay time measurements of DME [15]. In particular, Tomlin et al. [11] highlight the need for accurate pressure dependent descriptions for both first and second O_2 additions to DME radical derivatives, and subsequent OH forming pathways. Thus, a number of more recent studies have been published that include detailed rate theory calculations for these reactions. Notably, Eskola et al. [16] performed a combined theoretical and experimental study for both first and second O_2 additions. The subsequent corresponding $CH_3OCH_2O_2$ (RO_2) = CH_2OCH_2OOH (QOOH) isomerization step is determined to be faster than those used in previous models [17][18], suggesting that the O_2 addition to QOOH may play a more important role than previously thought [16]. The rate theory calculations performed by Eskola et al. [16] resulted in a total of nine phenomenological rates, including four well-skipping reactions. The rate of the RO_2 = QOOH isomerization is near its high-pressure limit at 1 bar, while the rate of the important QOOH decomposition to $2CH_2O$ + OH is at its high-pressure limit at 10 bar. Rodriguez et al. [19] also recently calculated high-pressure limit rates on a G4 potential energy surface for the reactions $CH_3OCH_2O_2$ = CH_2OCH_2OOH and $CH_3OCH_2O_2$ = CH_3OCHO + OH. The same authors conducted atmospheric-pressure jet-stirred reactor (JSR) experiments for varying equivalence ratios, measuring a number of intermediate and

product species profiles using gas chromatography and cavity ring-down spectroscopy. Rodriguez et al. [19] noted that the use of both the DME models of Zhao et al. [20] and Burke et al. [9] overestimate the DME reactivity in the low-temperature region. Thus, Rodriguez et al. [19] assembled a new model which satisfactorily reproduces their measured species profiles in addition to a number of higher-pressure experiments, including other JSR data at 10 atm [21], plug flow reactor (PFR) data at 12.5 atm [18], and shock tube data ranging from 12 bar to 40 bar [9,22,23]. Finally, Burke et al. [9] computed pressure-dependent rates for the unimolecular decomposition of CH_3OCH_2, by performing Quantum-Rice-Ramsperger-Kassel (QRRK) calculations with a modified strong-collisional model for energy transfer, and energies obtained at the CBS-QB3 level of theory.

Propane (C_3H_8) has also been studied extensively, and its combustion had been reviewed in several studies, including those by Simmie [24] and Westbrook and Dryer [25]. Thus, only select previous works are noted briefly, which are relevant to this work. Of particular interest to this work is the study by Gallagher et al. [26], who measured pure propane overall ignition delay times in a rapid compression machine for variable equivalence ratio. In addition, the low temperature chain branching pathways (involving the first and second O_2 additions) have been studied using high-level electronic structure and rate theory methods by Goldsmith et al. [27]. Although not tested against global experimental measurements (e.g., ignition delay times) in a detailed kinetic model, individually computed rates were compared with those available in the literature. More recently, Merchant et al. [28] conducted a study on the first stage ignition of propane, using the elementary rates computed by Goldsmith et al. [27]. With a focus on deriving simple analytical solutions that can reliably predict first-stage ignition delay time, Merchant et al. [28] discussed in depth the roles of both OH and HO_2 radicals on the low-temperature autoignition behavior of propane.

Fundamental combustion studies on DME/hydrocarbon mixtures have also been recently performed, albeit to a lesser extent than for each individual component. Hu et al. [29] have studied DME/propane autoignition at engine-relevant pressures (20 bar) by measuring ignition delay times behind reflected shock waves at high temperatures (1100–1500 K). Burke et al. [9] performed a combined experimental and modeling study of DME/CH_4 mixtures between 600–1600 K and 7–41 atm for varying fuel equivalence ratios. The authors performed rate theory calculations to elucidate the pressure dependent nature of the unimolecular decomposition of the CH_3OCH_2 radical, finding that this chemistry, in addition to pressure dependent low temperature DME

chemistry adopted from Yamada et al. [30], resulted in improvements in model agreement with various experimental data compared to modeling with only pressure independent expressions. Burke et al. [9] also pointed out the strong promoting effect small amounts of DME can have on overall ignition delays of 20:80 blends (by mole) of DME:CH_4 [30]. This promoting effect is attributed to the overall weaker C–H bonds of DME compared to that of methane.

Although reactions between dual fuel derivatives/intermediates may exist under engine conditions, no current model incorporating both DME and propane reaction kinetics includes these fuel intermediate cross-reactions. Most models of fuel blends do not contain any direct cross-reactions between the first intermediate radicals produced during oxidation/pyrolysis, although some exceptions do exist. In a model of gasoline surrogate components, Mehl et al. [10] added cross-reactions of alkyl and alkyl-peroxy radicals to account for interactions of various fuel components in the mixture, although their importance in determining various combustion characteristics was not discussed.

Thus, the first objective of this work is to investigate the capability of the Reaction Mechanism Generator (RMG) [31] to identify any reactions important to blended fuel combustion chemistry that do not exist in a pre-constructed base model from a simple concatenation of existing DME and propane mechanisms. Use of RMG in this manner can be especially valuable in the context of dual- or multi-component fuel mixtures given that many potentially important cross-reactions between fuel components may be readily missed or overlooked during manual (i.e., human) mechanism construction. The second objective of this work is to collect new experimental data in a rapid compression machine for the autoignition of binary DME/propane mixtures under engine-relevant conditions (a pressure of 30 bar and temperatures of 600–900 K). The third objective of this study is to conduct rate calculations and critical evaluations for several reactions important to the autoignition of DME and propane. These improved rate calculations are used to assemble a comprehensive model for the combustion of binary DME/propane mixtures under engine-relevant conditions (initial pressures of 1–60 bar and initial temperatures of 300–1500 K). This model is validated by comparison to a wide range of experimental targets, including literature data and the new data for DME/propane binary mixtures collected in this study. Finally, we investigate the non-linear promoting effect of DME on propane autoignition.

Table 1. Recent experimental studies of DME combustion with their corresponding experimental conditions, including temperature, pressure, equivalence ratio (ϕ), diluent, and residence time (t_{res}). Adapted from Rodriguez et al. [19].

Type of Experiment	Experimental Conditions	Reference
Jet-stirred reactor	T = 800–1300 K; P = 101–1013 kPa; ϕ = 0.2–2 in N_2; t_{res}= 0.1–1 s	Dagaut et al. 1996 [32]*
	T = 550–1100 K; P = 1013 kPa; ϕ = 0.2–1.0 in N_2; t_{res} = 1 s	Dagaut et al. 1998 [21]*
	T = 540–850 K; P = 101 kPa; ϕ = 0.5–2 in N_2; t_{res} = 1.5 s	Le Tan et al. 2015 [33]
	T = 550–1100 K; P = 107 kPa; ϕ = 0.25–2 in He, t_{res} = 2 s	Rodriguez et al. 2015 [19]*†
Plug flow reactor	T = 600–1500 K; P = 101 kPa; ϕ = 0.01–∞ in air	Alzueta et al. 1999 [34]
	T = 1080–1086 K; P = 101 kPa; ϕ = 0.5 in N_2; t_{res} = 0.1 s	Fischer et al. 2000 [17]
	T = 550–855 K; P = 1216–1825 kPa; ϕ = 0.7–4.2 in N_2; t_{res} = 1.8 s	Curran et al. 2000 [18]
	T = 513–973 K; P = 101 kPa; 340 ppm in 10% O_2; t_{res} = 2–4 s	Liu et al. 2001 [35]
	T = 490–750 K; P = 101 kPa; ϕ = 0.6 in He; t_{res} = 107 s	Guo et al. 2013 [36]
	T = 500–1200 K; P = 101 kPa; ϕ = 0.8–1.2 in Ar	Herrmann et al. 2013, 2014 [37][38]
	T = 739–902 K; P = 200–400 kPa; ϕ = 0.225–0.675 in N_2	Schönborn et al. 2014 [39]
	T = 555–585 K; P = 101 kPa; ϕ = 0.835 in air	Wada et al. 2013 [40]
	T = 500–1150 K; P = 101 kPa; ϕ = 0.2–1.6 in He/Ar; t_{res} = 0.19–2 s	Kurimoto et al. 2015 [41]
	T = 500–1150 K; P = 101 kPa; ϕ = 1 in Ar; t_{res} = 1.5 s	Wang et al. 2015 [42]
Shock tube	T = 650–1300 K; P = 1317–4053 kPa; ϕ = 1 in air	Pfahl et al. 1996 [22]*
	T = 1200–1600 K; P = 350 kPa; ϕ = 0.5–2 in Ar	Dagaut et al. 1998 [21]*
	T = 1175–1900 K; P = 161–666 kPa; ϕ = 0.5–3 in Ar	Cook et al. 2009 [43]*
	T = 1134–2015 K; P = 101–1010 kPa; ϕ = 1 in Ar	Tang et al. 2012 [44]*
	T = 1100–1500 K; P = 2000 kPa; ϕ = 0.5–2 in Ar	Hu et al. 2013 [29]†
	T = 1200–1600 K; P = 120–530 kPa; ϕ = 1 in Ar	Hu et al. 2013 [29]
	T = 697–1239 K; P = 2200–2300 kPa; ϕ = 0.5–1.5 in air/N_2	Li et al. 2013 [23]†
	T = 1300–1600 K; P = 152 kPa; 0.5–2% DME in Ar	Pyun et al. 2013 [45]*
	T = 900–1700 K; P = 122–1013 kPa; ϕ = 0.5–2 in H_2/Ar	Pan et al. 2014 [46]*
	T = 400–1160 K; P = 1111–3030 kPa; ϕ = 0.3–2 in air	Burke et al. 2015 [9]*
	T = 1000–1600 K; P = 122–2030 kPa; ϕ = 0.5–2 in Ar	Pan et al. 2015 [47]
RCM	T = 615–735 K; P = 1010–2010 kPa; ϕ = 0.43–1.5 in N_2	Mittal et al. 2008 [15]*†
	T = 630–1250 K; P = 1111–3030 kPa; ϕ = 0.3–2 in air	Burke et al. 2015 [9]*
Burner	premixed flame; P = 4 kPa; ϕ = 0.98–1.2 in Ar	Mcilroy et al. 2000 [48]
	premixed flame; P = 101 kPa; ϕ = 0.67–1.49 in air	Kaiser et al. 2000 [49]
	premixed flame; P = 2.67–4 kPa; ϕ = 1.2–1.68 in Ar	Cool et al. 2007 [50]
	premixed flame; P = 4 kPa; ϕ = 0.5–2 in Ar	Wang et al. 2008 [51]
	premixed flame; P = 4 kPa; ϕ = 1 in Ar	Xu et al. 2011 [52]
	premixed flame; P = 5 kPa; ϕ = 1.63 in Ar/CO_2	Liu et al. 2013 [12]*
	Single jet-wall stagnation flame; T = 298 K; P = 101 kPa; ϕ = 0.7–1.7 in air	Zhao et al. 2008 [20]
	Counterflow flame; T = 298 K; P = 101 kPa; ϕ = 0.7–1.7 in air	Wang et al. 2009 [53]
Spherical bomb	T = 295 K; P = 100 kPa; ϕ = 0.7–1.7 in air	Daly et al. 2001 [54]
	T = 298 K; P = 200–1000 kPa; ϕ = 0.6–1.7 in air	Qin and Ju 2005 [55]
	T = 298 K; P = 80–150 kPa; ϕ = 0.7–1.8 in air	Huang et al. 2007 [56]
	T = 293 K; P = 97 kPa; ϕ = 0.7–1.8 in air	Chen et al. 2009 [57]
	T = 298 K; P = 100–1000 kPa; ϕ = 0.7–1.6 in air	De Vries et al. 2011 [58]

*See the Supplementary Material for comparisons with the model of the present work.

†See main text for comparisons with the model of the present work.

Commented [JS2]: Indicate diluent and dilution level?

2. Experimental methods

The present experiments are conducted in a heated RCM at the University of Connecticut. The specifications of this RCM have been detailed in [59]. Briefly, the RCM is a single-piston, pneumatically-driven, hydraulically-stopped arrangement with compression times near 30 ms. The end of compression (EOC) temperature and pressure conditions, T_C and P_C respectively, are independently changed by varying the compression ratio, initial pressure, and initial temperature of the experiments. The piston in the reaction chamber is machined with specially designed crevices to suppress the roll-up vortex effect and promote homogenous conditions during and after compression [60].

The primary diagnostic on the RCM is the in-cylinder pressure, measured by a Kistler 6125C transducer coupled to a Kistler 5010B charge amplifier. The voltage from the charge amplifier is recorded by a National Instruments 9215 analog input device connected to a cDAQ 9178 chassis. The voltage is sampled at a rate of 100 kHz by a LabView VI and processed by a Python package called UConnRCMPy developed as part of this work; version 1.0.6 of UConnRCMPy was used in this study. The code for the data processing package is available on GitHub at https://github.com/bryanwweber/UConnRCMPy.

The compression stroke of the RCM brings the homogenous fuel/oxidizer mixture to the EOC conditions, and for suitable values of T_C and P_C, the mixture will ignite after some delay. For some combinations of mixture/pressure/temperature conditions, the ignition undergoes two stages. In these cases, the first-stage ignition delay (τ_1) is defined as the time from the EOC ($t = 0$) until the first peak in the time derivative of the pressure trace while the overall ignition delay (τ) is defined as the time from the EOC until the global maximum of the time derivative of the pressure trace, as shown in Figure 1. Cases undergoing single-stage ignition have their ignition delay defined the same as the overall ignition delay.

Each experimental condition is repeated at least five times to ensure repeatability of the data. As there is some random scatter present in the data, the standard deviation (σ) of the ignition delays computed from the runs at a particular condition is computed. In all cases, σ is less than 10% of the mean value of the ignition delay. Vertical error bars shown on plots of ignition delay measured in this study represent twice the standard deviation of the experiments at a given

condition; if no error bars are shown for data measured in this study, the error bars are approximately the same vertical dimension as the data point.

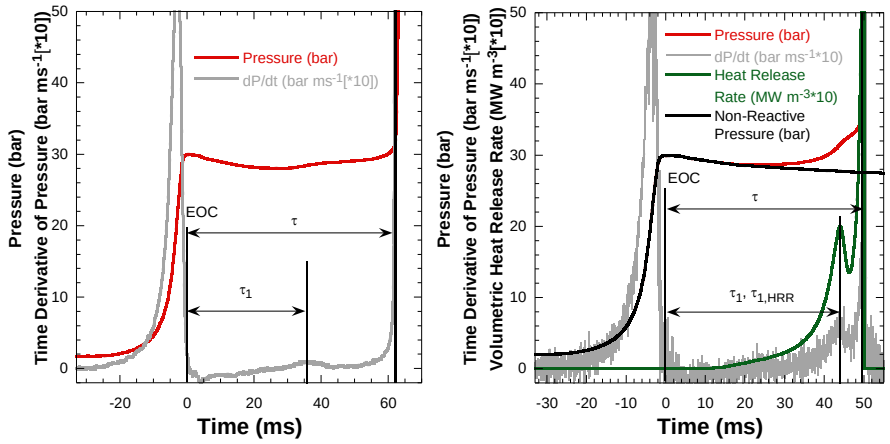

(a) (b)

Figure 1. Definitions of ignition delays, $\boldsymbol{\tau_1}$ and $\boldsymbol{\tau}$, in the RCM experiments and simulations. The conditions shown are for a $\boldsymbol{\phi = 2.0}$ mixture of propane in O_2/N_2 air. Figure (a) shows an experimental pressure trace with conditions: $\boldsymbol{P_0}$ = 1.7054 bar, $\boldsymbol{T_0}$ = 373 K, $\boldsymbol{P_C}$ = 30.02 bar, $\boldsymbol{T_C}$ = 759 K. Figure (b) shows a simulated pressure trace with conditions: $\boldsymbol{P_0}$ = 2.059 bar, $\boldsymbol{T_0}$ = 373 K, $\boldsymbol{P_C}$ = 29.98 bar, $\boldsymbol{T_C}$ = 726 K

In addition to the reactive experiments, non-reactive experiments are carried out to determine the influence of the machine-specific operating parameters on the experimental conditions. In these non-reactive experiments, O_2 in the oxidizer is replaced with N_2 to maintain a similar specific heat ratio but suppress oxidation reactions that lead to thermal runaway. If the pressure at the EOC of the non-reactive experiments matches that at the EOC of the reactive experiments, it is assumed that no substantial heat release has occurred during the compression stroke, and the temperature at the EOC (T_C) can be estimated by applying the adiabatic core hypothesis [61] and the isentropic relations between pressure and temperature during the compression stroke:

$$\ln\left(\frac{P_C}{P_0}\right) = \int_{T_0}^{T_C} \frac{\gamma}{\gamma - 1}\frac{dT}{T}$$

where P_0 is the initial pressure, T_0 is the initial temperature, γ is the temperature-dependent specific heat ratio, and the other variables are as defined previously. Due to the varying specific heat ratio, this formula is not integrated directly. Instead, the procedure described in Section 3.2.2 is used to model the compression stroke, and the simulated temperature at the EOC is taken as T_C. The uncertainty inherent in this calculation of T_C was estimated by Weber et al. [62] using a Monte Carlo method. Using the same method for the conditions of this experiment results in a typical uncertainty in the EOC temperature of $\pm 1\%$, similar to the values obtained in the work of Weber et al. [62]. Horizontal error bars are shown on the experimental data obtained in this study to represent this $\pm 1\%$ uncertainty.

The experiments in this work are carried out for the stoichiometric equivalence ratio for a range of relative fractions of DME/C_3H_8 in the fuel blends, from pure DME to pure C_3H_8. The oxidizer for all the stoichiometric experiments is a mixture of oxygen and nitrogen in the molar ratio of 1:3.76 (i.e., air). Furthermore, two additional conditions at ϕ = 0.5 and 2.0 are studied for pure C_3H_8, by holding the initial fuel mole fraction constant while adjusting the initial O_2 and N_2 mole fractions. All the experiments are conducted for an EOC pressure of $P_C = 30$ bar, and the EOC temperatures (T_C) range from 603 K to 902 K. The mixture conditions are summarized in Table 2, and the complete list of experimental data points collected in this study is presented in the Supplementary Material.

Table 2. Summary of RCM experimental conditions.

Molar proportions (purity of reactant)				
DME (99.8%)	C_3H_8 (99.72%)	O_2 (99.994%)	N_2 (99.999%)	Equivalence ratio (ϕ)
1	0	3	11.28	1.0
3	1	14	52.64	1.0
1	1	8	30.08	1.0
1	3	18	67.68	1.0
1	9	48	180.48	1.0
0	1	5	18.80	1.0
0	1	10	13.80	0.5
0	1	2.5	21.30	2.0

Mixtures are prepared in one of two mixing tanks, approximately 15 L or 17 L in volume. The larger tank is used for the reactive mixtures, while the smaller is used for the non-reactive

mixtures. Mixtures are made by first vacuuming the mixing tanks to an ultimate pressure less than 5 torr, then filling each gas sequentially into the mixing tank to the desired partial pressure. The filling is done at room temperature. Typical total pressures in each tank after filling range from 1700 torr to 2500 torr. The pressure in the mixing tanks during filling is monitored by an Omega Engineering MMA type static pressure transducer. This same transducer is used to measure the initial pressure of the reactants prior to a given experiment. In addition, the temperatures of the mixing tanks and reaction chamber are monitored by several K-type thermocouples; these thermocouples are also used as the control feedback for the heaters. After filling is complete, the heaters are switched on and the mixture is allowed 2 hours to come to steady state. The mixing tanks are also equipped with magnetic stir bars to enhance mixing and ensure homogeneity of the reactants.

3. Computational methods

3.1 *Rate theory calculations*

Electronic energies of all species studied in this work were determined at the CCSD(T)-F12a/cc-pVTZ-F12 [63–66] level of theory using Molpro [67]. Molecular geometries and force constants for species and saddle points were determined at the M08SO/MG3S [68][69] level of theory, utilizing QChem 4.1 [70]. A computational grid with 75 radial points and 434 angular points per radial point was used in the optimization and frequency calculations for all species. Frequencies were scaled by the recommended value of 0.983 [71]. Loose internal degrees of freedom for relevant adducts and transition states (i.e., hindered rotors) were treated separately by performing relaxed potential energy scans about the bond defining the internal rotor; these calculations were performed in Gaussian 03 [72] at the BMK/6-311+G(d,p) level of theory [73]. Reduced internal moments of inertia for all internal rotors were estimated at the $I^{(2,3)}$ level as defined by East and Radom [74]. Cantherm [75], a utility of RMG, was used for all TST and RRKM/Master Equation calculations, which were performed in the region of 0.001–100 atm in a nitrogen bath gas and varying temperatures based on the system (further discussed below). The master equation for energy transfer was solved using the chemically significant eigenvalue method, which is documented elsewhere [31,76]. Eckart tunneling corrections [77] were applied to all relevant reactions. All information pertaining to the calculations in this work can be found in the

Supplementary Material, including rate coefficients suitable for combustion modeling, in both Chebyshev and PLOG [78] formats.

The exponential down model for collisional energy transfer was adopted in this work. A temperature-dependent formulation was used for the average downward energy transferred per collision:

$$\langle \Delta E_d \rangle = \langle \Delta E_d \rangle_{300} \left(\frac{T}{300\ \mathrm{K}} \right)^n \mathrm{kJ/mol}$$

where $\langle \Delta E_d \rangle_{300}$ = 3.47 kJ/mol (for CH_2OCHO, OCH_2OCHO $HOCH_2O$, and CH_3OCH_2O) is adopted from a previous study of vinyl + O_2 [79], and the temperature exponent, n = 0.7, is adopted from previous studies for N_2 as the bath gas [80]. Lennard-Jones (LJ) collision diameters and well depths were estimated via the Joback method [81], which is based on the critical temperature and pressure of parent compounds. The method of corresponding states was subsequently used to estimate the LJ parameters [82] and is described in the context of RMG elsewhere [83].

3.2 Experiment simulation details

The Python 3.4 interface of Cantera [84] version 2.2.0 was used for all simulations in this work other than premixed laminar flame speed calculations, for which CHEMKIN-PRO [85] was used. In Cantera, state information about the system is stored in an instance of the Solution class. The Solution classes used in this study model simple, compressible systems and as such, require two independent intensive variables to fix the state. These instances of Solution classes are further utilized to compute the thermodynamic properties required to solve the ODE's representing the combustion systems studied here.

Cantera contains several objects used to model homogeneous reacting systems; the two used in this work are a Reservoir and an IdealGasReactor, which are subclasses of the generic Reactor class. The specific IdealGasReactor class is preferred over the generic Reactor class in this study because the energy equation is directly solved in terms of the temperature, instead of the enthalpy. A Solution object is installed in each Reactor subclass to manage the state information. The difference between the IdealGasReactor and the Reservoir is simply that the state (i.e., the pressure, temperature, and chemical composition) of the Solution in a Reservoir is fixed.

3.2.1 Shock tube simulations

Comparisons with experiments were made by assuming all shock tube ignition delay time measurements could be modeled as 0-D constant volume, adiabatic, batch reactors. This assumption is valid for experiments with negligible rates of change of pressure and temperature after the shock wave reflects off the tube endwall. We note however, that traditional shock tube ignition delay measurements for longer times (e.g., $\tau \geq 1$ ms) cannot reliably be modeled with the commonly utilized constant volume adiabatic batch reactors ('CONV') approach due to boundary layer and mixture attenuation effects that can reduce the observed τ compared to a corresponding ideal scenario. This behavior and best practices for minimizing its influence in both experiments and models have been discussed in great detail elsewhere [86]. We therefore recognize the reduced reliability in model-data comparisons for shock tube targets with a long τ. Unless otherwise noted, all shock tube ignition delay times were defined as the time to reach the simulated maximum slope of [OH] with respect to time after the arrival of the shock wave at the endwall. Simulations of species profiles measured behind reflected shock waves in DME/argon mixtures at the Stanford High Temperature Gasdynamics Laboratory [45] were conducted in the same manner as the τ simulations.

Sensitivity analyses for CONV simulations were performed in Cantera and with respect [OH]. In this work, normalized sensitivity coefficients of [OH] with respect to individual model rate parameters were computed as such:

$$S_{[\mathrm{OH}],k_i} = \frac{\partial \ln[\mathrm{OH}]}{\partial \ln k_i}$$

For all analyses, a user specified time was chosen (e.g., time of $\max(d[\mathrm{OH}]/dt)$, time at 50% fuel consumption, etc.). Sensitivity parameters were then further normalized to -1 or 1 based on the largest value by magnitude within the sensitivity array.

3.2.2 Rapid compression machines

As mentioned previously, non-reactive experiments were conducted to characterize the machine specific effect on the experiments in the RCM. A non-reactive experiment was conducted for each reported ignition delay in this study. The non-reactive pressure trace was combined with the reactive pressure trace to produce a combined pressure trace. For this, the reactive pressure trace was taken until the EOC, and the non-reactive pressure trace was taken after the EOC.

The combined pressure trace was used to compute a volume trace that could be applied to simulations to include any facility effects. The volume trace was created by initializing a Cantera Solution object at the initial pressure and temperature (P_0, T_0) of the reactor. After initialization, the initial mass-specific entropy (s_0) and density (ρ_0) were recorded. The initial volume (V_0) was arbitrarily taken to be equal to 1.0 m^3; the initial volume in this step was arbitrary so long as the initial volume utilized in the Reactor-based simulations described below was the same, since the velocity (i.e., the time rate of change of volume) enters the energy equation, not the volume itself.

The measured pressure at each data point (P_i) from the combined pressure trace was used with the previously recorded initial entropy (s_0) to set the state of the Solution object sequentially. At each data point, the volume was computed according to conservation of mass and the ideal gas law

$$V_i = V_0 \frac{\rho_0}{\rho_i}$$

where ρ_i was the density at each point computed by the Cantera Solution. This procedure effected an isentropic compression/expansion process, where compression occurred during the compression stroke and expansion occurred after the EOC. Note that the expansion process after the EOC was not a physical process; it was simply a modeling of the inherent experimental heat loss post-EOC. Moreover, this procedure accounted for the variation of the specific heat ratio as a function of temperature. Since there were no significant reactions that occurred during the compression stroke for the reactive experiments, or during and after the compression stroke for the non-reactive experiments, it was not necessary to solve the species and energy equations using an IdealGasReactor. After generation, the volume trace was downsampled to 20 kHz (from the experimental rate of 100 kHz) to reduce computational time of the simulations. This has no effect on the simulations, as confirmed by applying the full-rate (i.e., 100 kHz) volume trace to a simulation.

This volume trace was applied to a reactive simulation in Cantera as follows. A Solution object was initialized to the initial state of the reactor (P_0, T_0) and installed in an IdealGasReactor object (V_0 = 1.0 m^3). A Reservoir object was defined containing an arbitrary state and a Wall was installed between the Reservoir and the Reactor. The Wall allows the volume of the IdealGasReactor to vary with time and the effect of the Wall enters the energy equation through

Commented [ed3]: Bryan. Bill raises the point of rewording this a little to include rho_i = rho_o* P(t) * To / (T(t) * Po) and to further point out that T(t) must be computed, and P(t) is measured.

Commented [BW4R3]: I don't think it's necessary to show the derivation from the ideal gas law of the relationship between density and volume. I do think clarifying could be useful, especially because this particular computation step doesn't actually require the assumption of an isentropic process

the velocity term as the Wall does work on the IdealGasReactor. The velocity of the Wall was specified based on the first forward difference of the volume as a function of time.

Finally, the IdealGasReactor was installed in a ReactorNet, which implements the interface to the solver CVODES. CVODES is an adaptive-time-stepping solver, distributed as part of the SUNDIALS suite [87]. As the solver stepped towards the end time of the simulation, the state of the system was stored on each integrator time step, producing simulated pressure, volume, and temperature traces. Comparisons between the simulated pressure traces from Cantera and CHEMKIN-PRO show negligible differences.

Simulations were conducted for two purposes – to determine the temperature at the EOC, T_C, and to compute the simulated ignition delay. The temperature at the EOC was used as the reference temperature for this RCM data, and was therefore reported for all of the data points collected in this paper. T_C was defined as the simulated temperature at the EOC. To ensure that the adiabatic assumption during the compression stroke was realized, the simulated pressure during the compression stroke for a reactive simulation and a simulation where reactions have been "turned off" (e.g., by setting the reaction rate multiplier to zero) were compared and found to be identical. In addition, the non-reactive simulated pressure trace was compared to the non-reactive experimental pressure trace and no differences were found.

Two definitions of the ignition delay in the simulations were used. The first definition matches the definition in the experiments, with the overall ignition time defined as the global maximum of the time derivative of the pressure (dP/dt) after the EOC, and the first-stage ignition delay time defined as the first maximum of dP/dt after the EOC. The time derivative of the pressure in the simulations was computed by second order Lagrange polynomials, as discussed by Chapra and Canale [88]. In some cases, however, the pressure rise during the first-stage ignition was slow, resulting in a small peak in dP/dt. Due to electrical noise in the measured pressure signal that propagated into the simulations through the computed volume trace, a first peak in dP/dt was not always observed in the simulations despite a significant deviation of the simulated reactive pressure trace from the non-reactive pressure trace prior to ignition. In such cases, the first peak of the overall simulated heat release rate (HRR) was used to define a first-stage ignition delay time, $\tau_{1,HRR}$. This definition of the first-stage ignition delay was found to align well with the definition of first-stage ignition delay by the first maximum of dP/dt. A comparison of these

definitions is shown in Figure 1b. Note that Figures 1a and 1b show different T_C conditions; this is because we could not find an overlapping condition where the experimental dP/dt, the simulated dP/dt, and the HRR all showed distinct peaks.

3.2.3 Jet-stirred reactors

Jet-stirred reactors were modeled as 0-D adiabatic, constant pressure, perfectly-mixed, isothermal reactors with no reactions at the walls. A Cantera Solution object was installed in an IdealGasReactor. Subsequently, the IdealGasReactor was connected to a Cantera Valve object with inlet flow from a Reservoir supplying the reactant mixture. The IdealGasReactor was also connected to an outlet – a Cantera MassFlowController object, whose mass flow rate was calculated from a corresponding experimental residence time, with exhaust products flowing into another Cantera Reservoir object. This network of objects (Inlet→IdealGasReactor→Outlet) was installed in an instance of ReactorNet and integrated until steady state was reached. In all cases, integrating from multiples of 10–25 in residence times was sufficient for the systems to reach steady state.

3.2.4 Premixed laminar counterflow and burner-stabilized flames

Simulations were performed using CHEMKIN-PRO [85]. All calculations in the present work were performed with the multicomponent transport formulation and inclusion of thermal diffusion. Domain-discretized grid sizes of 200 or more points were obtained for each simulation, which was deemed sufficiently resolved (as demonstrated in a benchmark exercise for simulations of up to 600 grid points). Similarly, burner-stabilized premixed laminar flame speeds were solved with imposed experimentally measured temperature profile constraints. Multicomponent transport and thermal diffusion were included. Inlet unburned gas velocities were used as a boundary condition for the flame model.

3.3 RMG simulations

The open source Reaction Mechanism Generator (RMG) [31], Python version 1.0 (found at http://reactionmechanismgenerator.github.io) was used for automated kinetic model construction. Details of RMG's algorithm and methods can be found elsewhere [89] and are described briefly here. The model is grown using the rate-based algorithm developed by Susnow et al. [90], where RMG simulates isothermal, isobaric reactor conditions with a user-given set of initial "core" species, using a set of reaction family templates to discover all possible reactions between them, forming a new set of "edge" species. At each integration step, RMG evaluates whether an edge

species is important enough to be included in the model by checking whether it has a larger flux than the user-specified tolerance. If so, the edge species is added to the set of core species constituting the model, and it is reacted with all the existing core species to generate additional edge species and reactions. The simulation is repeated from $t = 0$ until RMG deems another edge species to be important. This iterative process of adding new edge species and re-simulating the system continues until the model satisfies the user-given termination criteria and all fluxes to edge species are below the threshold tolerance. For more information on this software package, see Gao et al. [91].

4. Results and discussion

4.1 Detailed kinetic models

4.1.1 Base model

A base model (hereafter described as Model I) of 120 species and 701 reactions is assembled in the present work from three principal sources. The propane submechanism (along with the majority of the small molecule chemistry) is adopted from Merchant et al. [28], in which the low temperature kinetics are derived from the detailed *ab initio* and rate theory calculations of Goldsmith et al. [27]. Goldsmith and coworkers also computed the thermodynamic parameters for a large number of the species relevant to propane oxidation [27]; these are adopted in the present work. The base chemistry for H_2/CO/H_2O_2/HCO compounds was updated with that from the CEFRC mechanism [92][93]. The remaining base chemistry in the model assembled by Merchant et al. [28] is derived from the work of Healy et al. [94] and is carried forward into Model I. The DME kinetics and related thermochemistry are largely adopted from the recent work of Burke et al. [9], who have validated their model for a number of experimental targets over a wide range of pressure, temperature, and composition conditions. Those authors also computed pressure dependent rate parameters for the decomposition of CH_3OCH_2 and pathways relevant to the first O_2 addition. Between 650−1000 K, the $CH_3OCH_2O_2$ adduct formed from the first O_2 addition to CH_3OCH_2 is consumed primarily by the well know isomerization-elimination chain branching pathway:

$CH_3OCH_2\bullet + O_2 = CH_3OCH_2OO\bullet$ (RO_2)

$CH_3OCH_2OO\bullet$ (RO_2) = $HOOCH_2OCH_2\bullet$ (QOOH)

Commented [JS5]: For the identical reactions with different rates, how were the rate coefficients determined in the assembled mechanism?

Commented [ed6R5]: This situation did not arise the way the mechanism was assembled in this work.

$HOOCH_2OCH_2\bullet$ (QOOH) = OH + $2CH_2O$

O_2 + $HOOCH_2OCH_2\bullet$ (QOOH) = $\bullet OOCH_2OCH_2OOH$ (O_2QOOH)

$\bullet OOCH_2OCH_2OOH = HOOCH_2OCHO + \bullet OH$

$HOOCH_2OCHO = \bullet OCH_2OCHO + \bullet OH$

This first O_2 addition and its subsequent reactions have also been recently investigated by Eskola et al. [16] and Rodriguez et al. [19]. We tested the use of all three (the two aforementioned sets in addition to that by Burke et al. [9]) elementary reaction sets against a wide range of low temperature experimental targets, finding that the reaction sequence by Burke et al. [9] gave superior overall performance against the large number experimental targets used in this work. Thus, we retained the reactions corresponding to first O_2 addition from the model of Burke et al. [9]. The rate of $CH_2O + H = HCO + H_2$ was also updated based on the results of a recent combined computational and theoretical study [95]. Further updates based on rate evaluations and calculations are described below.

4.1.2 RMG model

One additional model was generated in the present work using RMG. By specifying Model I as a "seed mechanism" in RMG, all of the reactions in Model I were forced to be included in the final RMG model. This model is referred to hereafter as Model II. Reactor conditions spanning the temperature and pressure ranges of the RCM data obtained in this work were used as RMG input reactor parameters to generate Model II. This model is substantially larger in size, with 168 species and 3979 reactions, as RMG found more than 3200 reactions and 48 species that satisfied the criteria for inclusion in the model. Aspects of the two models generated in this work are summarized in Table 3.

Table 3. Species and reaction count for models used in this work.

Model	Number of species*	Number of reactions
Model I	120	701
Model II	168	3979

*RMG-generated species are listed in the Supplementary Material

Model II was used to simulate many of the experimental targets chosen for this work, including the RCM data measured in the present study and the JSR data of Rodriguez et al. [19]. For all cases considered, Model I and II predicted the available experimental data equally well, even though RMG discovered a plethora of reactions between DME and propane radical intermediates. Although it is possible that differences between Models I and II may surface for fuel-rich or pyrolytic conditions, these are not conditions of practical interest since most practical devices [ideally] operate with fuel-lean or stoichiometric combustion. We note however, that Model II did have an impact on predicted methyl formate JSR species profiles of Rodriguez et al. [19], which are sensitivity to a number of factors discussed below. Model I is used as the primary comparison tool with the experimental data in the remainder of the present work. In addition to the model-experiment comparisons presented in this paper, a large number of additional validations using Model I are available in the Supplementary Material and are identified in Table 1.

The results of this exercise support the hypothesis that binary fuel models designed for dual fuel purposes may be assembled simply based on combinations of their separate submechanisms. This notion, in combination with advanced model merging tools [96] which can identify and eliminate redundant species and/or reactions, may make model generation for future binary fuel mixtures a facile task (assuming the independent submechanisms are reliable). Although cross-reactions between larger radical intermediate derivatives of DME and propane do not influence any of the experimental targets modeled in this work, there is clearly kinetic coupling of the fuels as a result of DME's higher reactivity and OH, HO_2 radical formation which promotes autoignition of propane. As illustrated and elaborated upon in a later section, even small amounts of DME can significantly reduce the ignition delay times of DME/propane binary mixtures.

Commented [Gu7]: I wonder if this claim is more specific to this case since there are a lot of overlapping radicals between propane and dme... How boldly could we say this about other binary mixtures? - Connie

Commented [ed8R7]: Other than OH and HO2, there are not really any radicals that overlap. However, we could considered narrowing down the statement to DME + alkanes of C3 or larger size (since propane is commonly viewed as a prototypical linear fuel surrrogage)

4.2 Rate considerations, evaluations, and calculations

As discussed in the previous section, a number of updates to rates of important reactions in the DME and propane submechanisms were performed in this work. These are described in the following sections.

4.2.1 HO_2CH_2OCHO = OH + OCH_2OCHO

The decomposition of HO_2CH_2OCHO (hydroperoxymethylformate) to OH + OCH_2OCHO is known to drive autoignition of DME below 700 K [20]. The rate of this decomposition reaction remains highly uncertain, and is typically tuned to fit experimental data (published and adopted

rates can differ by over 2 orders of magnitude). In addition, all current DME models use a rate derived from the soft recommendation of Baulch et al. [97] for the decomposition of C_2H_5OOH (ethyl hydroperoxide) to C_2H_5O + OH (although most others have adjusted the rate coefficient). The decomposition rate of the ketohydroperoxide is not expected to be the same as the ethyl hydroperoxide. Here, similar approach was adopted in this work, where the activation energy of the nominal Baulch evaluated rate [97] was reduced by 2 kcal/mol to better match the DME RCM experiments of this work. Figure 2 compares the rate of this decomposition reaction with select literature values, illustrating the large disparity. As elaborated upon below, the assumed rate this reaction also strongly influences predicted peak methyl formate (MF) mole fractions in the JSR experiments of Rodriguez et al. [19].

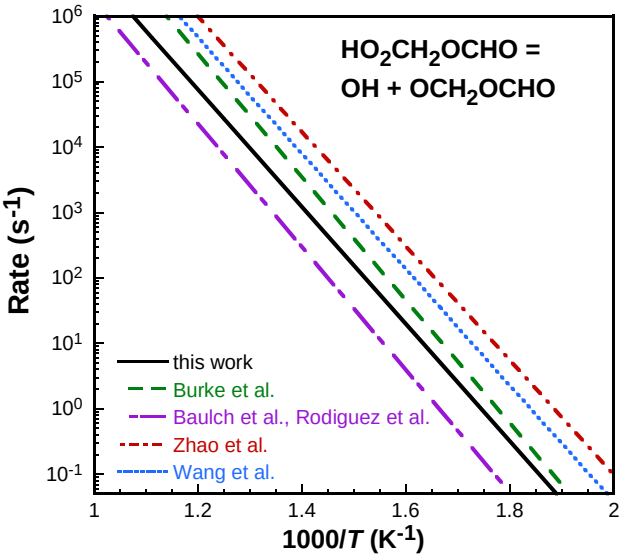

Figure 2. Comparison of the rates of the decomposition of the ketohydroperoxide hydroperoxymethylformate (HO_2CH_2OCHO) to OH + OCH_2OCHO between 500–1000 K. Black line: this work; red dash-dotted line: Zhao et al. [20]; blue dotted line: Wang et al. [42]; green dashed line: Burke et al. [9]; purple long/short-dashed line: Baulch et al. [97], for the reaction C_2H_5OOH = C_2H_5O + OH, recommended between 400–800 K (used in Rodriguez et al. [19]).

4.2.2 OCH_2OCHO = HOCHO + HCO

Prior to a recently discovered concerted pathway, the resulting OCH_2OCHO radical was thought to solely undergo an intra-H migration to $HOCH_2OCO$:

$OCH_2OCHO = HOCH_2OCO$

Under the low temperature oxidative conditions where $HOCH_2OCO$ is important in DME combustion, it can undergo further unimolecular decomposition:

$HOCH_2OCO = CH_2OH + CO_2$

$HOCH_2OCO = CO + HOCH_2O$

where the α-hydroxymethyl (CH_2OH) radical will almost exclusively react with O_2 under the conditions where the above pathway is important, although at higher temperatures it may undergo H-elimination to CH_2O + H [98]. $HOCH_2O$ may undergo a variety of decomposition reactions:

$HOCH_2O = HOCHO + H$

$HOCH_2O = OH + CH_2O$

$HOCH_2O = H + HCOOH$

which are further discussed below in a separate section. Wang et al. [42] recently discovered a concerted elimination from OCH_2OCHO:

$OCH_2OCHO = HOCHO + HCO$

This concerted reaction results in formic acid (HOCHO) and formyl (HCO), and is faster than the competing intra-H migration by an order of magnitude or more below 1400 K. In their work, Wang et al. [42] explored the potential energy surface in detail at the UQCISD(T)/CBS//B3LYP/6-311++G(d,p) level of theory, followed by pressure-dependent rate calculations using MESMER [99]. Rate coefficients were also computed in the present work, as described above, and a comparison of the decomposition with other published values is shown below in Figure 3. As illustrated in Figure 3, there is considerable pressure dependence at higher temperatures. Although the high-pressure limit rates between this work and Wang et al. [42] are in good agreement, there exists notable disagreement between the 1 atm and 10 atm rate constants. In their work, Wang et al. [42] used RRHO for all internal degrees of freedom, which could explain the slightly higher high-pressure limit rate in comparison to that computed here. Our computed pressure-dependent rate coefficients differ from those computed by Wang et al. [42] by about an order of magnitude in the combustion-relevant temperature ranges. It is also noted that in the recent work of Rodriguez et al. [19], the reaction products were assumed to be $OCH_2OCHO = CH_2O + OCHO$, negating the need to include the species $HOCH_2OCO$ in their reaction mechanism (along with its subsequent reactions). The recent mechanism of Burke et al. [9] included estimates for the intra-H migration channel, as well as a decomposition pathway to $CH_2O + OCHO$.

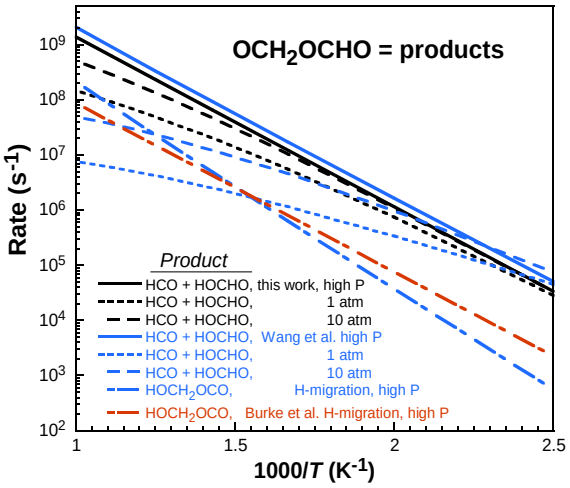

Figure 3. Arrhenius comparison of rate constants at various pressures for the unimolecular decomposition of OCH_2OCHO. Black: this work; blue: Wang et al. [42]; orange: isomerization to

HCH_2OCO (concerted elimination to HCO + HOCHO was not considered) [20] [9]. In the work of Rodriguez et al. [19], different products are assumed.

4.2.3 Self-reaction of $CH_3OCH_2O_2$

At low temperatures, the self-reaction of $CH_3OCH_2O_2$ (methoxymethyl peroxy, the 'RO_2' corresponding to DME) is in competition with RO_2 = QOOH isomerization, and subsequent OH producing reactions. Two possible product channels are considered:

$$2CH_3OCH_2O_2 = 2CH_3OCH_2O + O_2$$

$$2CH_3OCH_2O_2 = CH_3OCHO + CH_3OCH_2OH + O_2$$

Determination of product yields of this reaction has been hampered by the fact that both reactions yield MF, although Jenkin et al. [100] reported a 0.7 ± 0.1 branching ratio from FTIR product studies and photolysis experiments involving methoxymethyl peroxy. Thus, the branching fraction is dominated by the first pathway. This is further discussed below.

The rate of the RO_2 self-reaction was also indirectly measured by Rosado-Reyes et al. [101], in the temperature range of 295–600 K and pressures of 20–200 torr. In their study, the authors investigated branching ratios of the $CH_3OCH_2 + O_2$ reaction by monitoring yields of formaldehyde, methyl formate, and formic acid via transient infrared spectroscopy. The rate constant of the methoxymethyl peroxy radical self-reaction is calculated from the kinetics of the formaldehyde and methyl formate product yields [101]. At 298 K, the resulting rate of 1.9×10^{12} cm^3/mol-s is in good agreement with that measured by Jenkin et al. [100] at the same temperature (1.3×10^{12} cm^3/mol-s). The mechanism of Zhao et al. [20] used a combination of the results from Dagaut et al. [102] and Jenkin et al. [100], originally implemented by Fisher et al. [17] and Curran et al. [18]. Both Dagaut et al. [102] and Jenkin et al. [100] noted that this reaction is pressure-dependent and in the falloff regime between 228–380 K and 25–800 torr. Although Dagaut et al. [102] provided a pressure dependent parameterization of the self-reaction by monitoring its decay over 228–380 K and 25–800 torr, no kinetic model incorporates it. Furthermore, the reported experimental uncertainties of Dagaut et al. [102] are smaller than what has been reported by Rosado-Reyes et al. [101]; thus, the tabulated rates of Dagaut et al. [102] were parameterized into

the PLOG format and used in this work. Additionally, the branching fraction was assigned to 0.7 (in favor of the $2CH_3OCH_2O + O_2$ channel), as observed by Jenkin et al. [100]. A comparison of the resulting rate used in this work is shown with other values in Figure 4. Up to 600 K, the rates adopted in this work fall within the lower bound of the self-reaction rate constant reported by Rosado-Reyes et al. [101], also illustrated in Figure 4.

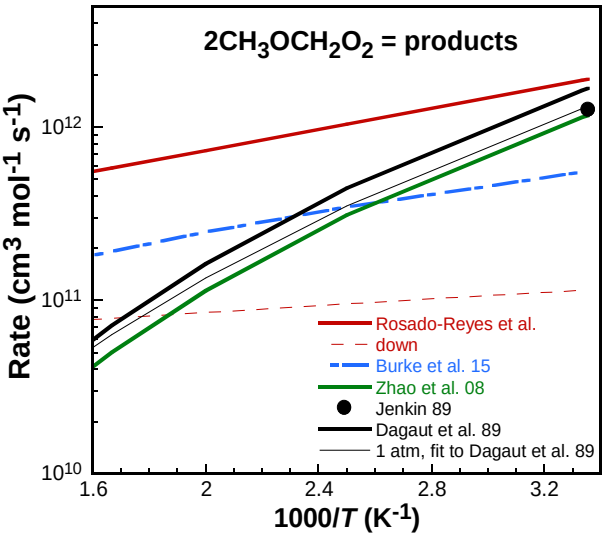

Figure 4. Arrhenius plot of the methoxymethyl peroxy self-reactions dominant channel plotted between 298–600 K. Black line: high-pressure limit rate of Dagaut et al. [102]; thin black line: fitted 1 atm rate from Dagaut et al. [102]; red: Rosado-Reyes et al. [101] (with lower limit as thin red line); green line: Zhao et al. [20], which is a combination of the results from Dagaut et al. [102] and Jenkin et al. [100], originally implemented by Fisher et al. [17] and Curran et al. [18]; black filled circle: experimental result of Jenkins et al. [100]; blue short/long dashed line: Burke et al. [9].

4.2.4 $CH_3OCH_2O = CH_3OCHO + H$

This alkoxy species is predominantly formed during the self-reaction of methoxymethyl peroxy radicals, as described above. Upon its formation, methoxymethyloxyl very quickly decomposes into methyl formate (CH_3OCHO) + H (see Figure 5 and illustration of competing $CH_3O + CH_2O$ product channel from [20]). Although rate calculations for this reaction have been performed by

Song et al. [103], no rate expressions were given. Thus, the temperature and pressure dependent kinetics were computed in the present work.

In the work of Rosado-Reyes et al. [101], the alkoxy decomposition rate is assigned a lower bound of 2×10^5 s^{-1}, as depicted in Figure 5. This value was fitted to MF and CH_2O profiles at 503 K and defined as a lower limit since the rate-limiting reaction step under the authors' experimental conditions is the self-reaction of the methoxymethyl peroxy radicals ($CH_3OCH_2O_2$). At 500 K, the rate of the corresponding high-pressure limit reaction computed in this work is over two orders of magnitude faster. Compared to the rate computed here, large discrepancies in rates exist with those used in other models. As seen in Figure 5, the rate computed here roughly splits the values determined/used in previous work. The decomposition rate is very fast: at 500 K and 1 atm, the lifetime of CH_3OCH_2O is less than 0.1 microseconds. Thus the overall self-reaction of methoxymethyl peroxy can be represented as:

$2CH_3OCH_2O_2 = 2MF + 2H + O_2$

Figure 5 also shows the minor channel ($CH_3OCH_2O = CH_3O + CH_2O$) from the model of Burke et al. [9]; the rate of reaction is not competitive with the MF channel and the reaction was therefore removed from the final model.

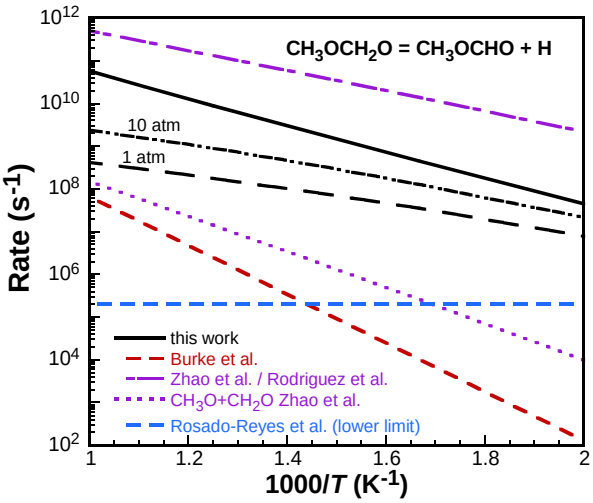

Figure 5. Comparison of rate constants at various pressures for the decomposition of CH_3OCH_2O to methyl formate (CH_3OCHO, MF) + H. Black: this work, with 1 atm and 10 atm rates also included; red: Burke et al. [9]; blue: Rosado-Reyes et al. **[101]**, lower bound; purple: Zhao et al. [20] (adopted by Rodriguez et al. [19]) with short dashed purple lines representing the decomposition channel to CH_3O + CH_2O.

4.2.5 CH_2OCHO = CH_2O + HCO

This radical species is a derivative of methyl formate, which is formed during the oxidation of DME. This reaction is only included at the high pressure limit in current combustion models [9][19][104][105]. Thus, the pressure dependence was computed here. At higher temperatures, the pressure dependence of this reaction may influence the combustion kinetics of methyl formate via H-abstraction reactions by various radicals from the parent methyl formate, forming CH_2OCHO. The decomposition rate is compared against other literature values in Figure 6. The high pressure limit used in the model by Burke et al. [9] is in fair agreement with that computed here, although that used by Rodriguez et al. [19] is faster by 1–3 orders of magnitude from 298–2000 K. Although intra-H migration is possible for this system, the unimolecular decomposition dominates for all temperatures, as illustrated in Figure 6.

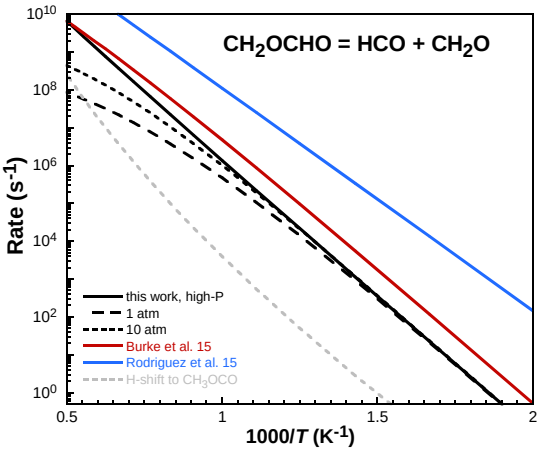

Figure 6. Comparison of rate constants at various pressures for the decomposition of CH_2OCHO. Black: this work; red: Burke et al.[9]; blue: Rodriguez et al. [19]; light grey: this work, intra-H migration to CH_3OCO.

4.2.6 $HOCH_2O$ = H + HOCHO

$HOCH_2O$ is a radical derivative of methanediol, and can be formed during its oxidation. In the context of DME, all combustion kinetic models for its oxidation created before the year 2015 (before inclusion of the concerted elimination of OCH_2OCHO to HOCHO + HCO computed by Wang et al. [42] and in this work) predict the formation of large quantities of $HOCH_2O$ during low temperature DME oxidation simulations. However, because the intra-H migration from OCH_2OCHO to $HOCH_2OCO$ is in fact a minor channel, $HOCH_2O$ forms only in small amounts during DME oxidation. Because its rate of decomposition is expected to be pressure dependent, and because this alkoxy radical may be an important intermediate during the oxidation/pyrolysis of other potential alternative fuels, its pressure-dependent decomposition rates were computed here. An Arrhenius plot comparing the results of the ME/RRKM simulations conducted in this work are shown in Figure 7 with comparisons to other available rates. We note that $HOCH_2O$ = OH + CH_2O is also included in the detailed kinetic model (written in the reverse direction, and adopted from Xu et al. [106]), but this reaction is slower under all temperatures (three orders of magnitude at 600 K, increasing to 5% of the H + HOCHO channel at 1500K).

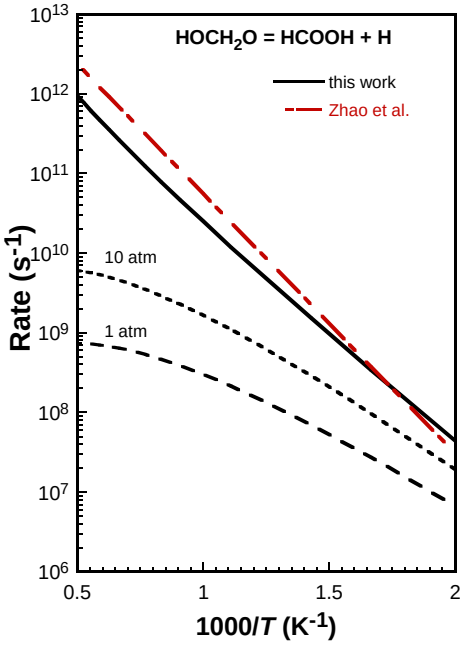

Figure 7. Arrhenius plot for the decomposition of $HOCH_2O$. Black: this work; red: used in a number of other models [20][9][42].

4.2.7 Role of cyclic peroxides

Ketohydroperoxides (KHPs) produced during low temperature hydrocarbon oxidation may undergo Korcek decomposition reactions [107–110] that can directly compete with decomposition to OH and an alkoxy radical. The Korcek decomposition reaction of a DME KHP (hydroperoxymethyl formate) is to form acetic acid + formaldehyde, and acetaldehyde + formic acid (see illustration in Figure 8). Carbonic acid has been recently detected by mass spectrometry after molecular beam sampling from a JSR by Moshammer et al. [111]. However, no rate calculations have been performed for this reaction, because the Korcek reaction for HO_2CH_2OCHO is not expected to play a significant role under the conditions of interest here (see the comparison for a propane KHP below). The primary source of OH radicals during the low temperature oxidation of propane is through the $HO_2CH_2CH_2CHO$ KHP and its unimolecular decomposition [112]:

$HO_2CH_2CH_2CHO = OH + OCH_2CH_2CHO$

which is in competition with formation of a cyclic peroxide (CP):

$HO_2CH_2CH_2CHO = CP$

The CP may further react through the following reactions:

CP = acetic acid + formaldehyde
CP = acetaldehyde + formic acid

These pathways are also schematically illustrated in Figure 8. The pathway to a CP and its subsequent products was considered in this work, but inclusion of the rates recently computed by Jalan et al. [112] did not have any influence on simulation results. The reason for this is evidenced by a comparison of the KHP decomposition rates, illustrated in Figure 9. Under the lowest temperature RCM experiments of this work (~700 K), decomposition of KHP to OH + OCH_2CH_2CHO dominates by 3 orders of magnitude. Only at and below 400 K does CP formation become competitive with the aforementioned channel. Thus, formation of CP and its subsequent reactions is not included in the kinetic mechanism in the present work.

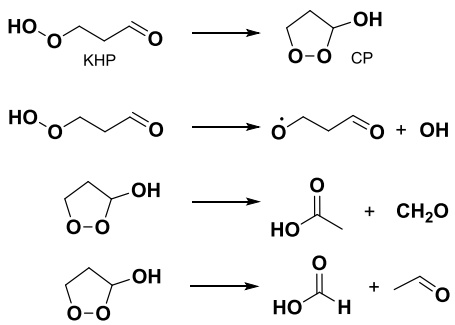

Figure 8. Ketohydroperoxide (KHP) fate and cyclic peroxide (CP) decomposition reactions investigated in previous work, with respect to propane oxidation **[112]**[27].

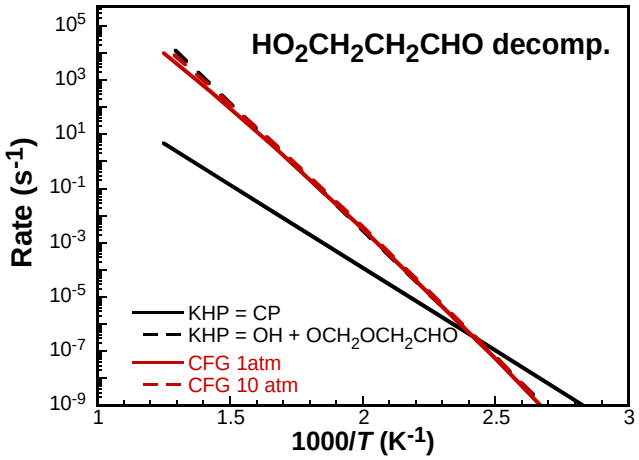

Figure 9. Rate comparison of KHP (HO_2CH_2OCHO) decomposition pathways. Black: high-pressure limit rates from Jalan et al. [112]; Red: Goldsmith et al. [27]; see Figure 8 for species definitions.

Last, it must be noted that there also exists the possibility of a formic acid catalyzed conversion of KHP to CP [112], which is relevant to the low-temperature JSR data of Rodriquez et al. [19]. Jalan et al. [112] used high-level quantum chemical methods for the analogous propane mechanism, predicting that the formic acid catalyzed reaction can lower the barrier by over 30 kcal/mol. To test the influence of this pathway on the simulated species profiles for the JSR data investigated here, rate parameters for the acid catalyzed isomerization and subsequent decomposition were estimated by analogy to those for propane (in this case, the resulting DME CP is assumed to decompose into two formic acid molecules). JSR simulations were then performed with these two additional reactions:

$HO_2CH_2OCHO + HOCHO = CP + HOCHO$

CP = 2HCOOH (formic acid)

Simulations of stoichiometric DME/O_2 mixtures in helium (corresponding to the conditions in the work of [112]) resulted in accumulation of CP up to 100 ppm (10% of the KHP peak concentration), peaking at the same temperatures as HO_2CH_2OCHO. In addition, peak formic acid and HO_2CH_2OCHO concentrations were predicted to change by ~10%. Thus, future work should include exploration of this acid-catalyzed mechanism if the low temperature (T < 600 K) JSR product distributions are to be accurately predicted.

4.2.8 C_3H_8 + OH

The competition between primary and secondary H-abstraction by OH on propane is critically important in dictating its autoignition behavior. Two reactions are possible:

$C_3H_8 + OH = n\text{-}C_3H_7 + H_2O$
$C_3H_8 + OH = i\text{-}C_3H_7 + H_2O$

As noted by Merchant et al. [28], H-abstraction from the methyl groups of propane promotes low temperature autoignition due to the resulting OH chain branching pathways, while H-abstraction at the secondary carbon site retards ignition because it leads to HO_2 formation, which further undergoes HO_2-HO_2 recombination. Therefore, we have derived rates that accurately capture both the branching ratios and total rate constants over a wide temperature range. Droege and Tully [113] previously measured absolute rate coefficients and branching fractions between 293–854 K through a laser photolysis/laser-induced fluorescence technique at 400 torr (in helium), with branching ratios determined by performing experiments using six selectively deuterated isotopes of propane. The resulting branching ratios were found to be strikingly similar to those previously determined by Walker's fits to experiments at 297 K and 753 K [114]. More recently, rates and branching ratios of this reaction have been computed by Huynh et al. [115], who compared their predictions with numerous other efforts performed over the last 30 years, finding excellent agreement with the experimental work of Droege and Tully [113]. However, the authors did not publish their computed rates in any form other than in an Arrhenius plot. Thus, the branching ratios published by Droege and Tully [113] were fitted to functional forms in this work – a power law form was used for the *i*-propyl branch, while a log form was used for the *n*-propyl branch with

fitting errors less than 5% below 1500 K. These were then used to define the rates for each channel based on the total rate fitted by Sivaramakrishnan et al. [116], which accurately captures experimental data spanning a wide temperature range. Sivaramakrishnan et al. [116] measured the total rate of C_3H_8 + OH in the temperature range of 797–1259 K. In their study, they performed a modified three-parameter Arrhenius regression of their data along with those of 13 other studies spanning the temperature range of 190–1248 K. This total rate – in combination with the branching fits from the work of Droege and Tully [113] – were used to derive new C_3H_8 + OH rate constant. Comparisons with this newly derived rate are made with other available rates in Figure 10. The new rates were adopted in this work and also fitted to a modified three-parameter Arrhenius form and are given in Table 4.

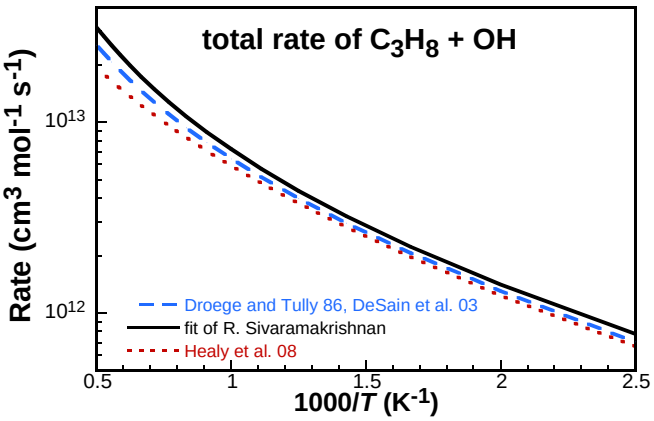

Figure 10. Comparison of the total rate of H-abstraction by OH on propane. Black solid line: fit of Sivaramakrishnan et al. **[116]**, used in this work; blue dashed line: Droege and Tully **[113]**, as well as DeSain et al. **[117][118]**; red dotted line: Healy et al. **[94]**.

Table 4. Three-parameter modified Arrhenius fits to reaction rates studied in this work, computed at the CCSD(T)-F12a/cc-pVTZ-F12//M08SO/MG3S level or re-evaluated. Units in cm^3, mole, cal, and s. Pressure dependent rate parameterizations included in the Supplementary Material.

Reaction channel	High-pressure limit rate parameters*		
	A	n	E_a (cal/mol)
$HOCH_2O \rightarrow HOCHO + H$	4.83E+08	1.350	10726
$OCH_2OCHO \rightarrow CH_2O + HCO$	3.32E+11	0.214	13818

$CH_2OCHO \rightarrow HCO + CH_2O$	8.69E+10	0.714	31689
$CH_3OCH_2O \rightarrow MF + H$	1.38E+09	1.428	12214
$C_3H_8 + OH \rightarrow n\text{-}C_3H_7 + H_2O$[1]	1.05E+10	1.080	2187
$C_3H_8 + OH \rightarrow i\text{-}C_3H_7 + H_2O$[1]	4.67E+07	1.620	-86.8
$2CH_3OCH_2O_2 \rightarrow 2CH_3OCH_2O + O_2$[1]	1.60E+23	-4.500	0
$2CH_3OCH_2O_2 \rightarrow CH_3OCH_2OH + MF + O_2$[1]	6.84E+22	-4.500	0

*Rates are of the form $k(T) = AT^n \exp(-E_a/RT)$ where R = 1.9872 cal/mol-K. Pre-exponential factor is in units of s^{-1} or $cm^3\,mol^{-1}\,s^{-1}$ depending on reaction order. MF = methyl formate.

[1]Re-evaluated in this work; see text for discussion.

4.3 Low-temperature propane oxidation

RCM ignition delay measurements were obtained for pure propane/oxidizer mixtures in order to increase model fidelity for low temperature propane autoignition and at engine-relevant conditions. Experiments were performed for three different equivalence ratios in the range T = 690–910 K. Comparisons of this data with the model of this work is shown in Figure 11. A normalized sensitivity analysis of rate parameters to [OH] at τ to the model pre-exponential factors for certain conditions is shown in Figure 12. Among the reactions are the H-abstractions from propane by the OH radical, which is especially important under fuel-lean conditions. For this reason, these reactions were critically evaluated and updated in this work, as described above. The following reactions also define the low temperature autoignition for propane:

Commented [JS9]: The sensitivity coefficient is not normalized? Should a similar sensitivity analysis be done for tau1 as well (may not be [OH])?

Commented [ed10R9]: We now define how all sensitivity coefficients have been computed in the methodology, and tau1 is described in previous work and is not reiterated here.

$n\text{-}C_3H_7O_2 = HO_2 + C_3H_6$

$OOCH_2CH_2CH_2OOH = OH + KHP$

As seen in the sensitivity spectra of Figure 12, the first reaction in the above list inhibits autoignition because it competes with the second O_2 addition and its subsequent chain branching pathways that produce additional OH radicals. The latter reaction promotes ignition through the net formation of two OH radicals (the decomposition of $OOCH_2CH_2CH_2OOH$ and additional decomposition of KHP to OH + OCH_2OCHO). As explained above, the rate parameters of these reactions were adopted from the electronic structure and resulting rate theory calculations by Goldsmith et al. [27]. Mentioned in their work are the uncertainties in computed rates solely due to the 1-D treatments of loose internal degrees of freedom, which are estimated to be less than a

factor of 2. Given the relatively large T1 diagnostic value for many of the species in that study, the global uncertainty of the computed rate is of course larger. And at the conditions where the reactions are not in the high-pressure limit, larger uncertainties are expected. The inherently large uncertainties associated with computed rate coefficients using accurate model chemistries and state of the art rate theories can result in large global kinetic uncertainties. For this reason, reducing the uncertainties of rates common to the low temperature oxidation of most fuel compounds requires more advanced global optimization and kinetic parametric uncertainty minimization techniques [11][119], which is beyond the scope of this work. Thus, rates of the two reactions above were tuned within their estimated uncertain bounds, as described below, to achieve better agreement with the RCM data obtained in this work. Figure 11 illustrates the agreement between the current RCM data and the model of this work (see the Supplemental Material, Figure S30, for model comparisons before and after the rate adjustments) for an illustration of their overall effect on simulation results. The high sensitivity of propane ignition delay to the aforementioned rates is illustrated through the large differences in predictions between the original and updated final model. The activation energy for the rate of *n*-$C_3H_7O_2$ decomposition to HO_2 + C_3H_6 was increased by 1.0 kcal/mol, while that for the decomposition of $OOCH_2CH_2CH_2OOH$ (O_2QOOH) to OH + KHP was decreased by 0.5 kcal/mol. These adjustments are within the activation energy uncertainties for these two reactions. Although the resulting overall agreement is satisfactory, these rate adjustments cannot in any way reduce the uncertainty in the respective rates due to the fact that the propane ignition delay time is sensitive to a large number of reactions which also happen to have large rate parameter uncertainties. The sensitivity spectra in Figure 12 capture this well, with many of the reactions having large sensitivity coefficients. Nonetheless, the final model performs well against the low temperature RCM data of this work and has been validated against a wide range of propane and DME/propane experimental targets, as shown below and in the Supplementary Material. Figure 11 also presents the first-stage ignition delays (τ_1) observed experimentally for propane in this work, with model predictions where applicable (not all simulations resulted in clearly defined first-stage ignition). A recent detailed numerical and analytical analysis of reactions driving first-stage propane ignition has been performed by Merchant et al. [28], and illustrates the importance of both OH and HO_2 to fuel consumption. In their study and at initial conditions of 10 atm and 650 K, they identify two sub-stages of exponential OH generation that occur before the overall ignition event. A first sub-stage exists

Commented [BW11]: I don't think we need this comparison, but if we do, I think it should go on another figure.

Commented [JS12R11]: I cannot find this figure in the SM. Intend to show the effects of each adjustment or the net effect? What is the objective here? Different from what the sensitivity results would show?

Commented [ed13R11]: I would like to get Jackie and Bill's input, and favor leaving it for now

Commented [JS14]: Should the key reactions responsible for the 1st stage reactivity be discussed as well? The effects of rate adjustments on tau1 and tau, respectively?

Commented [ed15R14]: There is another paper devoted to this topic; we now include some of those findings in the manuscript

where the concentration of HO_2 is high enough such that HO_2-HO_2 termination becomes competitive with other HO_2 reactions. This event is followed by a second sub-stage where almost all of the fuel is consumed through reaction with OH, which terminated due to depletion of the ketohydroperoxide.

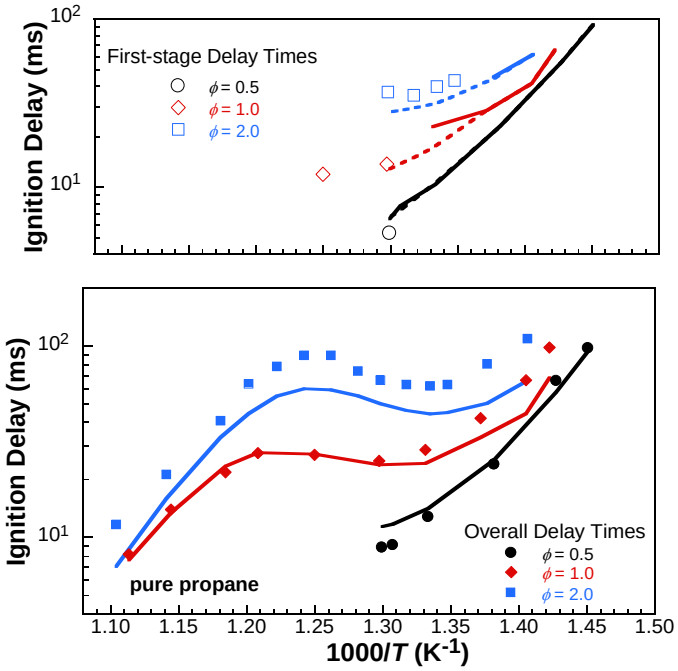

Figure 11. Experimental propane RCM data (closed symbols: $\boldsymbol{\tau}$, open symbols: $\boldsymbol{\tau_1}$) compared with the model constructed in this work for varying $\boldsymbol{\phi}$. See Table 2 for mixture compositions. Solid lines: simulated $\boldsymbol{\tau}$ or $\boldsymbol{\tau_1}$ based on $\boldsymbol{dP/dt}$. Dashed lines: simulated $\boldsymbol{\tau_1}$ based on HRR. Predictions only span the temperature range of the experimental data because experimental pressure traces are used in simulations; see text for discussion.

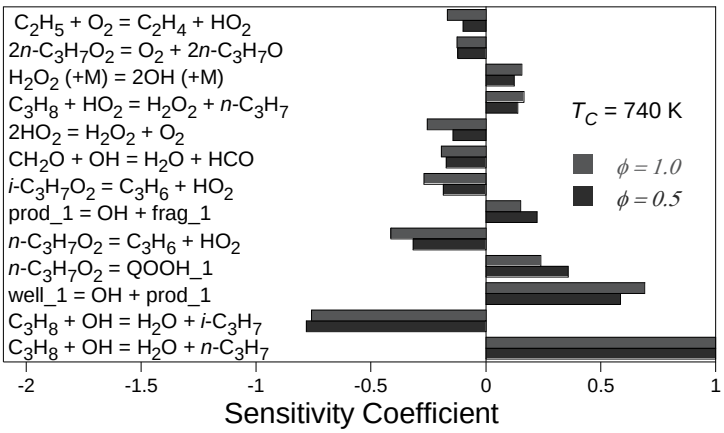

Figure 12. Normalized sensitivity spectra for [OH] to reaction rate pre-exponential factors at the ignition delay time for the model used in this work; modeled in a batch reactor under two conditions similar to those found in the present RCM experiments ($\boldsymbol{P_C}$ = 30 bar, $\boldsymbol{T_C}$ = 740 K, pure propane mixtures of $\boldsymbol{\phi = 0.5}$ and $\boldsymbol{\phi = 1.0}$). Note: prod_1, frag_1, and well_1 are 2-formyl-ethyl-hydroperoxide, 2-formyl-ethoxy, and 3-hydroperoxyl-*n*-propylperoxy, respectively, as defined in [27].

Commented [JS16]: Define the normalized coefficient by showing the equation.

Commented [ed17R16]: This is now defined in the methodology section

4.4 DME oxidation

In order to understand DME oxidation over a wide temperature range (700 to 1250 K), included here are ignition delay time comparisons with the data of Li et al. [23]. As seen in Figure 13, the agreement is excellent. The sensitivity spectra of Figure 14 show reactions that drive ignition at 23 bar and at 1000 K, for the mixture compositions in Figure 13. Among the reactions that are shown, all of those involving DME and its large low temperature intermediates are retained from the Burke et al. [9] model and adopted here. It is of interest to note that the KHP does not show up in this list, perhaps since its decomposition is so fast at 1000 K. Heat release rates were also computed for the conditions in Figure 13 for ϕ = 1 in order to better understand the reactions that drive autoignition. Between 700–1100 K, the following reactions are primarily responsible for heat release and listed in the order of their contribution:

$HCO + O_2 = CO + HO_2$

$CH_3OCH_3 + OH = CH_3OCH_2 + H_2O$

$CH_2O + OH = H_2O + HCO$

Other, smaller, contributions arise from:

$2HO_2 = H_2O_2 + O_2$

$CH_3 + HO_2 = \text{products}$

$2CH_3 = C_2H_6$

Thus, although many of the reactions of the DME submechanism which form and consume OH are important (and drive NTC behavior), so are the reactions of the H_2CO/HCO system. At temperatures above 1100 K, CH_3OCH_2 primarily undergoes unimolecular decomposition to $CH_3 + CH_2O$, which is proceeded by the small molecule core chemistry of '$C_1/H_2CO/HCO$'.

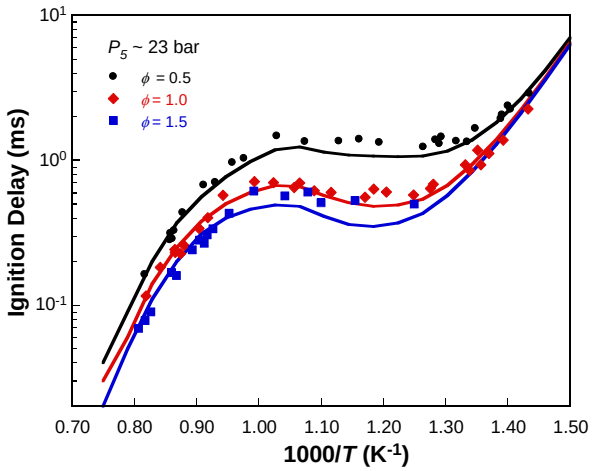

Figure 13. Variable equivalence ratio pure DME in air ignition delay time measurements of Li et al. [23] compared with simulations using the model of this work. Black: $\boldsymbol{\phi}$ = 0.5; red: $\boldsymbol{\phi}$ = 1.0; blue: $\boldsymbol{\phi}$ = 1.5; symbols: experimental data; lines: ignition delay simulation results.

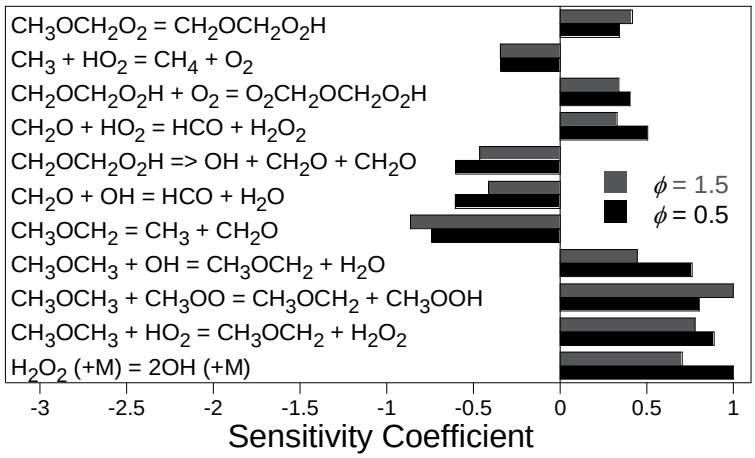

Figure 14. Normalized sensitivity spectra for [OH] to reaction rate pre-exponential factors at the ignition delay time of DME for the model used in this work and the conditions of Li et al. [23] at $\boldsymbol{T_5}$ = 1000 K and $\boldsymbol{P_5}$ = 23 bar for $\boldsymbol{\phi = 0.5}$ (black) and $\boldsymbol{\phi}$ = 1.5 (grey).

During the low-temperature oxidation of DME, there are two dominant fates of the CH_3OCH_2 ('R') radical: unimolecular decomposition to CH_3 and CH_2O, and O_2 addition to a stable $CH_3OCH_2O_2$ ('RO2'') adduct. The fraction of R that reacts to form RO_2 and eventually produce additional OH is:

$$f_{\mathrm{R+O_2\rightarrow RO_2}} \equiv \frac{\text{rate of } \mathrm{R + O_2 \rightarrow RO_2}}{\text{total rate of consumption of R}}$$

where the total rate of consumption of R is approximated as the sum of the rates of R + O_2 → QOOH and R → CH_3 + CH_2O. In addition, a quantity defined as $f_{\mathrm{QOOH+O_2\rightarrow O_2QOOH}}$ can be used to represent the fraction of QOOH that undergoes O_2 addition to form O_2QOOH with respect to the other two major pathways (β-scission to form $2CH_2O$ and an OH radical, or the chemically activated reaction with O_2 to form hydroperoxymethyl formate ($HO_2CH_2CH_2CHO$) + OH):

$$f_{\mathrm{QOOH+O_2\rightarrow O_2QOOH}} \equiv \frac{\text{rate of } \mathrm{QOOH + O_2 \rightarrow O_2QOOH}}{\text{total rate of consumption of QOOH}}$$

where the total rate of consumption of QOOH is approximated as the sum of the rates of QOOH + O_2 → O_2QOOH, QOOH + O_2 → KHP + OH (chemically activated well-skipping channel), and

QOOOH + O_2 → OH + 2CH_2O. Note that the formation of a stable O_2QOOH adduct enables 2 OH radicals to be produced, through its own decomposition and subsequent KHP decomposition (e.g., see Figure 16). The branching fractions defined above are illustrated in Figure 15 for DME in air at 1 and 23 bar (23 bar corresponding to one of the mixture compositions of Figure 13). For the 23 bar $\phi = 1$ case and at and above ~1050 K, the decomposition of R to CH_3 and CH_2O begins to dominate, representing a, exit from the NTC region of DME. However, below ~1050 K (entrance to the NTC regime), $f_{R+O_2\rightarrow RO_2} \geq 0.5$, signifying the availability for subsequent O_2 addition to promote chain branching. For the same pressure and mixture composition, $f_{QOOH+O_2\rightarrow O_2QOOH} = 0.5$ around 810 K, near the shortest ignition delay times in the NTC region. As the temperature continues to decrease, the ignition delay once again becomes Arrhenius-like and driven by the kinetics of KHP decomposition.

Commented [JS18]: At this point, the DME results have not been shown yet …….
Also, experimental results are at high P and Fig. 13 is for 1 atm.

Commented [AR19R18]: Enoch: If you have addressed the first point Jackie made and modified the text to reflect the changed figure, then you can mark this as "done."

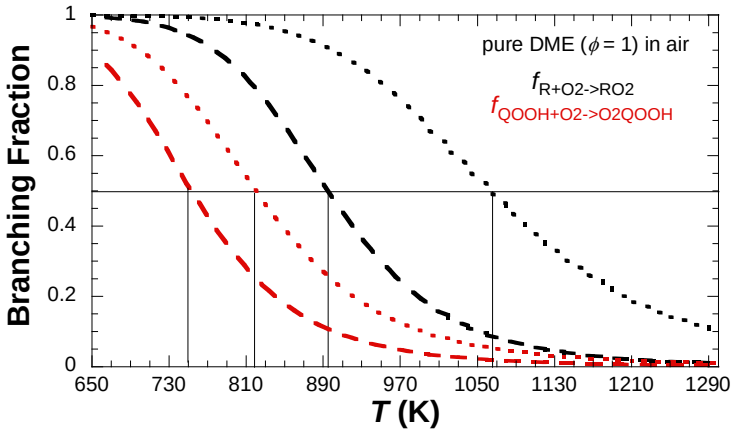

Figure 15. Branching fractions for first and second O_2 additions to stable corresponding adducts with respect to other reactions within the pure DME/air mixture with $\boldsymbol{\phi = 1}$. The dashed and dotted lines represent simulations at 1 bar and 23 bar, respectively. Red: $\boldsymbol{f_{QOOH+O_2\rightarrow O_2QOOH}}$; black: $\boldsymbol{f_{R+O_2\rightarrow RO_2}}$; horizontal line drawn at a branching fraction of 0.5; vertical lines drawn to indicate temperatures at which branching fractions equal 0.5.

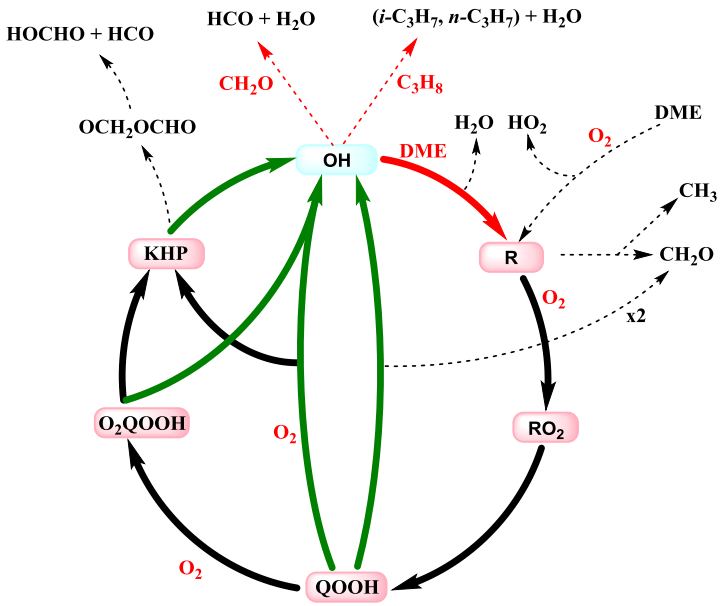

Figure 16. Schematic of major reaction pathways during the low-temperature oxidation of DME/propane blends, with focus on DME low temperature oxidation pathways. Solid green arrows: reactions that produce OH; solid red arrow: reactions that consume OH; solid black arrows: reactions that promote the chain-branching behavior; dashed red arrows: reactions that divert the reaction pathway away from the OH gain cycle of DME; dashed black arrows: included to illustrate other product species during DME oxidation. Species shown in red text represent a reactant for that corresponding reaction. See Figure 3 of [28] for a similar OH cycle of propane.

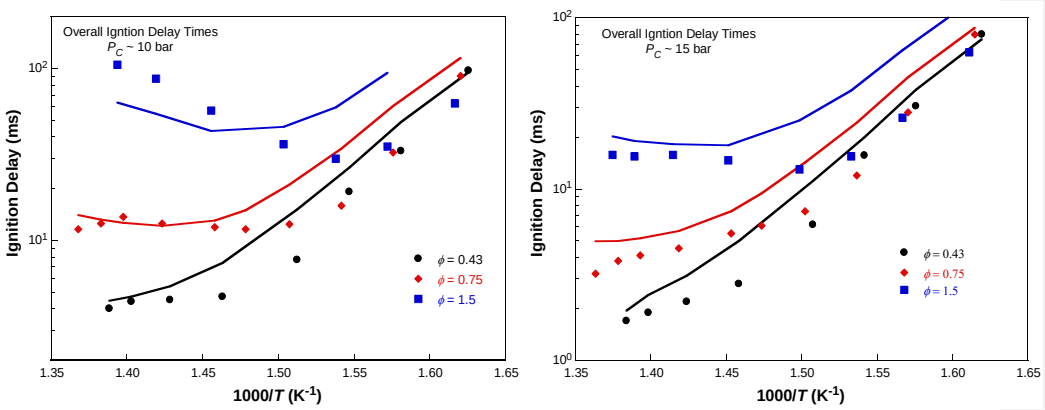

Figure 17. Measured [15] and simulated (using the RCM model of this work) overall RCM ignition delay times at 10 bar (left) and 15 bar (right) for DME/O_2/N_2 mixtures.

RCM simulations using the model of this work were also conducted for the overall and first stage DME ignition delay time measurements of Mittal et al. [15] (see Figure 17 for overall ignition delays, and the Supplementary Material for first stage comparisons). Good agreement is observed for overall ignition delay times at temperatures above 660 K. However, they are generally overpredicted at lower temperatures, by up to a factor of two. Similarly, the first stage ignition delay times are also overpredicted, with the largest model-experimental data discrepancy arising from fuel rich (ϕ = 1.5) conditions. There is also a clear predicted dependence of first- and second-stage ignition data on equivalence ratio under the lowest temperature conditions, while no corresponding dependence is observed experimentally. This is in contrast to the variable ϕ pure propane RCM measurements shown in Figure 17, which shows a clear dependence of overall ignition delay on ϕ. Although the cause for the discrepancy between the model predictions and data of Mittal et al. [15] is unclear, some dependence of ignition delay time on variable ϕ is expected since a relative reduction of available O_2 decreases the flux of CH_3OCH_2 through the low temperature chain branching pathways. In addition, we note that in the work of Mittal et al. [15], experiments were conducted with fixed [DME], while [O_2] was varied to achieve desired equivalence ratios. There is a similar factor of two over-prediction of delay time on the pure DME RCM results measured in this work and shown in Figure 20. Thus, sensitivity analyses were performed in an effort to understand what drives the predicted O_2-dependece of ignition delay at very low temperature. Sensitivity analyses (not shown) at 625 K and 15 bar for the mixture

compositions in the right panel of Figure 17 show that the reaction $CH_2OCH_2O_2H + O_2 = O_2CH_2OCH_2O_2H$ plays an increasingly dominant role in OH production at higher ϕ. For $\phi = 0.43$, autoignition is most sensitive to the KHP decomposition reaction, and the second O_2 addition has a sensitivity coefficient that is roughly one-half that for KHP decomposition. However, for $\phi = 1.5$, the sensitivity coefficient for the second O_2 addition is equal to that for the KHP decomposition, illustrating the importance of this reaction in driving DME autoignition. Thus, future work should include an improved rate coefficient for the reaction $CH_2OCH_2O_2H + O_2 = O_2CH_2OCH_2O_2H$, as well as the thermochemistry of participating species.

Rodriguez et al. [19] recently performed helium-diluted JSR experiments for three different DME equivalence ratios ($\phi = 0.25$, 1, and 2) at atmospheric pressure and in the temperature range of 500−1100 K. Along with O_2 and DME species profiles, gas chromatography was used to detect numerous additional species. Comparisons of the experimental data with simulations using the model of the present work are shown in the Supporting Material, while methyl formate species profiles comparisons are shown Figure 18. In general, the agreement between model and data is similar to that observed in the work of Rodriguez et al. [19], but peak methyl formate (MF) mole fractions are overestimated, and acetaldehyde formation is underpredicted. Rodriguez et al. [19] noted the models of Burke et al. [9] and Zhao et al. [20] also overpredict the MF mole fractions and attributed it to the 'higher reactivity' predicted by both models. Sensitivity analyses were conducted for simulated peak MF concentrations in this work. Predicted methyl formate peak concentrations are most sensitive to three factors:

1. the thermodynamic parameters, particularly the formation enthalpy, of $CH_3OCH_2O_2$ (RO_2)
2. the self-reaction rate of $CH_3OCH_2O_2$
3. the decomposition rate of hydroperoxymethylformate/HO_2CH_2OCHO to OH + O CH_2OCHO.

A decrease in the standard formation enthalpy of $CH_3OCH_2O_2$ by 3 kcal/mol decreases the predicted peak MF mole fractions (at 600 K) for $\phi = 0.25$ by a factor of 3, simply due to the increased endothermicity for the overall reaction sequence:

Commented [ed20]: We must decide on a course of action and whether we want to keep this in the main text or move it to the Supplementary Material. If we keep it in the main text, I think we will have to address the inconsistency in model and data at the lowest temperatures.

Commented [BW21R20]: I would note that the model gives a similar factor of 2 over prediction of my new pure DME data in a similar temperature window for an intermediate equivalence ratio. It seems like it's a more generic problem with the DME model, and not something specific to Mittal's data.

Commented [ed22R20]: Noted in the text now. This phi dependence is accentuated in the RCM simulations; it is not as prominent for batch reactor simulations of the same conditions, which is interesting. It's not immediately clear to me why this is? Nevertheless, the O2+QOOH and KHP decomp rates drive ignition here, and both of these rates + thermo are highly uncertain, so future work should include improvements in these areas (this is outside the scope of this work)

Note: Mittal varied [O2], held [DME] fixed; in this work and for propane, it is the opposite.

Commented [BW23R20]: **"Note: Mittal varied [O2], held [DME] fixed; in this work and for propane, it is the opposite."**

This is not correct. In the pure propane experiments, [C3H8] is fixed and [O2] is varied, see Table 2. I don't think it affects the text though.

$2CH_3OCH_2O_2 = 2CH_3OCH_2O + O_2 = 2MF + 2H + O_2$.

In particular, an increased the stability of $CH_3OCH_2O_2$ decreases the rate of the first step in the above sequence (as well as the rate of the minor branching channel to $CH_3OCH_2OH + MF + O_2$). This highlights the need for accurate thermochemical parameters for DME and its radical derivatives in predicting MF formation in JSR experiments. The rate of elementary steps in the above reaction (discussed in detail above) has been re-evaluated and computed in this work, and although the uncertainty in the reaction rate of $2CH_3OCH_2O = 2CH_3OCH_2O_2 + O_2$ is not known, it is likely to be quite high based on the large spread shown in the rate comparisons of Figure 4. We also note that the predictions of this work are in contrast to the comparisons made in the work of Rodriguez et al. [19], who predict substantially lower MF peak mole fractions. Although simulations using the model of Rodriguez et al. [19] are in good agreement with MF data for ϕ = 1 and 2, the peak mole fraction is significantly underestimated for the fuel-lean condition (ϕ = 0.25). The rate of HO_2CH_2OCHO decomposition used in their model is that reported by Baulch et al. [97], which is a factor of 5 less than that used here at 600 K. In this work, it is not possible to reconcile our model with the current DME RCM data without increasing the rate of this decomposition reaction from the value estimated by Baulch et al. [97]. However, this also results in an overprediction of peak MF mole fractions in the JSR experiments. High level electronic structure and rate theory calculations are needed to give more than just an estimate for this important reaction, something outside the scope of this work given the high multi-reference character expected in the transition state.

Peak methyl formate concentrations are also sensitive to several reactions discovered by RMG which were not included in Model I (this in fact represents the only noticeable difference between all simulations performed using both Model I and II). Figure 18 illustrates the effect of adding these reactions on the predicted methyl formate peaks. The greatest difference occurs for ϕ = 1; inclusion of the RMG generated reactions reduces the peak methyl formate by ~40%. In addition; the RMG generated reactions promote the production of methyl formate above 800 K, although only for ϕ = 1 and 2. Because the RMG generated reactions have a substantial influence

on these predictions, they are included in the final model. These 10 reactions are primarily metathesis reactions between DME and its large radical derivatives.

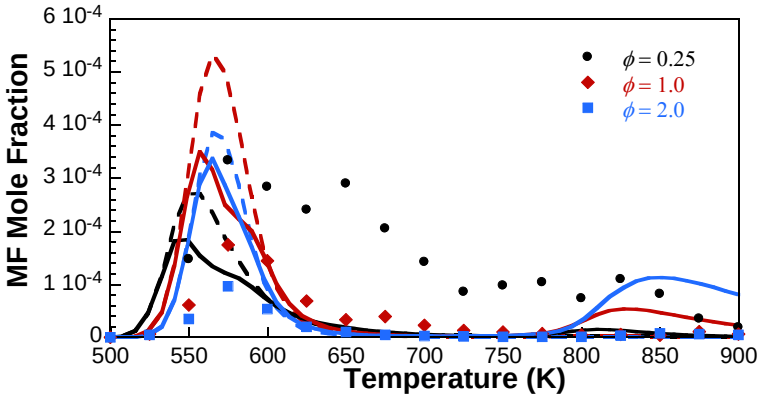

Figure 18. Comparison of measured methyl formate (MF) species profile in a jet stirred reactor [19] with the model in this work (lines). Symbols: experimental data; lines: model results. $\boldsymbol{x_{DME}}$ = 0.02, $\boldsymbol{P}$ = 106.7 kPa, residence time = 2 s, $\boldsymbol{\phi}$ = 0.25, 1, and 2). Solid lines: simulations using Model I, with 10 methyl formate reactions from Model II; dashed lines: simulations using only Model I.

4.5 DME/propane binary fuel mixtures

Although the focus of this work primarily lies in the lower temperature (T < 1000 K) regime, selected shock tube simulations were conducted at high temperatures for DME, propane, and their mixtures to verify that the final model performs well under such conditions. Figure 19 illustrates comparisons with the recent work of Hu et al. [29], which is the only DME/propane blended shock tube study to date. In addition, many other experimental targets included in Table 1 were simulated with Model I in this work; comparisons can be found in the Supplementary Material.

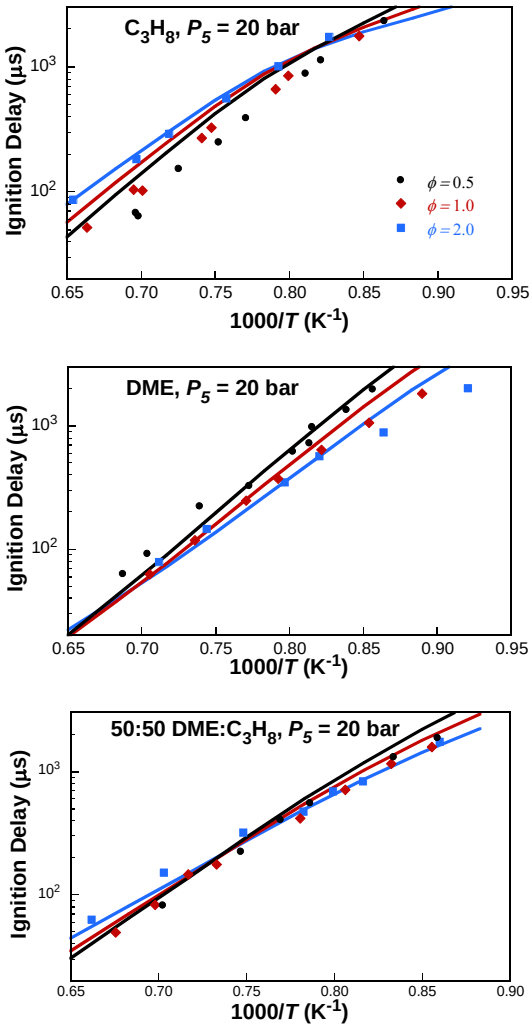

Figure 19. Comparison of engine-relevant experimental [29] DME/propane/oxygen/argon autoignition delay times with Model I for varying mixture fractions and equivalence ratios. Lines: Model I predictions; symbols: experimental data of Hu et al. [29]. Ignition delay defined as time to maximum of $\boldsymbol{d[\mathrm{OH}]/dt}$.

Figure 20 illustrates the influence of DME on the autoignition of propane in their binary mixtures in RCM experiments conducted in this work. As described above, a total of three

reactions were adjusted in the model of this work to achieve better agreement with the RCM data (see the Supplementary Material for comparisons of the model before and after rate adjustments). The resulting model performs reasonably well against the overall ignition delay times, capturing the fuel blend effects. Even a 10% addition by mole fraction of DME to propane reduces the ignition delay times by a factor of three in the NTC region, and a factor of two at both the highest and lowest temperatures studied. Also illustrated in Figure 20 are first-stage ignition delay times. The overall model-experimental data agreement is satisfactory. Sensitivity analyses were carried out with for both [DME] and [OH] at the first-stage for the 100% DME mixture at 770 K and 30 bar. As expected, the reactions of the low-temperature O_2 addition sequences and subsequent chain branching pathways, in addition to DME + O_2 = CH_3OCH_2 + HO_2 dominate OH production and DME consumption. CH_3OCH_3 + HO_2 = CH_3OCH_2 + H_2O_2 is also shown to play a role, albeit a minor one.

Commented [JS24]: Again, if tau1 is compared in this section, some discussions on the key reactions responsible for the first-stage activity are expected.

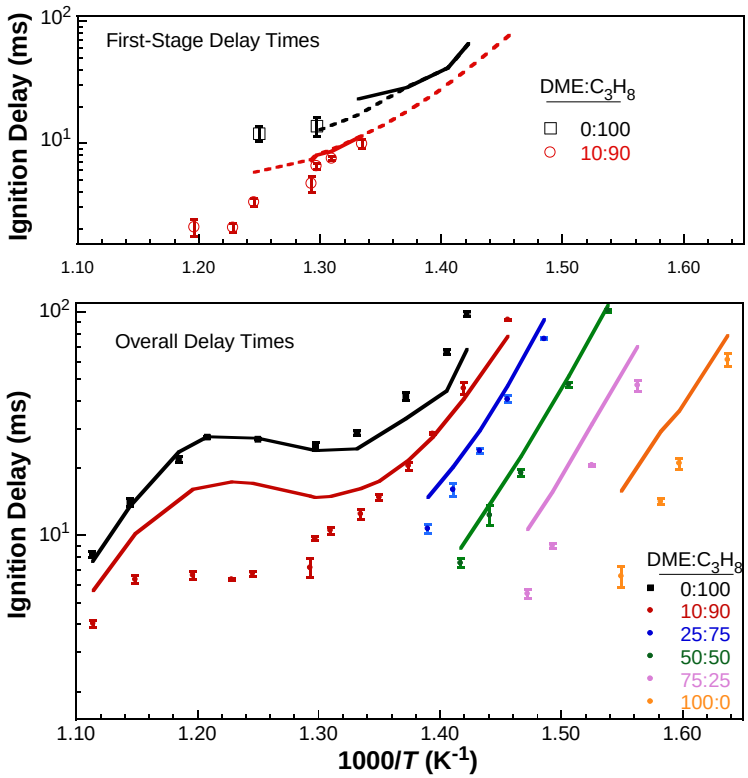

Figure 20. Comparison of RCM data with present model for varying DME/propane blend ratios by mole (P_C ~ 30 bar, $\phi = 1.0$). Blending ratio is defined within plot; solid lines: simulated overall and first stage ignition delays with final model of this work based on dP/dt; open circles: first stage ignition delay time (τ_1) measurements of this work; dashed lines: simulation of τ_1 based on the HRR. Note that not all simulations resulted in clearly defined first-stage ignition.

Figure S30 compares the DME/propane blended RCM data of this work to simulation results provided by other relevant models available in the literature. The model of Rodriguez et al. [19] significantly overestimates the ignition delay time of the pure propane and 10:90 DME:propane mixtures. DME ignition delay times predicted using the model of Burke et al. [9] are in good agreement with the current RCM data, primarily because the KHP decomposition rate is so high (see Figure 2). Recall that this is also the reason the model overpredicts MF peak mole fractions measured in the JSR experiments of Rodriguez et al. [19]. Thus, there is an apparent

Commented [ed25]: Make sure this label is correct

Commented [AR26R25]: We still need to clean up that figure. Worst case scenario we can just make it a plot using just the Rodriguez model since it's recent and what we discuss here.

trade-off between reconciling model predictions with low temperature shock tube and RCM data and accurately capturing the MF JSR species profiles.

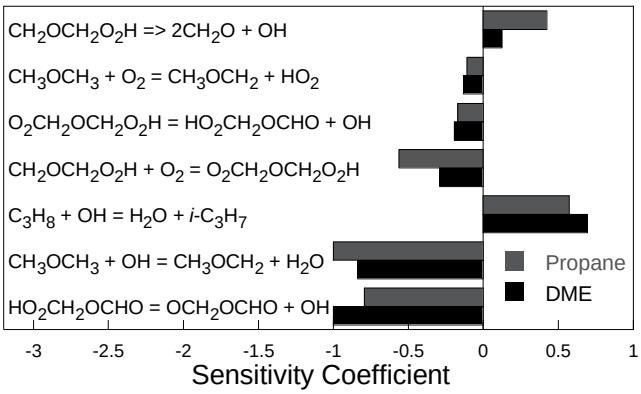

Figure 21. Normalized sensitivity spectra for [DME] and [Propane] at 50% propane consumption to reaction rate pre-exponential factors for the model used in this work, modeled in a batch reactor under conditions similar to those found in the present RCM experiments (***T*** = 690 K, ***P*** = 30 bar, 25:75 DME:propane mixture in air at $\boldsymbol{\phi}$ = 1)

As seen in the sensitivity spectrum for a binary DME/propane mixture (Figure 21), the decomposition of hydroperoxymethylformate to produce OH drives overall consumption of both DME and propane below 700 K. In addition, the sensitivity spectrum of propane is qualitatively the same as that for DME, illustrating the strong coupling of the two fuels as well as the promoting effect of DME on propane consumption. However, sensitivities of fuel concentration to H-abstraction by OH from both parent fuels are of opposing magnitude. This is due to the different overall reactivity of propane and DME under these conditions, where the low temperature chain branching cycle of DME is active, but that for propane is not. Thus, the reaction of C_3H_8 + OH to *i*-propyl is in effect a radical sink under the conditions shown in Figure 21. As discussed by Merchant et al. [28**]**, this is due to the inability of *i*-propyl to undergo OH producing chain branching reactions. Instead, it goes on to produce HO_2 + propene.

Commented [JS27]: Need to define the sensitivity coefficient used here.

Commented [ed28R27]: Defined in methodology now

Commented [JS29]: What is the % consumption of DME at this point of "50% propane consumption"?

Commented [ed30R29]: For the 25:75 mixture, about 51% of the DME has been consumed at 50% propane consumption

4.6 Propane combustion enhancement via DME

Under the fuel blend conditions studied here, propane combustion is promoted as a result of low temperature DME oxidation through the schematic of Figure 16. DME reacts with molecular

oxygen to produce the CH_3OCH_2 and HO_2 radicals, which then engages the low temperature autoignition sequence of DME through O_2 addition to CH_3OCH_2. A net gain of OH radicals results in H-abstraction from propane, generating *i*-propyl and *n*-propyl radicals, and therefore engaging the low temperature autoignition chemistry of propane. For all binary mixtures studied in this work, we observed similar rates of decay of both DME and propane, within 3% up to the ignition delay time. This is because the rate of H-abstraction by OH on DME is a factor of two higher than the total rate of H-abstractions by OH on propane for all temperatures. Additionally, the corresponding rate of H-abstraction by HO_2 on DME is higher than that for propane by 70% at 500 K, decreasing to 6% at 700 K. At higher temperatures, H-abstraction by HO_2 on propane begins to dominate H-abstraction by HO_2 on DME, by up to 25% at 1200 K. Thus, although H-abstraction by OH on DME is faster than on propane, the greater relative concentration of HO_2 (by orders of magnitude; e.g., see Figure 22) in the binary blends of this work results in both fuel compounds being consumed at similar rates.

Commented [JS31]: DME reacts first and is consumed earlier, right?

Commented [ed32R31]: Yes, but to a negligible extent. However, this is now quantified in the text

Illustrated in Figure 22 is the promoting effect of DME on propane autoignition: a 5:95 DME:propane blend ratio contains enough DME to reduce propane autoignition by 20% in this case. The binary blend composition was created by replacing 5% (by mole) of the propane in a stoichiometric propane/air mixture with DME. We also tested the relative influence of O_2 + DME = HO_2 + CH_3OCH_2 on the promoting effect of DME on propane. This reaction was removed from the model and simulations similar to those in Figure 22 were performed, with only a slight increase in the overall ignition delay time for the 5:95 DME:propane mixture. Thus, the promoting effect of DME on propane autoignition is dominated by OH and HO_2.

Figure 23 illustrates the nonlinear promoting effect of DME on propane for stoichiometric binary DME/propane mixtures under various conditions. Due to the existence of an NTC-regime for this binary fuel blend, the promoting effect under varying initial conditions is nether exponential nor 2nd order in DME concentration. Clearly though, nonlinear trends are predicted, and experimentally observed for the 710 K case. This temperature in particular was chosen because it is the only temperature where overall ignition delay times could be measured in this work for all fuel blends up to 50:50 DME:propane. The strong promoting effect of DME on overall autoignition even in low quantities (also illustrated through the 10:90 mixture of Figure 16) illustrates why this compound has been proposed as a fuel additive in automotive engines.

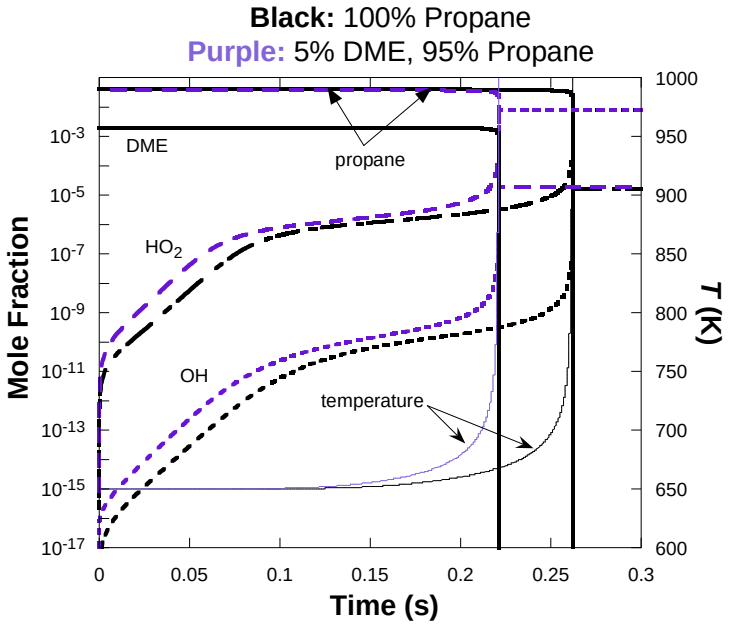

Figure 22. Temperature, OH, HO_2, and fuel species profiles for a CONV reactor simulation of a stoichiometric 100% propane/air mixture (black lines) and a 5:95 DME:propane blend in air (purple lines) at an initial temperature and pressure of 650 K and 30 atm, respectively. Simulations are conducted using the model of this work. Temperature ordinate maximum is set to 1000 K for easier viewing of corresponding temperature profiles.

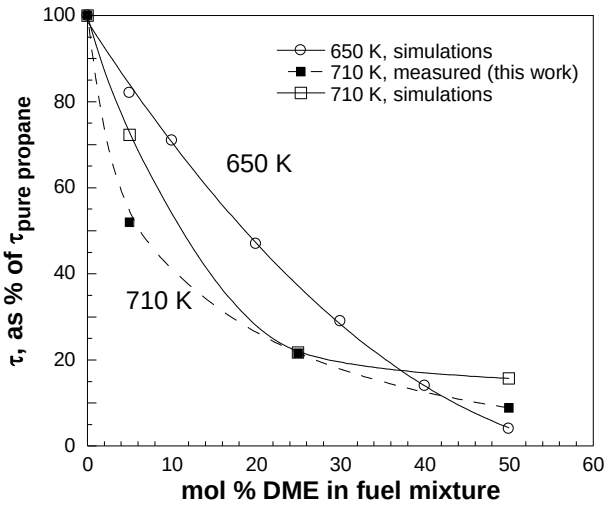

Figure 23. Influence of DME addition on binary DME/propane/air mixtures. DME substitution by mol % to an undiluted stoichiometric propane/air mixture (ϕ = 1, P = 30 atm) for two temperatures. Filled squares: τ values from the RCM measurements of this work at 710 K with corresponding RCM-simulated values (open squares); open circles: CONV simulations of τ at 650 K (fits to each data set provided to guide the eye).

Commented [JS33]: CONV- or RCM-simulated?

Overall OH gain is another way to understand the promoting effect of DME on propane. OH gain can be defined as the fraction of OH radicals created compared to those consumed in the low-temperature OH cycle of a given compound. As discussed by Merchant et al. [28], at low temperatures (500–600 K), the propane KHP chemical amplifier has an OH gain of about 1.5 (i.e., each OH produced results in another 1.5 OH's produced). As temperature increases, the OH gain drops primarily due to the increased rate of $CH_3CH_2CH_2O2 = HO_2$ + propane. Above about 700 K the propane KHP cycle no longer amplifies [OH]. A similar analysis for the DME KHP chemical amplifier gives an OH gain of 2 at low temperatures, which drops with increasing temperature, primarily due to the reaction $CH_2OCH_2OOH = 2CH_2O$ + OH. For DME/propane binary mixtures, the overall gain is expected to be an average of the pure molecule gains, weighted by the rates of H-abstraction by OH on the parent fuel compounds.

Commented [JS34]: Have you actually checked and confirmed this for 0-100% DME in fuel blend?

Commented [ed35R34]: No, but the sentence is reworded to state this is an expectation

4.7 Overall model performance

A parity plot of the experimental ignition delay time data points taken from the shock tube experiments listed in Table 1 and the RCM data experiments from this work is shown in Figure 24 for the model presented in this work, the Rodriguez et al. model [19], and the Wang et al. model [42]. Comparisons with the Burke et al. [9] model are not shown since much of the DME chemistry in this model is directly adopted into the model of this work. In general, all models perform equally well. It is interesting to note the general model-data discrepancy at very long overall ignition delay times, where achieving constant volume reactor conditions becomes a challenge (or, simply not possible), as recently discussed by Hanson et al. [86]. Additional experimental targets (species profiles behind reflected shock waves, perfectly stirred reactor data) were also considered and are included in the Supplemental Material.

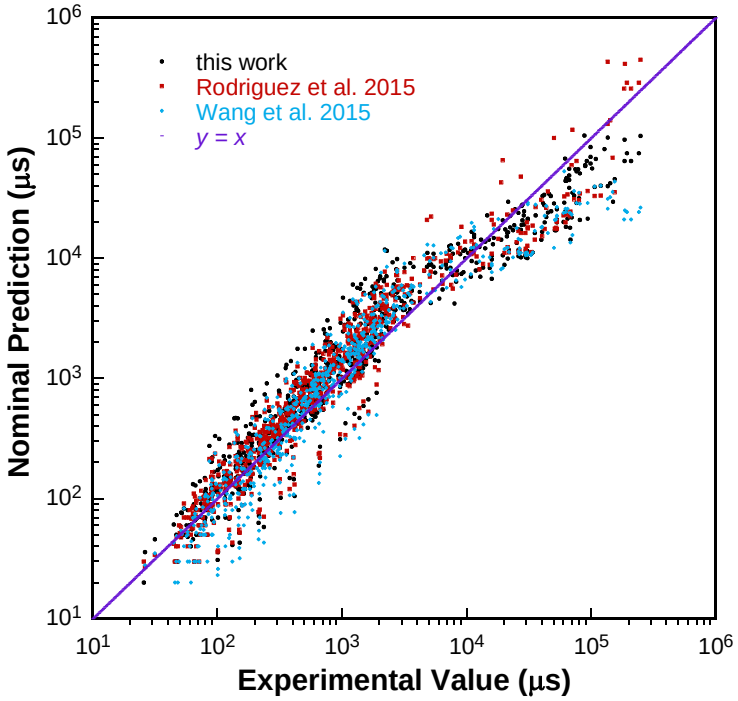

Figure 24. Parity plot of all experimental shock tube data in this paper and the Supplementary Material ([9][21][22][23][29][43][44][47]) and the RCM data from this work with the corresponding predicted ignition delay time values from the model in this work (black circles), the model from Rodriguez et al. [19]

(red squares), and the model from Wang et al. [42] (blue diamonds). Purple line: $\boldsymbol{y = x}$, for visual comparison.

5. Conclusions

A model for the oxidation of DME/propane binary fuel mixtures has been developed and validated against a wide range of experimental targets. A number of recent advances in DME and propane combustion have been compiled and included in this model. In particular, the pressure dependent unimolecular decomposition of CH_3OCH_2 [9] has been included from other work and the concerted elimination from OCH_2OCHO to HOCHO + HCO [42] along with an accurate evaluation for the reaction and branching of C_3H_8 + OH, a re-evaluation of $2CH_3OCH_2O_2$ = products, and accurate computation of pressure-dependent unimolecular decomposition rates for several radical intermediates of DME:

$CH_2OCHO = CH_2O + HCO$

$OCH_2OCHO = HOCHO + HCO$

$HOCH_2O = H + HOCHO$

$CH_3OCH_2O = CH_3OCHO + H$

In addition to being radical intermediates during low temperature DME oxidation, some of the above species are directly relevant to the combustion of methyl formate, acetone, and methylene glycol.

New RCM data have been obtained at 30 bar for T_C = 600–900 K for pure propane mixtures as well as a range of DME/propane blends. The model constructed in this work performs well against the RCM data as well as other literature experimental data. Both the RCM data and model illustrate the significant promoting effect DME has on propane autoignition.

The Reaction Mechanism Generator tool was additionally utilized in an effort to discover cross-reactions between large radical intermediates of both parent fuel compounds. Although RMG generated over 3000 additional reactions including many cross-reactions, they did not have an effect on most simulation results. The important cross-reactions that do occur for this binary

fuel blend are through the OH and HO_2 radicals, suggesting that binary fuel models designed for dual fuel purposes may be assembled simply based on combinations of their separate submechanisms. This observation, in combination with advanced model merging tools [96] which can identify and eliminate redundant species and/or reactions, may make model generation for future binary fuel mixtures a facile task (assuming the independent submechanisms are reliable).

6. Acknowledgements

We need to list funding agencies

The work at the University of Connecticut was supported by the National Science Foundation under Grant No. CBET-1402231.

References

[1] Arcoumanis C, Bae C, Crookes R, Kinoshita E. The potential of di-methyl ether (DME) as an alternative fuel for compression-ignition engines: A review. Fuel 2008;87:1014–30.

[2] Kitamura T, Ito T, Senda J, Fujimoto H. Mechanism of smokeless diesel combustion with oxygenated fuels based on the dependence of the equivalence ration and temperature on soot particle formation. Int J Engine Res 2002;3:223–48.

[3] Lu X, Han D, Huang Z. Fuel design and management for the control of advanced compression-ignition combustion modes. Prog Energy Combust Sci 2011;37:741–83.

[4] Prabhakar B, Jayaraman S, Vander Wal R, Boehman A. Experimental Studies of High Efficiency Combustion With Fumigation of Dimethyl Ether and Propane Into Diesel Engine Intake Air. J Eng Gas Turbines Power 2015;137:041505.

[5] Kokjohn S, Hanson R, Splitter D, Reitz R. Fuel reactivity controlled compression ignition (RCCI): a pathway to controlled high-efficiency clean combustion. Int J Engine Res 2011;12:209–26.

[6] Splitter D, Hanson R, Kokjohn S, Reitz RD. Reactivity controlled compression ignition (RCCI) heavy-duty engine operation at mid-and high-loads with conventional and alternative fuels. SAE Technical Paper; 2011.

[7] Morsy MH. Ignition control of methane fueled homogeneous charge compression ignition engines using additives. Fuel 2007;86:533–40.

[8] Chen Z, Qin X, Ju Y, Zhao Z, Chaos M, Dryer FL. High temperature ignition and combustion enhancement by dimethyl ether addition to methane–air mixtures. Proc Combust Inst 2007;31:1215–22.

[9] Burke U, Somers KP, O'Toole P, Zinner CM, Marquet N, Bourque G, et al. An ignition delay and kinetic modeling study of methane, dimethyl ether, and their mixtures at high pressures. Combust Flame 2015;162:315–30.

[10] Mehl M, Pitz WJ, Westbrook CK, Curran HJ. Kinetic modeling of gasoline surrogate components and mixtures under engine conditions. Proc Combust Inst 2011;33:193–200.

[11] Tomlin AS, Agbro E, Nevrlý V, Dlabka J, Vašinek M. Evaluation of Combustion Mechanisms Using Global Uncertainty and Sensitivity Analyses: A Case Study for Low-Temperature Dimethyl Ether Oxidation. Int J Chem Kinet 2014;46:662–82.

[12] Liu D, Santner J, Togbé C, Felsmann D, Koppmann J, Lackner A, et al. Flame structure and kinetic studies of carbon dioxide-diluted dimethyl ether flames at reduced and elevated pressures. Combust Flame 2013;160:2654–68.

[13] Zheng XL, Lu TF, Law CK, Westbrook CK, Curran HJ. Experimental and computational study of nonpremixed ignition of dimethyl ether in counterflow. Proc Combust Inst 2005;30:1101–9. doi:10.1016/j.proci.2004.08.241.

[14] Metcalfe WK, Burke SM, Ahmed SS, Curran HJ. A Hierarchical and Comparative Kinetic Modeling Study of C1 − C2 Hydrocarbon and Oxygenated Fuels. Int J Chem Kinet 2013;45:638–75. doi:10.1002/kin.20802.

[15] Mittal G, Chaos M, Sung C-J, Dryer FL. Dimethyl ether autoignition in a rapid compression machine: Experiments and chemical kinetic modeling. Fuel Process Technol 2008;89:1244–54.

[16] Eskola AJ, Carr SA, Shannon RJ, Wang B, Blitz MA, Pilling MJ, et al. Analysis of the Kinetics and Yields of OH Radical Production from the CH3OCH2+ O2 Reaction in the Temperature Range 195–650 K: an Experimental and Computational study. J Phys Chem A 2014;118:6773–88.

[17] Fischer S, Dryer F, Curran H. The reaction kinetics of dimethyl ether. I: High-temperature pyrolysis and oxidation in flow reactors. Int J Chem Kinet 2000;32:713–40.

[18] Curran H, Fischer S, Dryer F. The reaction kinetics of dimethyl ether. II: Low-temperature oxidation in flow reactors. Int J Chem Kinet 2000;32:741–59.

[19] Rodriguez A, Frottier O, Herbinet O, Fournet R, Bounaceur R, Fittschen C, et al. Experimental and Modeling Investigation of the Low-Temperature Oxidation of Dimethyl Ether. J Phys Chem A 2015.

[20] Zhao Z, Chaos M, Kazakov A, Dryer FL. Thermal decomposition reaction and a comprehensive kinetic model of dimethyl ether. Int J Chem Kinet 2008;40:1–18.

[21] Dagaut P, Daly C, Simmie JM, Cathonnet M. The oxidation and ignition of dimethylether from low to high temperature (500–1600 K): Experiments and kinetic modeling. vol. 27, Elsevier; 1998, p. 361–9.

[22] Pfahl U, Fieweger K, Adomeit G. Self-ignition of diesel-relevant hydrocarbon-air mixtures under engine conditions. vol. 26, Elsevier; 1996, p. 781–9.

[23] Li Z, Wang W, Huang Z, Oehlschlaeger MA. Dimethyl Ether Autoignition at Engine-Relevant Conditions. Energy Fuels 2013;27:2811–7. doi:10.1021/ef400293z.

[24] Simmie JM. Detailed chemical kinetic models for the combustion of hydrocarbon fuels. Prog Energy Combust Sci 2003;29:599–634.
[25] Westbrook CK, Dryer FL. Chemical kinetic modeling of hydrocarbon combustion. Prog Energy Combust Sci 1984;10:1–57.
[26] Gallagher S, Curran H, Metcalfe W, Healy D, Simmie J, Bourque G. A rapid compression machine study of the oxidation of propane in the negative temperature coefficient regime. Combust Flame 2008;153:316–33.
[27] Goldsmith CF, Green WH, Klippenstein SJ. Role of O2+ QOOH in Low-Temperature Ignition of Propane. 1. Temperature and Pressure Dependent Rate Coefficients. J Phys Chem A 2012;116:3325–46.
[28] Merchant SS, Goldsmith CF, Vandeputte AG, Burke MP, Klippenstein SJ, Green WH. Understanding low-temperature first-stage ignition delay: Propane. Combust Flame 2015.
[29] Hu E, Zhang Z, Pan L, Zhang J, Huang Z. Experimental and Modeling Study on Ignition Delay Times of Dimethyl Ether/Propane/Oxygen/Argon Mixtures at 20 bar. Energy Fuels 2013;27:4007–13.
[30] Yamada T, Bozzelli JW, Lay TH. Comparisons of CBS-q and G2 calculations on thermodynamic properties, transition states, and kinetics of dimethyl-ether + O2 reaction system. Int J Chem Kinet 2000;32:435–52. doi:10.1002/(SICI)1097-4601(2000)32:7<435::AID-KIN6>3.0.CO;2-4.
[31] Allen JW, Goldsmith CF, Green WH. Automatic estimation of pressure-dependent rate coefficients. Phys Chem Chem Phys 2012;14:1131–55. doi:10.1039/c1cp22765c.
[32] Dagaut P, Boettner J-C, Cathonnet M. Chemical kinetic study of dimethylether oxidation in a jet stirred reactor from 1 to 10 ATM: Experiments and kinetic modeling. vol. 26, Elsevier; 1996, p. 627–32.
[33] Le Tan NL, Djehiche M, Jain CD, Dagaut P, Dayma G. Quantification of HO 2 and other products of dimethyl ether oxidation (H 2 O 2, H 2 O, and CH 2 O) in a jet-stirred reactor at elevated temperatures by low-pressure sampling and continuous-wave cavity ring-down spectroscopy. Fuel 2015.
[34] Alzueta MU, Muro J, Bilbao R, Glarborg P. Oxidation of dimethyl ether and its interaction with nitrogen oxides. Isr J Chem 1999;39:73–86.
[35] Liu I, Cant NW, Bromly JH, Barnes FJ, Nelson PF, Haynes BS. Formate species in the low-temperature oxidation of dimethyl ether. Chemosphere 2001;42:583–9.
[36] Guo H, Sun W, Haas FM, Farouk T, Dryer FL, Ju Y. Measurements of H2O2 in low temperature dimethyl ether oxidation. Proc Combust Inst 2013;34:573–81.
[37] Herrmann F, Jochim B, Oßwald P, Cai L, Pitsch H, Kohse-Höinghaus K. Experimental and numerical low-temperature oxidation study of ethanol and dimethyl ether. Combust Flame 2014;161:384–97.
[38] Herrmann F, Oßwald P, Kohse-Höinghaus K. Mass spectrometric investigation of the low-temperature dimethyl ether oxidation in an atmospheric pressure laminar flow reactor. Proc Combust Inst 2013;34:771–8.
[39] Schönborn A, Sayad P, Konnov AA, Klingmann J. Autoignition of Dimethyl Ether and Air in an Optical Flow-Reactor. Energy Fuels 2014;28:4130–8.
[40] Wada T, Sudholt A, Pitsch H, Peters N. Analysis of first stage ignition delay times of dimethyl ether in a laminar flow reactor. Combust Theory Model 2013;17:906–36.
[41] Kurimoto N, Brumfield B, Yang X, Wada T, Diévart P, Wysocki G, et al. Quantitative measurements of HO 2/H 2 O 2 and intermediate species in low and intermediate temperature oxidation of dimethyl ether. Proc Combust Inst 2015;35:457–64.
[42] Wang Z, Zhang X, Xing L, Zhang L, Herrmann F, Moshammer K, et al. Experimental and kinetic modeling study of the low-and intermediate-temperature oxidation of dimethyl ether. Combust Flame 2015;162:1113–25.
[43] Cook RD, Davidson DF, Hanson RK. Shock tube measurements of ignition delay times and OH time-histories in dimethyl ether oxidation. Proc Combust Inst 2009;32:189–96.
[44] Tang C, Wei L, Zhang J, Man X, Huang Z. Shock Tube Measurements and Kinetic Investigation on the Ignition Delay Times of Methane/Dimethyl Ether Mixtures. Energy Fuels 2012;26:6720–8.
[45] Pyun SH, Ren W, Lam K-Y, Davidson DF, Hanson RK. Shock tube measurements of methane, ethylene and carbon monoxide time-histories in DME pyrolysis. Combust Flame 4;160:747–54. doi:10.1016/j.combustflame.2012.12.004.
[46] Pan L, Hu E, Zhang J, Zhang Z, Huang Z. Experimental and kinetic study on ignition delay times of DME/H2/O2/Ar mixtures. Spec Issue Altern Fuels 2014;161:735–47. doi:10.1016/j.combustflame.2013.10.015.
[47] Pan L, Hu E, Tian Z, Yang F, Huang Z. Experimental and Kinetic Study on Ignition Delay Times of Dimethyl Ether at High Temperatures. Energy Fuels 2015;29:3495–506.
[48] Mcilroy A, Hain TD, Michelsen HA, Cool TA. A laser and molecular beam mass spectrometer study of low-pressure dimethyl ether flames. Proc Combust Inst 2000;28:1647–53.

[49] Kaiser E, Wallington T, Hurley M, Platz J, Curran H, Pitz W, et al. Experimental and modeling study of premixed atmospheric-pressure dimethyl ether-air flames. J Phys Chem A 2000;104:8194–206.
[50] Cool TA, Wang J, Hansen N, Westmoreland PR, Dryer FL, Zhao Z, et al. Photoionization mass spectrometry and modeling studies of the chemistry of fuel-rich dimethyl ether flames. Proc Combust Inst 2007;31:285–93.
[51] Wang J, Struckmeier U, Yang B, Cool TA, Osswald P, Kohse-Höinghaus K, et al. Isomer-Specific Influences on the Composition of Reaction Intermediates in Dimethyl Ether/Propene and Ethanol/Propene Flame†. J Phys Chem A 2008;112:9255–65.
[52] Xu H, Yao C, Yuan T, Zhang K, Guo H. Measurements and modeling study of intermediates in ethanol and dimethy ether low-pressure premixed flames using synchrotron photoionization. Combust Flame 2011;158:1673–81.
[53] Wang YL, Holley AT, Ji C, Egolfopoulos FN, Tsotsis TT, Curran HJ. Propagation and extinction of premixed dimethyl-ether/air flames. Proc Combust Inst 2009;32:1035–42.
[54] Daly CA, Simmie JM, Würmel J, DjebaÏli N, Paillard C. Burning velocities of dimethyl ether and air. Combust Flame 2001;125:1329–40. doi:10.1016/S0010-2180(01)00249-8.
[55] Qin X, Ju Y. Measurements of burning velocities of dimethyl ether and air premixed flames at elevated pressures. Proc Combust Inst 2005;30:233–40.
[56] Huang Z, Wang Q, Yu J, Zhang Y, Zeng K, Miao H, et al. Measurement of laminar burning velocity of dimethyl ether–air premixed mixtures. Fuel 2007;86:2360–6.
[57] Chen Z, Wei L, Huang Z, Miao H, Wang X, Jiang D. Measurement of laminar burning velocities of dimethyl ether− air premixed mixtures with N2 and CO2 dilution. Energy Fuels 2009;23:735–9.
[58] De Vries J, Lowry WB, Serinyel Z, Curran HJ, Petersen EL. Laminar flame speed measurements of dimethyl ether in air at pressures up to 10atm. Fuel 2011;90:331–8.
[59] Mittal G, Sung C-J. A Rapid Compression Machine for Chemical Kinetics Studies at Elevated Pressures and Temperatures. Combust Sci Technol 2007;179:497–530. doi:10.1080/00102200600671898.
[60] Mittal G, Sung C-J. Aerodynamics inside a rapid compression machine. Combust Flame 2006;145:160–80.
[61] Lee D, Hochgreb S. Rapid compression machines: Heat transfer and suppression of corner vortex. Combust Flame 1998;114:531–45.
[62] Weber BW, Sung C-J, Renfro MW. On the uncertainty of temperature estimation in a rapid compression machine. Combust Flame 2015;162:2518–28.
[63] Adler TB, Knizia G, Werner H-J. A simple and efficient CCSD (T)-F12 approximation. J Chem Phys 2007;127:221106–4100.
[64] Adler TB, Werner H-J. Local explicitly correlated coupled-cluster methods: Efficient removal of the basis set incompleteness and domain errors. J Chem Phys 2009;130:241101.
[65] Adler TB, Werner H-J, Manby FR. Local explicitly correlated second-order perturbation theory for the accurate treatment of large molecules. J Chem Phys 2009;130:054106.
[66] Knizia G, Adler TB, Werner H-J. Simplified CCSD (T)-F12 methods: Theory and benchmarks. J Chem Phys 2009;130:054104.
[67] Werner H, Knowles PJ, Knizia G, Manby FR, Schütz M. Molpro: a general-purpose quantum chemistry program package. Wiley Interdiscip Rev Comput Mol Sci 2012;2:242–53.
[68] Zhao Y, Truhlar DG. Exploring the limit of accuracy of the global hybrid meta density functional for main-group thermochemistry, kinetics, and noncovalent interactions. J Chem Theory Comput 2008;4:1849–68.
[69] Lynch BJ, Zhao Y, Truhlar DG. Effectiveness of diffuse basis functions for calculating relative energies by density functional theory. J Phys Chem A 2003;107:1384–8.
[70] Shao Y, Molnar LF, Jung Y, Kussmann J, Ochsenfeld C, Brown ST, et al. Advances in methods and algorithms in a modern quantum chemistry program package. Phys Chem Chem Phys 2006;8:3172–91. doi:10.1039/b517914a.
[71] Alecu IM, Zheng J, Zhao Y, Truhlar DG. Computational thermochemistry: scale factor databases and scale factors for vibrational frequencies obtained from electronic model chemistries. J Chem Theory Comput 2010;6:2872–87.
[72] Frisch MJ, Trucks GW, Schlegel HB, Scuseria GE, Robb MA, Cheeseman JR, et al. Gaussian 03, Revision B.03 2004. doi:citeulike-article-id:3013967.
[73] Boese AD, Martin JML. Development of density functionals for thermochemical kinetics. J Chem Phys 2004;121:3405–16.
[74] East ALL, Radom L. Ab initio statistical thermodynamical models for the computation of third-law entropies. J Chem Phys 1997;106:6655–74.
[75] Cantherm/RMGPy n.d. http://greengroup.github.io/RMG-Py.

[76] Allen JW, Ashcraft RW, Beran GJ, Goldsmith CF, Harper MR, Jalan A, et al. RMG (Reaction Mechanism Generator) version 3.2 2010. http://rmg.sourceforge.net/.
[77] Eckart C. The penetration of a potential barrier by electrons. Phys Rev 1930;35:1303–9.
[78] Gou X, Miller JA, Sun W, Ju Y. Implementation of PLOG function in Chemkin II and III n.d.
[79] Chang A, Bozzelli J, Dean A. Kinetic analysis of complex chemical activation and unimolecular dissociation reactions using QRRK theory and the modified strong collision approximation. Z Für Phys Chem Int J Res Phys Chem Chem Phys 2000;214:1533.
[80] Senosiain JP, Miller JA. The Reaction of n-and i-C4H5 Radicals with Acetylene. J Phys Chem A 2007;111:3740–7.
[81] Poling BE, Prausnitz JM, O'connell JP. The properties of gases and liquids. vol. 5. McGraw-Hill New York; 2001.
[82] Welty JR, Wicks CE, Rorrer G, Wilson RE. Fundamentals of momentum, heat, and mass transfer. John Wiley & Sons; 2009.
[83] Harper MR, Van Geem KM, Pyl SP, Marin GB, Green WH. Comprehensive reaction mechanism for n-butanol pyrolysis and combustion. Combust Flame 2011;158:16–41. doi:10.1016/j.combustflame.2010.06.002.
[84] Goodwin DG. An open-source, extensible software suite for CVD process simulation. Chem Vap Depos XVI EUROCVD 2003;14:2003–8.
[85] CHEMKIN-PRO. San Diego: Reaction Design; 2013.
[86] Hanson R, Chakraborty S, Pang G, Ren W, Wang S, Davidson D. Constrained Reaction Volume: A New Approach to Studying Reactive Systems in Shock Tubes. vol. 1, Springer; 2015, p. 149.
[87] Hindmarsh AC, Brown PN, Grant KE, Lee SL, Serban R, Shumaker DE, et al. SUNDIALS: Suite of nonlinear and differential/algebraic equation solvers. ACM Trans Math Softw TOMS 2005;31:363–96.
[88] Chapra SC, Canale RP. Numerical methods for engineers. vol. 2. McGraw-Hill; 2012.
[89] Green Jr. WH. Predictive Kinetics: A New Approach for the 21st Century. In: Marin GB, editor. Adv. Chem. Eng., vol. 32, Academic Press; 2007, p. 1–313.
[90] Susnow RG, Dean AM, Green WH, Peczak P, Broadbelt LJ. Rate-Based Construction of Kinetic Models for Complex Systems. J Phys Chem A 1997;101:3731–40. doi:10.1021/jp9637690.
[91] Gao, C. W. A, J. W., West RH, Green Jr, William H. Reaction Mechanism Generator: automatic construction of chemical kinetic mechanisms. Comput Phys Commun 2015.
[92] Smith G, Wang H, Dames EE, Sheen D. Foundational Combustion Chemistry 2013.
[93] Tao Y, Dames, Enoch E, Smith G, Wang H. Optimization and Uncertainty Minimization of the Foundational Fuel Chemistry Model, Cincinnati, Ohio: 2015.
[94] Healy D, Curran H, Dooley S, Simmie J, Kalitan D, Petersen E, et al. Methane/propane mixture oxidation at high pressures and at high, intermediate and low temperatures. Combust Flame 2008;155:451–61.
[95] Wang S, Dames EE, Davidson DF, Hanson RK. Reaction Rate Constant of CH2O+ H= HCO+ H2 Revisited: A Combined Study of Direct Shock Tube Measurement and Transition State Theory Calculation. J Phys Chem A 2014;118:10201–9.
[96] Lambert VR, West RH. Identification, Correction, and Comparison of Detailed Kinetic Models. 9th US Natl Combust Meet 2015.
[97] Baulch DL, Cobos CJ, Cox RA, Frank P, Hayman G, Just T, et al. EVALUATED KINETIC DATA FOR COMBUSTION MODELING SUPPLEMENT-I. J Phys Chem Ref Data 1994;23:847–1033.
[98] Dames EE, Golden DM. Master Equation Modeling of the Unimolecular Decompositions of Hydroxymethyl (CH2OH) and Methoxy (CH3O) Radicals to Formaldehyde (CH2O)+ H. J Phys Chem A 2013;117:7686–96.
[99] Glowacki DR, Liang C-H, Morley C, Pilling MJ, Robertson SH. MESMER: An Open-Source Master Equation Solver for Multi-Energy Well Reactions. J Phys Chem A 2012;116:9545–60. doi:10.1021/jp3051033.
[100] Jenkin ME, Hayman GD, Wallington TJ, Hurley MD, Ball JC, Nielsen OJ, et al. Kinetic and mechanistic study of the self-reaction of methoxymethylperoxy radicals at room temperature. J Phys Chem 1993;97:11712–23.
[101] Rosado-Reyes CM, Francisco JS, Szente JJ, Maricq MM, Frøsig Østergaard L. Dimethyl ether oxidation at elevated temperatures (295-600 K). J Phys Chem A 2005;109:10940–53.
[102] Dagaut P, Wallington TJ, Kurylo MJ. Gas phase studies of substituted methylperoxy radicals: the UV absorption spectrum and self-reaction kinetics of CH 3 OCH 2 O 2—the reaction of CF 2 ClO 2 with Cl atoms. J Photochem Photobiol Chem 1989;48:187–98.

[103] Song X, Hou H, Wang B. Mechanistic and kinetic study of the O+ CH 3 OCH 2 reaction and the unimolecular decomposition of CH 3 OCH 2 O. Phys Chem Chem Phys 2005;7:3980–8.
[104] Dooley S, Burke MP, Chaos M, Stein Y, Dryer FL, Zhukov VP, et al. Methyl formate oxidation: Speciation data, laminar burning velocities, ignition delay times, and a validated chemical kinetic model. Int J Chem Kinet 2010;42:527–49.
[105] Westbrook CK, Pitz WJ, Westmoreland PR, Dryer FL, Chaos M, Oßwald P, et al. A detailed chemical kinetic reaction mechanism for oxidation of four small alkyl esters in laminar premixed flames. Proc Combust Inst 2009;32:221–8.
[106] Xu S, Zhu R, Lin M. Ab initio study of the OH+ CH2O reaction: The effect of the OH·· OCH2 complex on the H-abstraction kinetics. Int J Chem Kinet 2006;38:322–6.
[107] Jensen R, Korcek S, Mahoney L, Zinbo M. Liquid-phase autoxidation of organic compounds at elevated temperatures. 1. The stirred flow reactor technique and analysis of primary products from n-hexadecane autoxidation at 120-180. degree. C. J Am Chem Soc 1979;101:7574–84.
[108] Jensen R, Korcek S, Mahoney L, Zinbo M. Liquid-phase autoxidation of organic compounds at elevated temperatures. 2. Kinetics and mechanisms of the formation of cleavage products in n-hexadecane autoxidation. J Am Chem Soc 1981;103:1742–9.
[109] Jensen R, Zinbo M, Korcek S. HPLC Determination of hydroperoxidic products formed in the autoxidation of n-hexadecane at elevated temperatures. J Chromatogr Sci 1983;21:394–7.
[110] Jensen R, Korcek S, Zinbo M, Johnson M. Initiation in hydrocarbon autoxidation at elevated temperatures. Int J Chem Kinet 1990;22:1095–107.
[111] Moshammer K, Jasper AW, Popolan-Vaida DM, Lucassen A, Diévart P, Selim H, et al. Detection and Identification of the Keto-Hydroperoxide (HOOCH2OCHO) and Other Intermediates during Low-Temperature Oxidation of Dimethyl Ether. J Phys Chem A 2015.
[112] Jalan A, Alecu IM, Meana-Pañeda R, Aguilera-Iparraguirre J, Yang KR, Merchant SS, et al. New pathways for formation of acids and carbonyl products in low-temperature oxidation: The Korcek decomposition of γ-ketohydroperoxides. J Am Chem Soc 2013;135:11100–14.
[113] Droege AT, Tully FP. Hydrogen-atom abstraction from alkanes by hydroxyl. 3. Propane. J Phys Chem 1986;90:1949–54.
[114] Walker R. Temperature coefficients for reactions of OH radicals with alkanes between 300 and 1000 K. Int J Chem Kinet 1985;17:573–82.
[115] Huynh LK, Ratkiewicz A, Truong TN. Kinetics of the Hydrogen Abstraction OH+ Alkane→ H2O+ Alkyl Reaction Class: An Application of the Reaction Class Transition State Theory. J Phys Chem A 2006;110:473–84.
[116] Sivaramakrishnan R, Srinivasan N, Su M-C, Michael J. High temperature rate constants for OH+ alkanes. Proc Combust Inst 2009;32:107–14.
[117] DeSain JD, Klippenstein SJ, Miller JA, Taatjes CA. Measurements, Theory, and Modeling of OH Formation in Ethyl+ O2 and Propyl+ O2 Reactions. J Phys Chem A 2004;108:7127–8.
[118] DeSain JD, Klippenstein SJ, Miller JA, Taatjes CA. Measurements, theory, and modeling of OH formation in ethyl+ O2 and propyl+ O2 reactions. J Phys Chem A 2003;107:4415–27.
[119] Sheen DA, Wang H. The method of uncertainty quantification and minimization using polynomial chaos expansions. Combust Flame 2011;158:2358–74. doi:10.1016/j.combustflame.2011.05.010.

Validated Kinetic Model for the Oxidation of Dimethyl Ether/Propane Blends: Rapid Compression Machine Experiments and Pressure-Dependent Rate Calculations

Enoch E. Dames[1], Andrew S. Rosen[1], Bryan W. Weber[2], Connie W. Gao[1], Chih-Jen Sung[2], William H. Green[1]

[1]*Department of Chemical Engineering, Massachusetts Institute of Technology, Cambridge, MA 02142*
[2]*Department of Mechanical Engineering, University of Connecticut, Storrs, CT 06269*

Supplemental Material – Additional Model Validations with Experimental Targets

Contents

I. Experimental Validations

A. Shock Tube

1. Pfahl et al. 1996

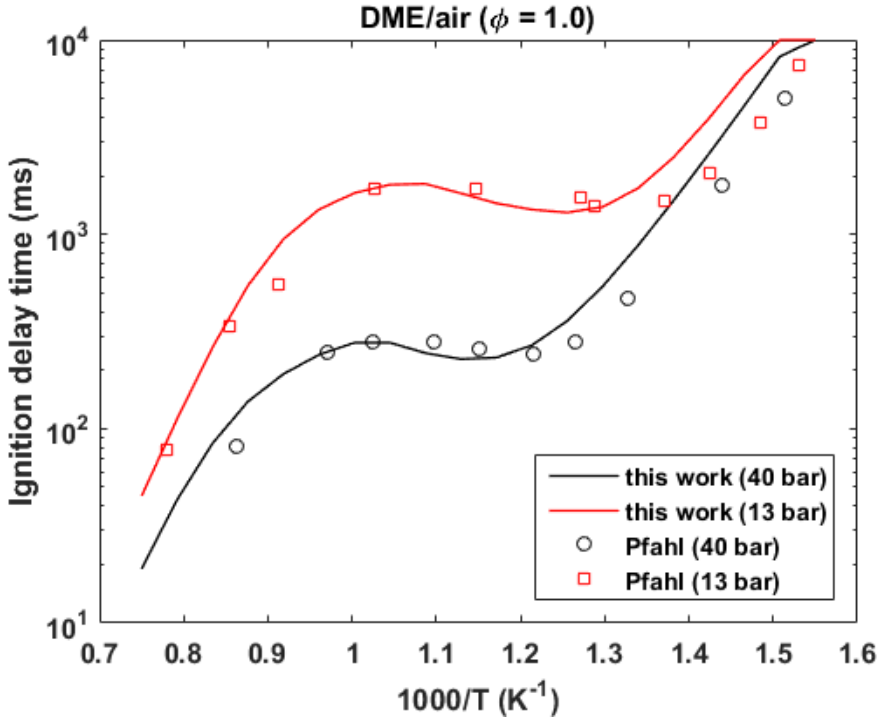

Figure S1. Ignition delay time data for the Pfahl et al. 1996 *[1]* shock tube conditions of DME/air with ϕ = 1.0 at 13 bar (red) and 40 bar (black). The experimental data is plotted as open symbols, and the simulated data using the model from this work is shown as solid lines.

2. Dagaut et al. 1998

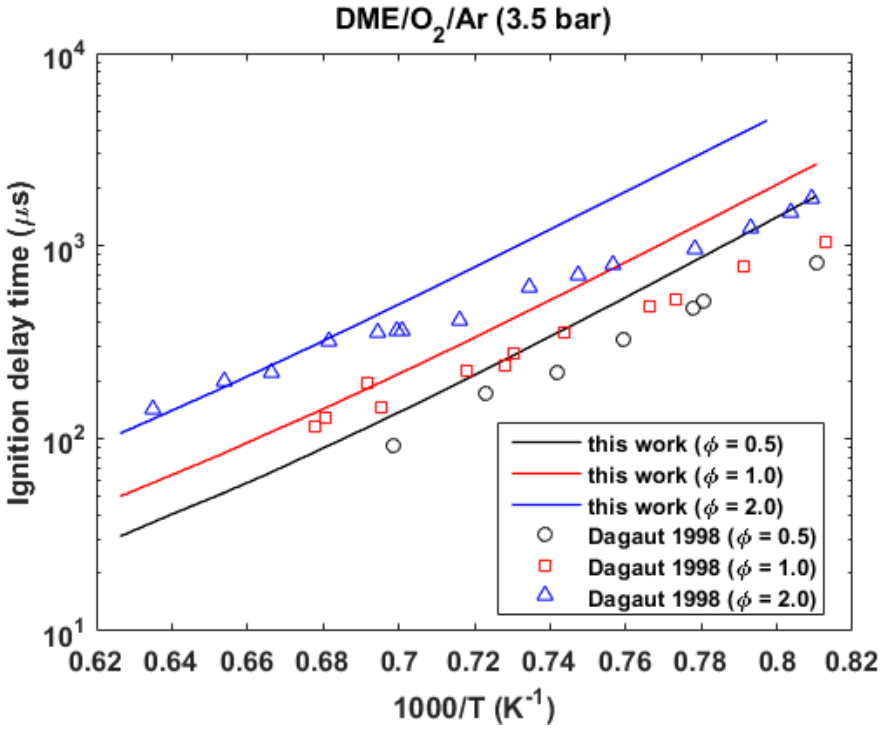

Figure S2. Ignition delay time data for the Dagaut et al. 1998 *[2]* shock tube conditions of DME/O_2/Ar at P = 3.5 bar with ϕ = 0.5 (black), ϕ = 1.0 (red), and ϕ = 2.0 (blue). The experimental data is plotted as open symbols, and the simulated data using the model from this work is shown as solid lines.

3. Cook et al. 2009

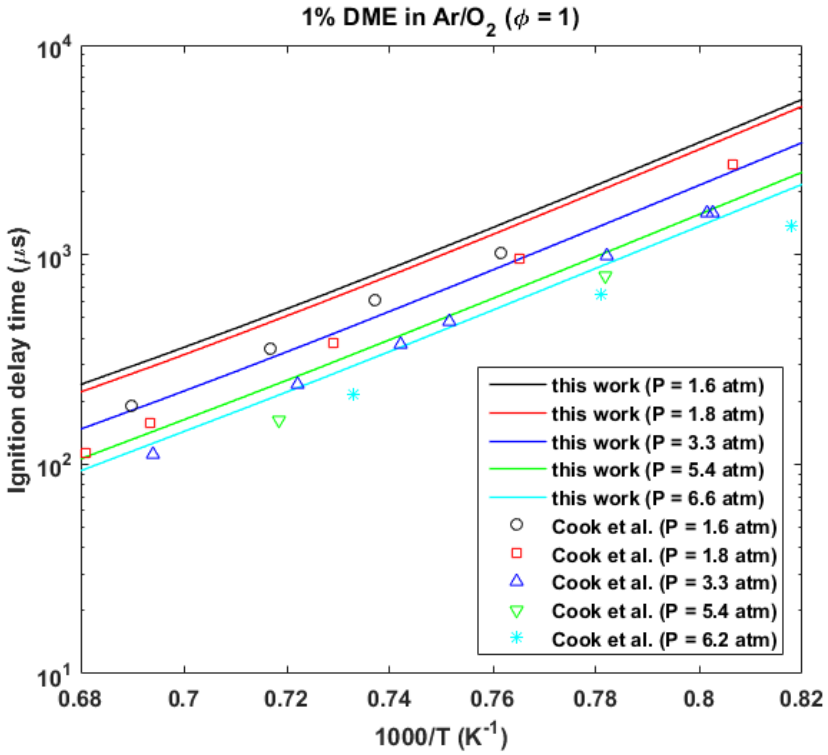

Figure S3. Ignition delay time data for the Cook et al. 2009 *[3]* shock tube conditions of 1% DME in Ar/O_2 with ϕ = 1.0 at P = 1.6 atm (black), 1.8 atm (red), 3.3 atm (dark blue), 5.4 atm (green), and 6.6 atm (cyan). The experimental data is plotted as open symbols, and the simulated data using the model from this work is shown as solid lines.

4. Tang et al. 2012

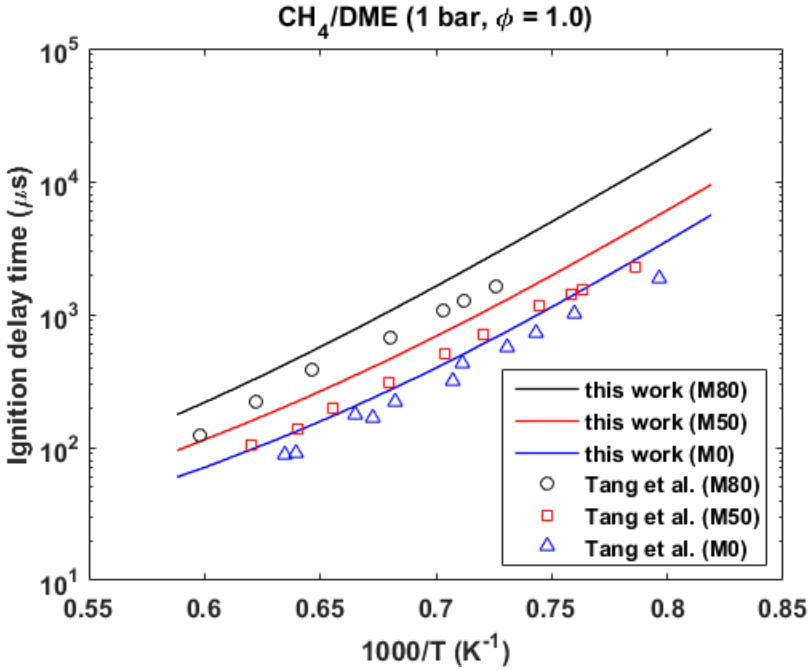

Figure S4. Ignition delay time data for the Tang et al. 2012 *[4]* shock tube conditions of CH_4/DME at P = 1 bar and ϕ = 1.0 for different DME blending ratios of 80% DME (M80, black), 50% DME (M50, red), 0% DME (M0, blue). The experimental data is plotted as open symbols, and the simulated data using the model from this work is shown as solid lines.

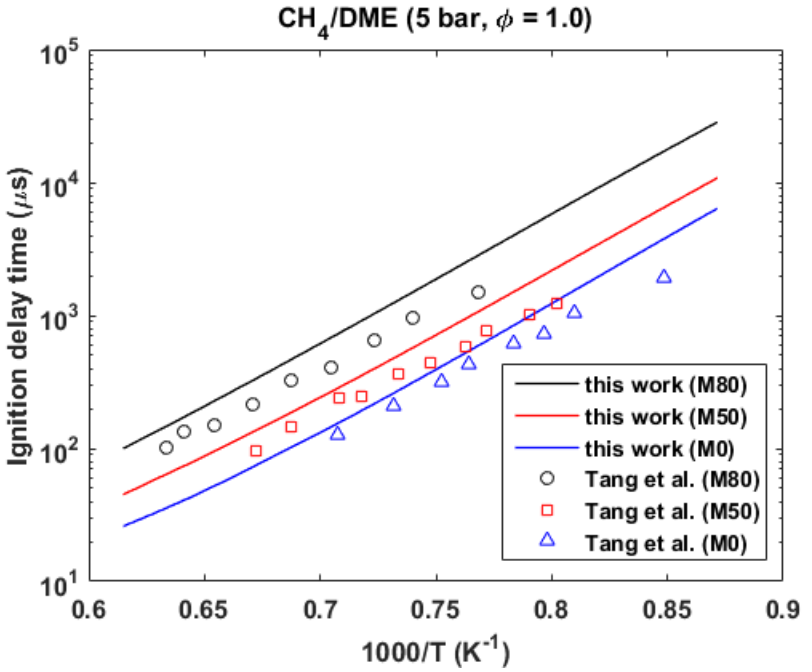

Figure S5. Ignition delay time data for the Tang et al. 2012 *[4]* shock tube conditions of CH_4/DME at P = 5 bar and ϕ = 1.0 for different DME blending ratios of 80% DME (M80, black), 50% DME (M50, red), 0% DME (M0, blue). The experimental data is plotted as open symbols, and the simulated data using the model from this work is shown as solid lines.

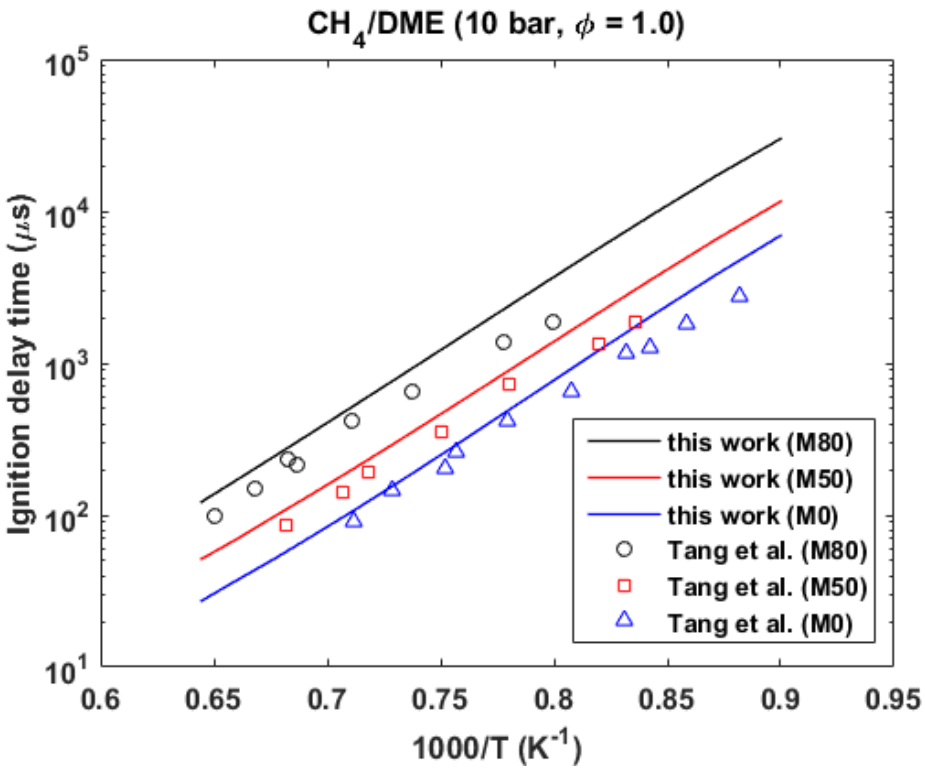

Figure S6. Ignition delay time data for the Tang et al. 2012 *[4]* shock tube conditions of CH_4/DME at P = 10 bar and ϕ = 1.0 for different DME blending ratios of 80% DME (M80, black), 50% DME (M50, red), 0% DME (M0, blue). The experimental data is plotted as open symbols, and the simulated data using the model from this work is shown as solid lines.

5. Pyun et al. 2013

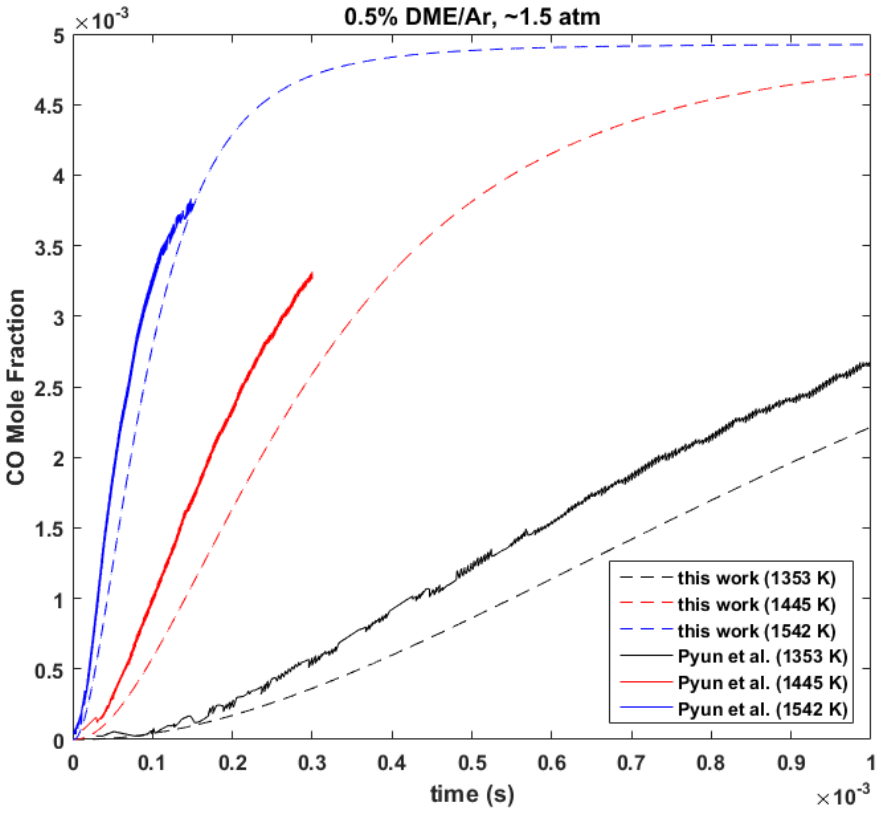

Figure S7. Carbon monoxide (CO) species profile data for the Pyun et al. 2013 *[5]* shock tube conditions of 0.5% DME in argon at P = 1.467 atm and initial temperatures of 1353 K (black), 1445 K (red), 1542 K (blue). The experimental data is plotted as solid lines, and the simulated data using the model from this work is shown as dashed lines.

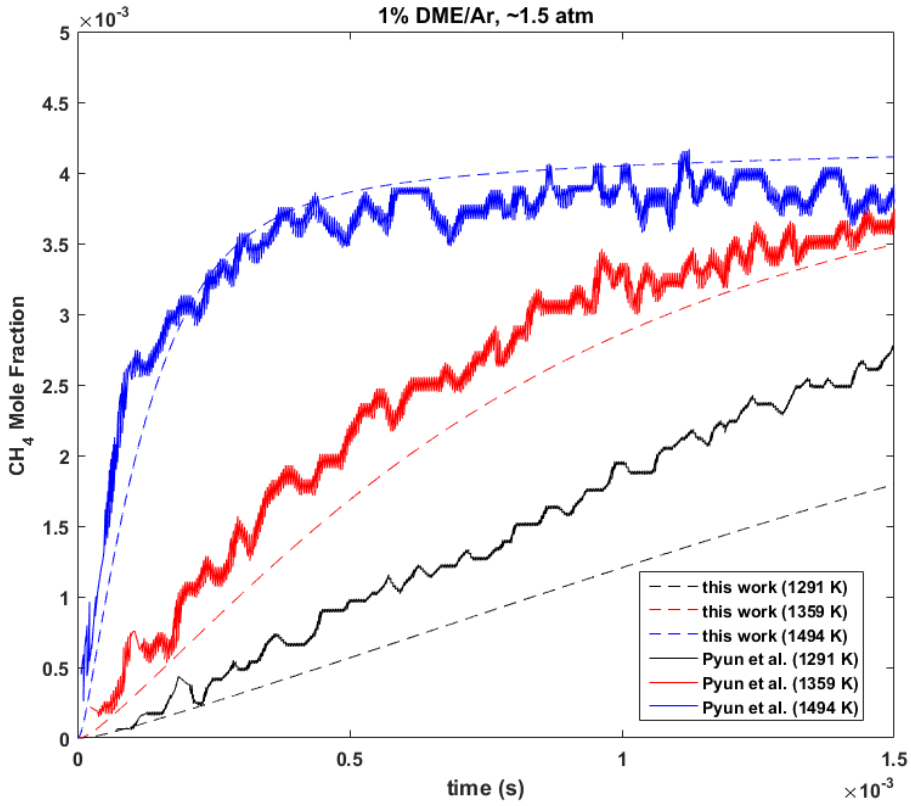

Figure S8. Methane (CH_4) species profile data for the Pyun et al. 2013 *[5]* shock tube conditions of 1% DME in argon at P = 1.467 atm and initial temperatures of 1291 K (black), 1359 K (red), 1494 K (blue). The experimental data is plotted as solid lines, and the simulated data using the model from this work is shown as dashed lines.

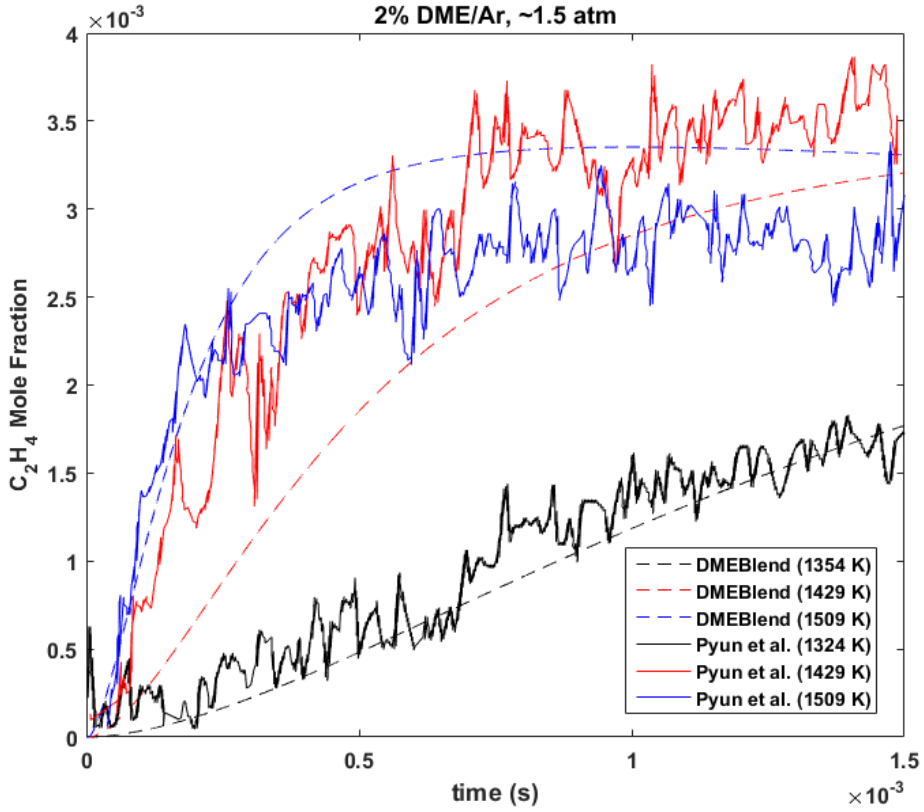

Figure S9. Ethylene (C_2H_4) species profile data for the Pyun et al. 2013 *[5]* shock tube conditions of 2% DME in argon at P = 1.467 atm and initial temperatures of 1354 K (black), 1429 K (red), 1509 K (blue). The experimental data is plotted as solid lines, and the simulated data using the model from this work is shown as dashed lines.

6. Pan et al. 2014

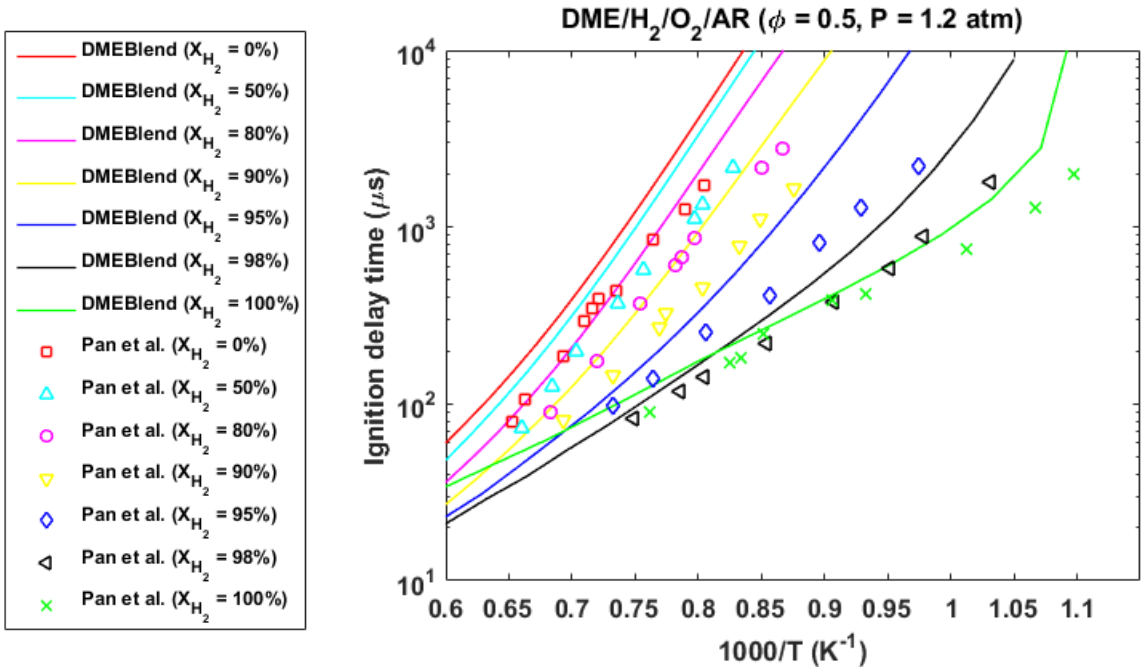

Figure S10. Ignition delay time data for the Pan et al. 2014 *[6]* shock tube conditions of DME/H_2/O_2/Ar at P = 1.2 atm at an equivalence ratio of ϕ = 0.5 for different percentages of H_2 including 0% H_2 (red), 50% H_2 (cyan), 80% H_2 (pink), 90% H_2 (yellow), 95% H_2 (blue), 98% H_2 (black), and 100% H_2 (green). The experimental data is plotted as open symbols, and the simulated data using the model from this work is shown as solid lines.

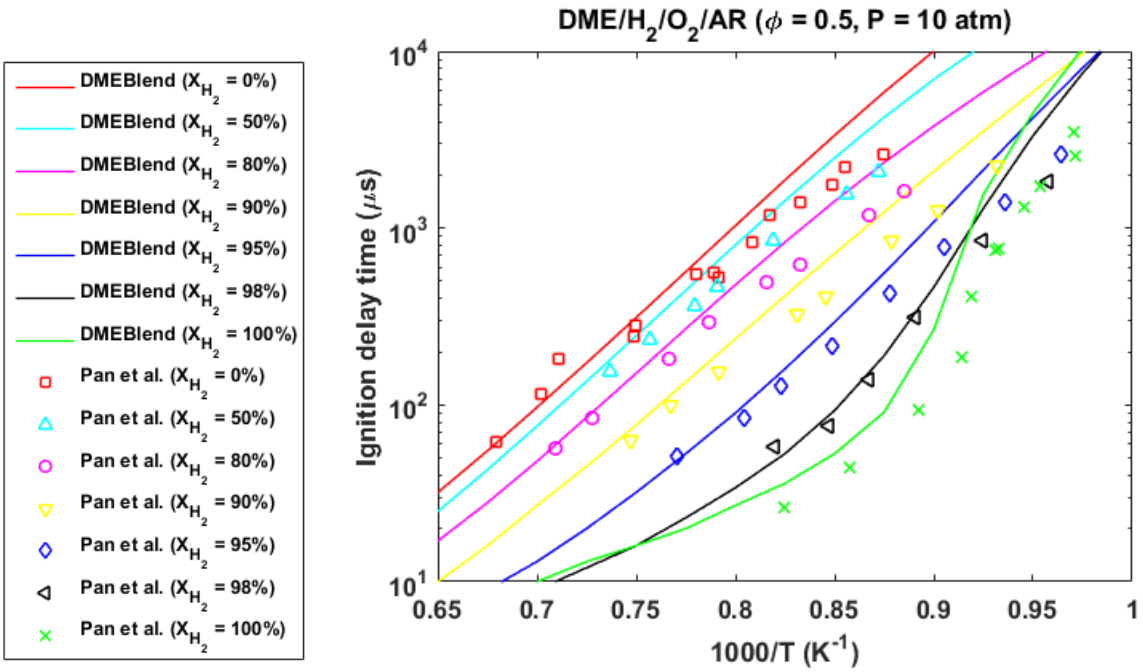

Figure S11. Ignition delay time data for the Pan et al. 2014 *[6]* shock tube conditions of DME/H_2/O_2/Ar at P = 10 atm at an equivalence ratio of ϕ = 0.5 for different percentages of H_2 including 0% H_2 (red), 50%

H_2 (cyan), 80% H_2 (pink), 90% H_2 (yellow), 95% H_2 (blue), 98% H_2 (black), and 100% H_2 (green). The experimental data is plotted as open symbols, and the simulated data using the model from this work is shown as solid lines.

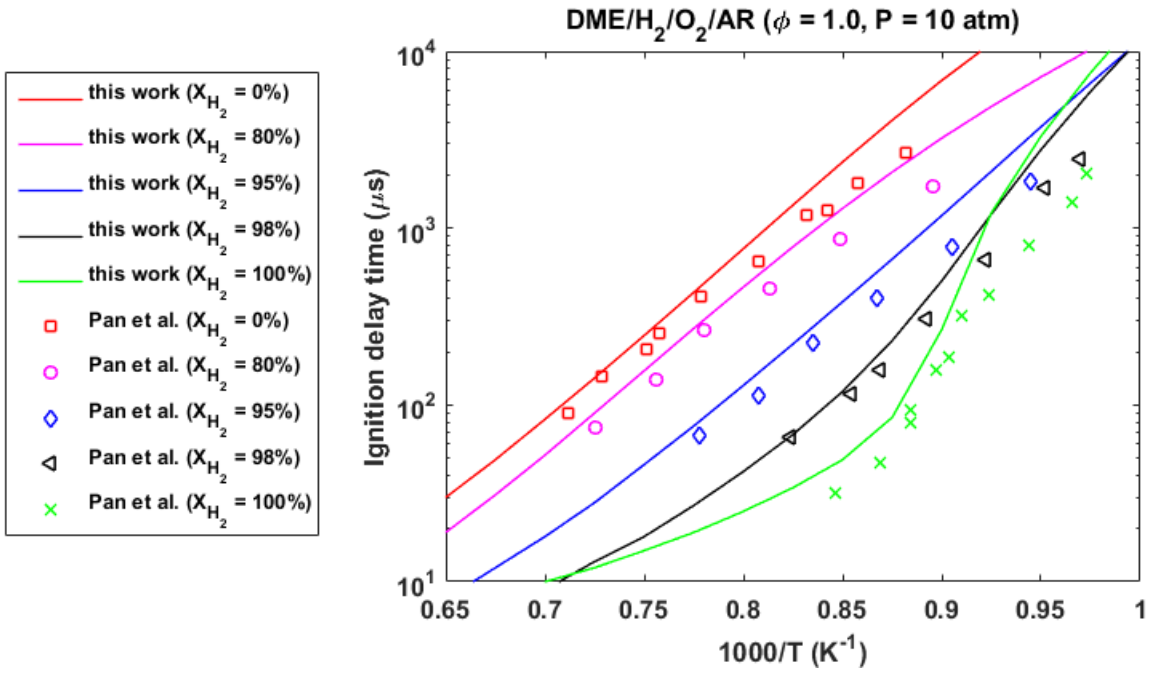

Figure S12. Ignition delay time data for the Pan et al. 2014 *[6]* shock tube conditions of DME/H_2/O_2/Ar at P = 10 atm at an equivalence ratio of ϕ = 1.0 for different percentages of H_2 including 0% H_2 (red), 50% H_2 (cyan), 80% H_2 (pink), 90% H_2 (yellow), 95% H_2 (blue), 98% H_2 (black), and 100% H_2 (green). The experimental data is plotted as open symbols, and the simulated data using the model from this work is shown as solid lines.

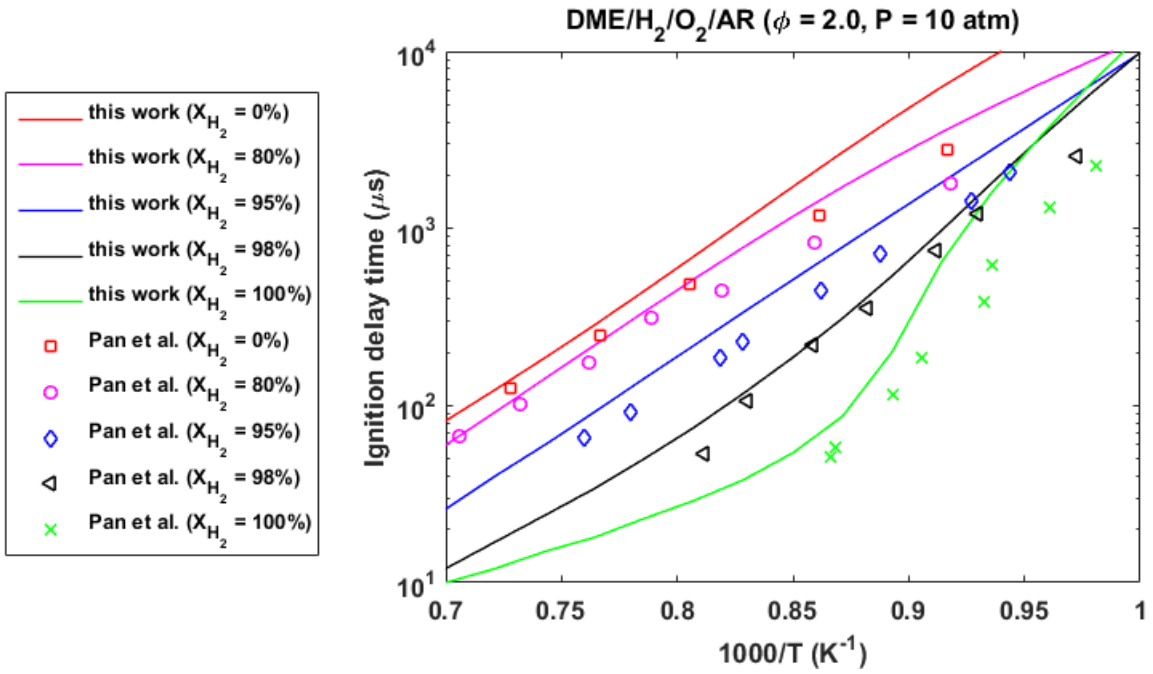

Figure S13. Ignition delay time data for the Pan et al. 2014 *[6]* shock tube conditions of DME/H_2/O_2/Ar at P = 10 atm at an equivalence ratio of ϕ = 2.0 for different percentages of H_2 including 0% H_2 (red), 50% H_2 (cyan), 80% H_2 (pink), 90% H_2 (yellow), 95% H_2 (blue), 98% H_2 (black), and 100% H_2 (green). The experimental data is plotted as open symbols, and the simulated data using the model from this work is shown as solid lines.

7. Burke et al. 2015

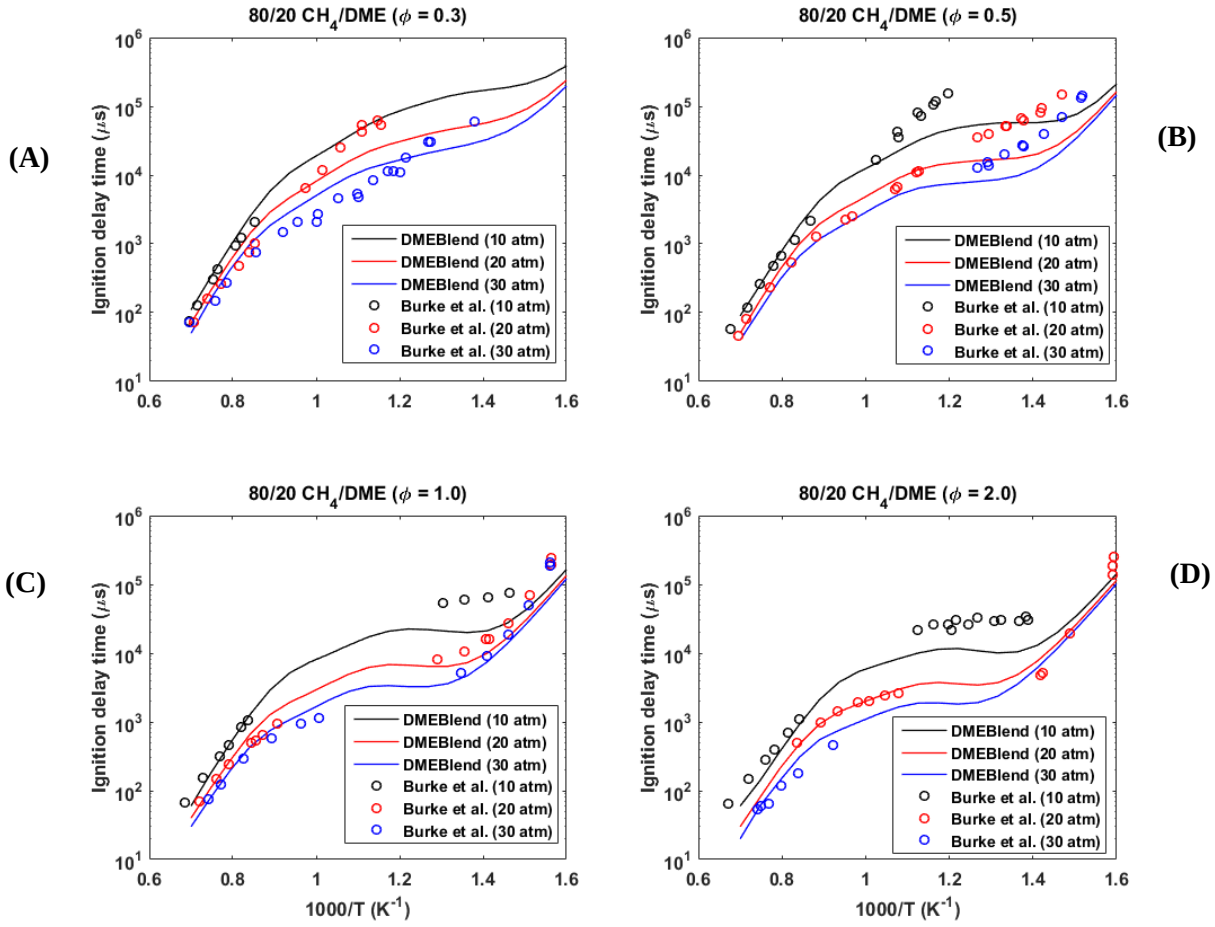

Figure S14. Ignition delay time data for the Burke et al. 2015 *[7]* shock tube conditions of 80/20 mixtures of CH_4/DME at varying pressures of 10 atm (black), 20 atm (red), and 30 atm (blue) as well as varying equivalence ratios of (A): $\phi = 0.3$, (B): $\phi = 0.5$, (C): $\phi = 1.0$, and (D): $\phi = 2.0$. The experimental data is plotted as open symbols, and the simulated data using the model from this work is shown as solid lines.

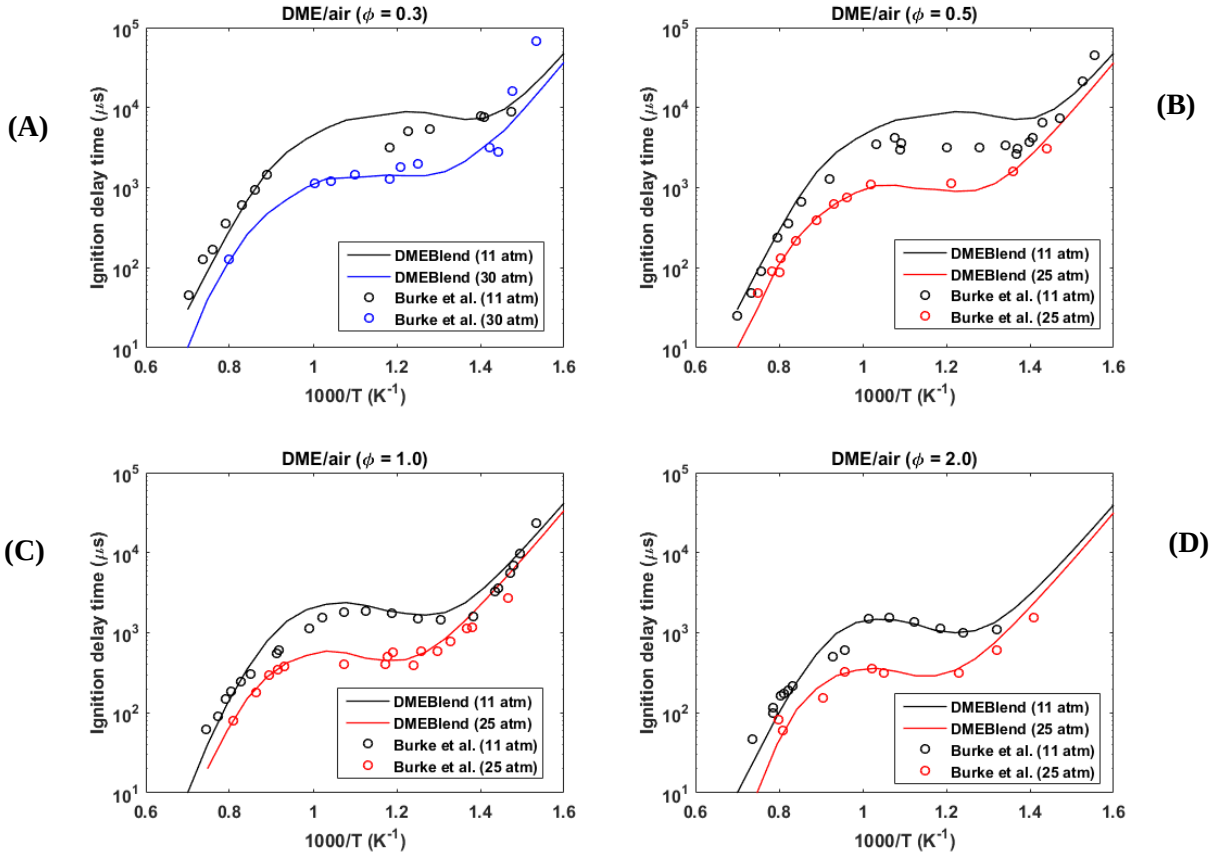

Figure S15. Ignition delay time data for the Burke et al. 2015 *[7]* shock tube and rapid compression machine experiments of DME mixtures (see Table 3 of *[7]*) at varying pressures of 11 atm (black), 25 atm (red), and 30 atm (blue) as well as varying equivalence ratios of (A): $\phi = 0.3$, (B): $\phi = 0.5$, (C): $\phi = 1.0$, and (D): $\phi = 2.0$. The experimental data is plotted as open symbols, and the simulated data using the model from this work is shown as solid lines.

8. Gallagher et al. 2008

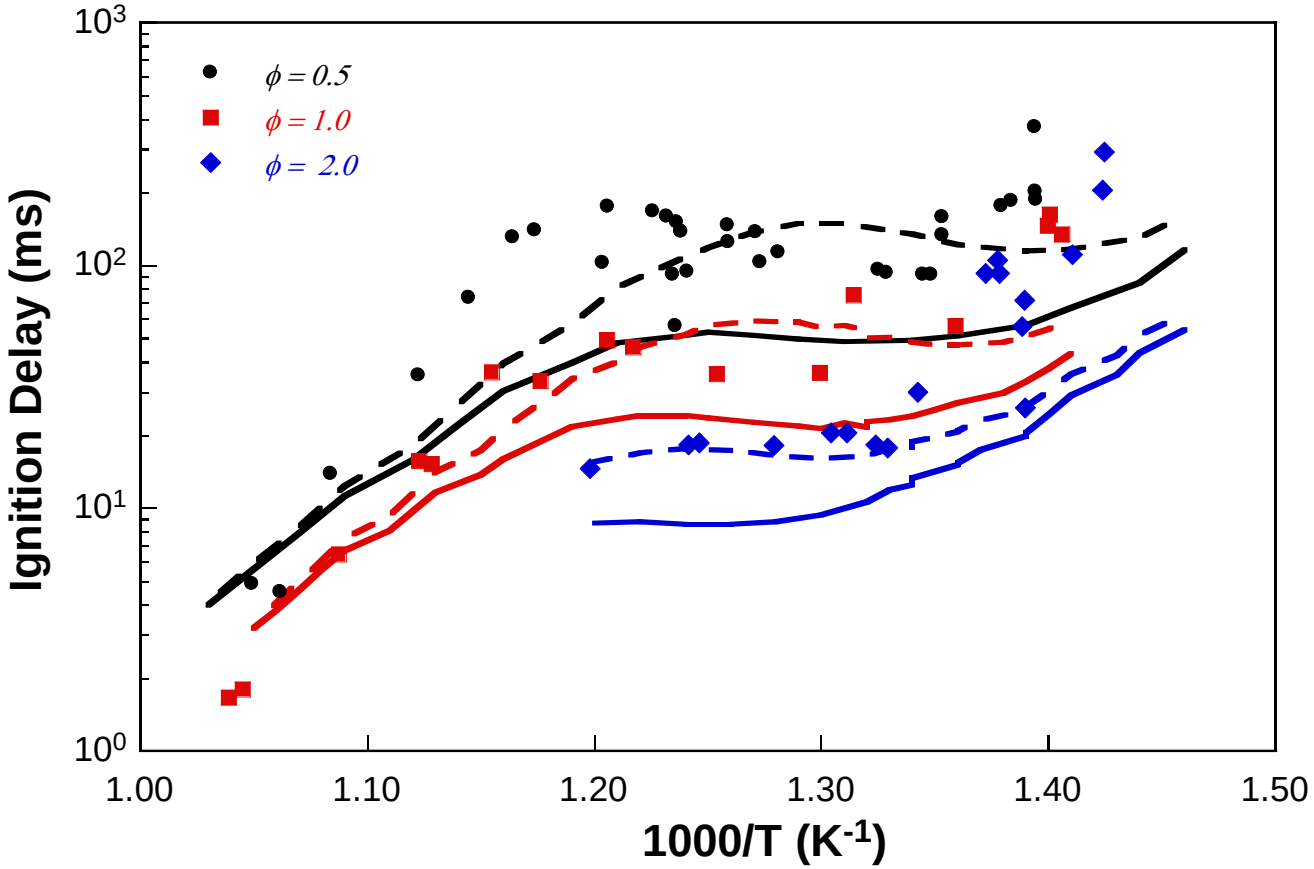

Figure S16. Experimental [8] propane RCM data in "air" (see descriptions in original text) compared with the model constructed in this work for varying ϕ. Solid lines: tuned model, as discussed in text; dashed lines: original model. Data simulated using the CONV approach.

Shown in Figure S16 are ignition delay time comparisons using the original and modified models of this work with the experimental data of Gallagher et al. [8]. In the work of Gallagher et al., the authors model their data using two methods – by accounting for heat losses through the RCM walls in a similar manner as performed in the RCM experiments of this work, and a more detailed multi-zone model which additionally includes geometry specific thermal boundary layer effects. Neither approach was not attempted here because pressure-traces of all unreactive mixtures are not provided in the original publication, nor could the supporting information be found. Therefore, only CONV simulations were performed. It is clear from Figure S16 that the changes to the two propane-related reactions which were tuned in this work decrease predicted ignition delay times in the NTC region. Recall these changes were made to improve agreement with the RCM data taken in this work, as the original model overestimates the ignition delay times. Although the predicted delay times are within a factor of three of the experimental data above 740 K, simulations incorporating heat loss through the RCM walls are expected to result in longer ignition delay times, and therefore better agreement with the experimental data of Gallagher et al. [8].

B. Jet-Stirred Reactor

1. Dagaut et al. 1996

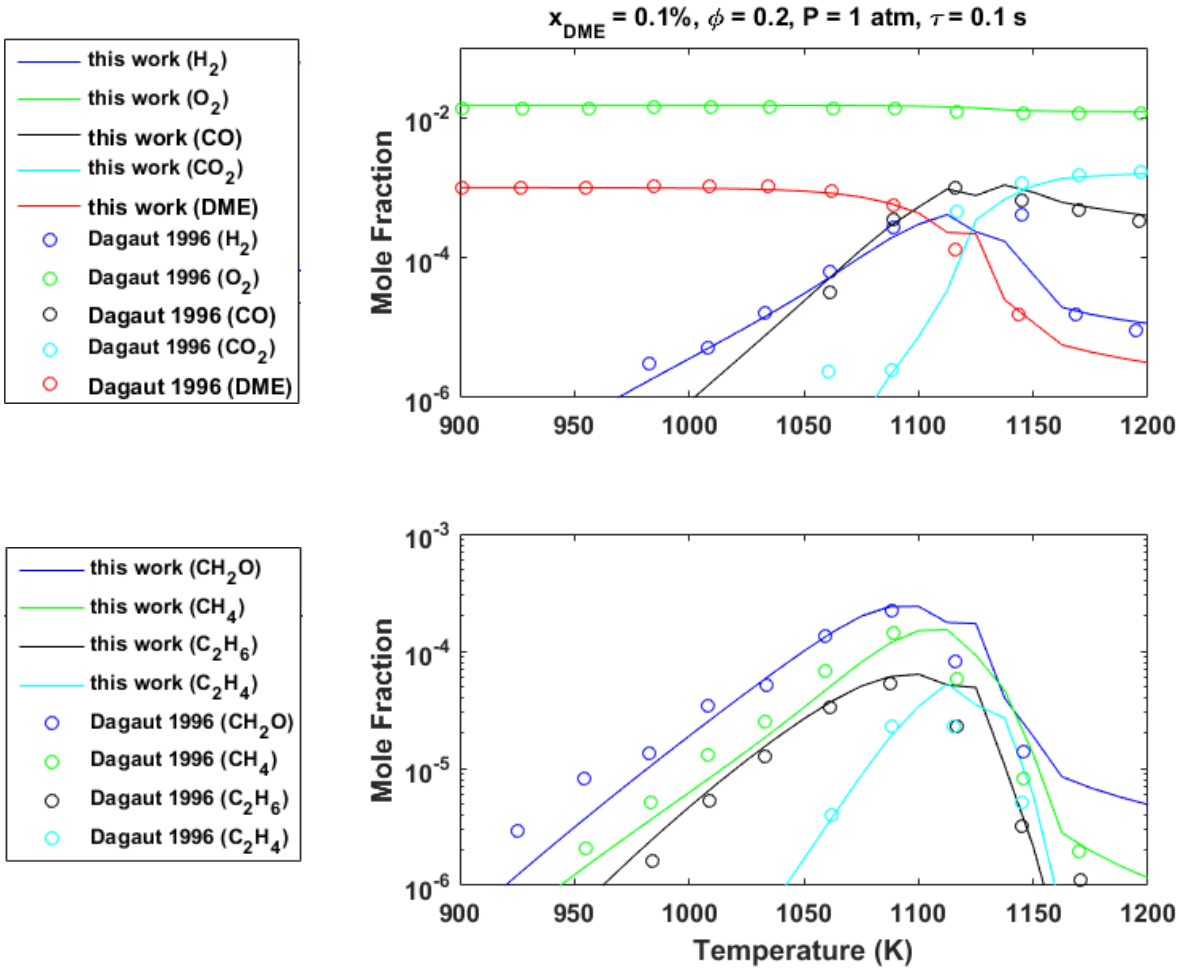

Figure S17. Species profile data for the Dagaut et al. 1996 *[9]* jet-stirred reactor conditions of 0.1% DME, 1.5% O_2 (ϕ = 0.2) in N_2 at 1 atm, and residence time of 0.1 s. The mole fractions shown in the top panel are H_2 (blue), O_2 (green), CO (black), CO_2 (cyan), and DME (red); the mole fractions shown in the bottom panel are CH_2O (blue), CH_4 (green), C_2H_6 (black), and C_2H_4 (cyan). The experimental data is plotted as open symbols, and the simulated data using the model from this work is shown as solid lines.

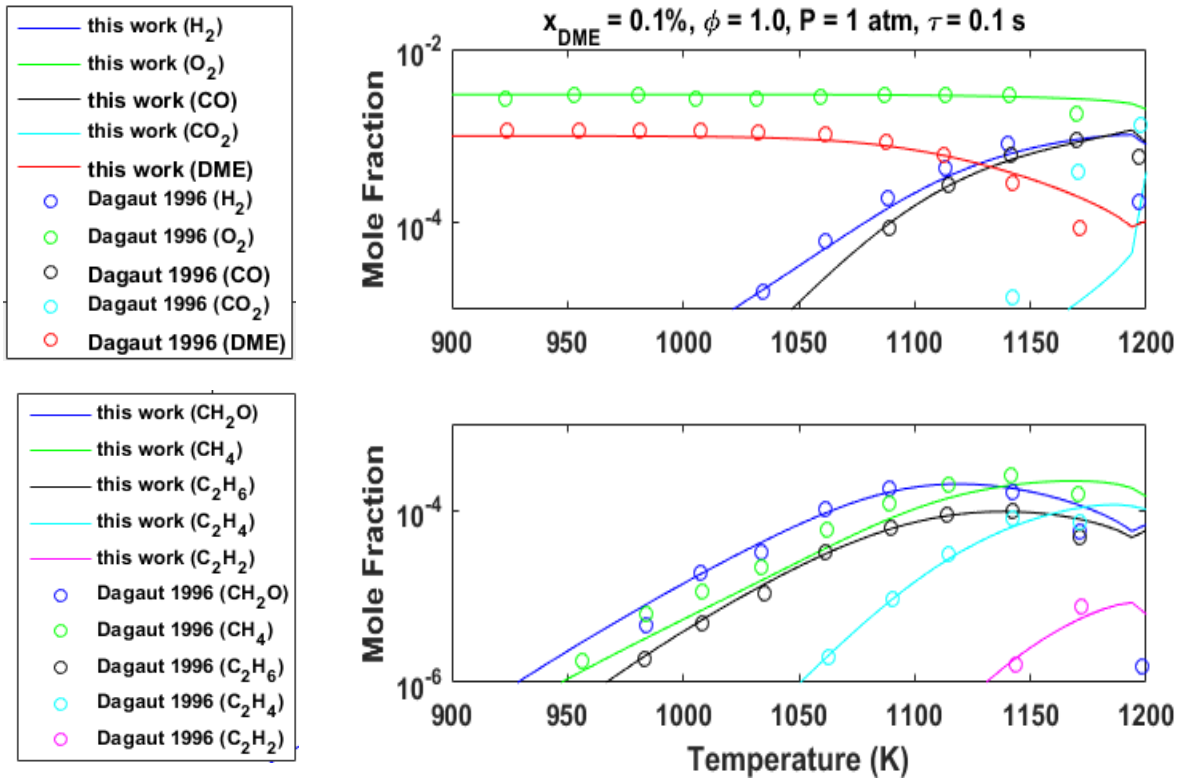

Figure S18. Species profile data for the Dagaut et al. 1996 *[9]* jet-stirred reactor conditions of 0.1% DME, 0.3% O_2 (ϕ = 1) in N_2 at 1 atm, and residence time of 0.1 s. The mole fractions shown in the top panel are H_2 (blue), O_2 (green), CO (black), CO_2 (cyan), and DME (red); the mole fractions shown in the bottom panel are CH_2O (blue), CH_4 (green), C_2H_6 (black), C_2H_4 (cyan), and C_2H_2 (pink). The experimental data is plotted as open symbols, and the simulated data using the model from this work is shown as solid lines.

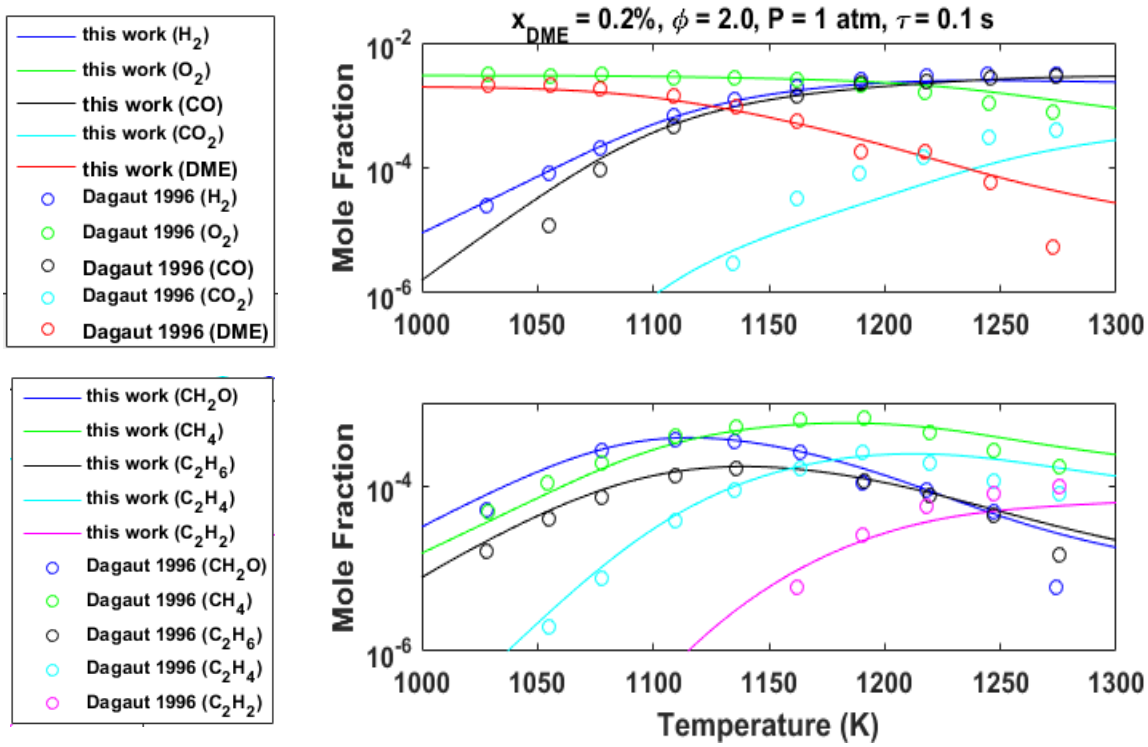

Figure S19. Species profile data for the Dagaut et al. 1996 *[9]* jet-stirred reactor conditions of 0.2% DME, 0.3% O_2 (ϕ = 2) in N_2 at 1 atm, and residence time of 0.1 s. The mole fractions shown in the top panel are H_2 (blue), O_2 (green), CO (black), CO_2 (cyan), and DME (red); the mole fractions shown in the bottom panel are CH_2O (blue), CH_4 (green), C_2H_6 (black), C_2H_4 (cyan), and C_2H_2 (pink). The experimental data is plotted as open symbols, and the simulated data using the model from this work is shown as solid lines.

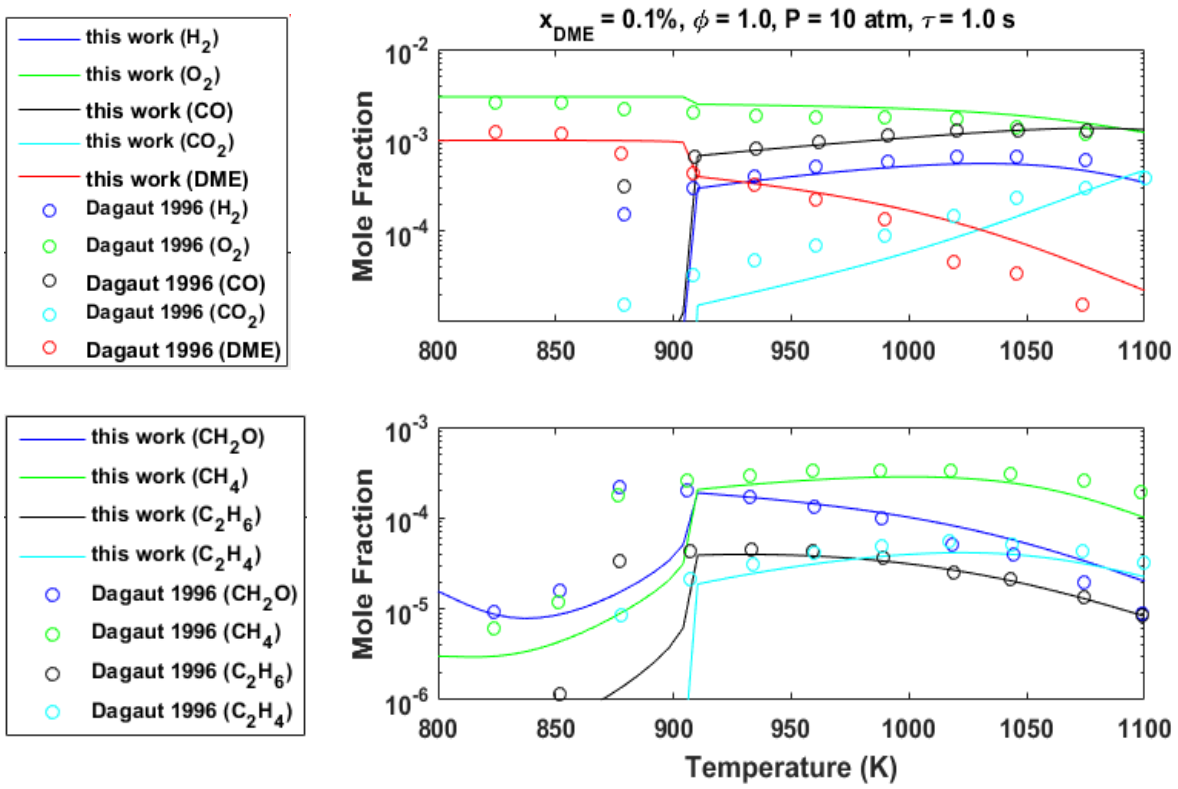

Figure S20. Species profile data for the Dagaut et al. 1996 *[9]* jet-stirred reactor conditions of 0.1% DME, 0.3% O_2 (ϕ = 1) in N_2 at 10 atm, and residence time of 1.0 s. The mole fractions shown in the top panel are H_2 (blue), O_2 (green), CO (black), CO_2 (cyan), and DME (red); the mole fractions shown in the bottom panel are CH_2O (blue), CH_4 (green), C_2H_6 (black), and C_2H_4 (cyan). The experimental data is plotted as open symbols, and the simulated data using the model from this work is shown as solid lines.

2. Dagaut et al. 1998

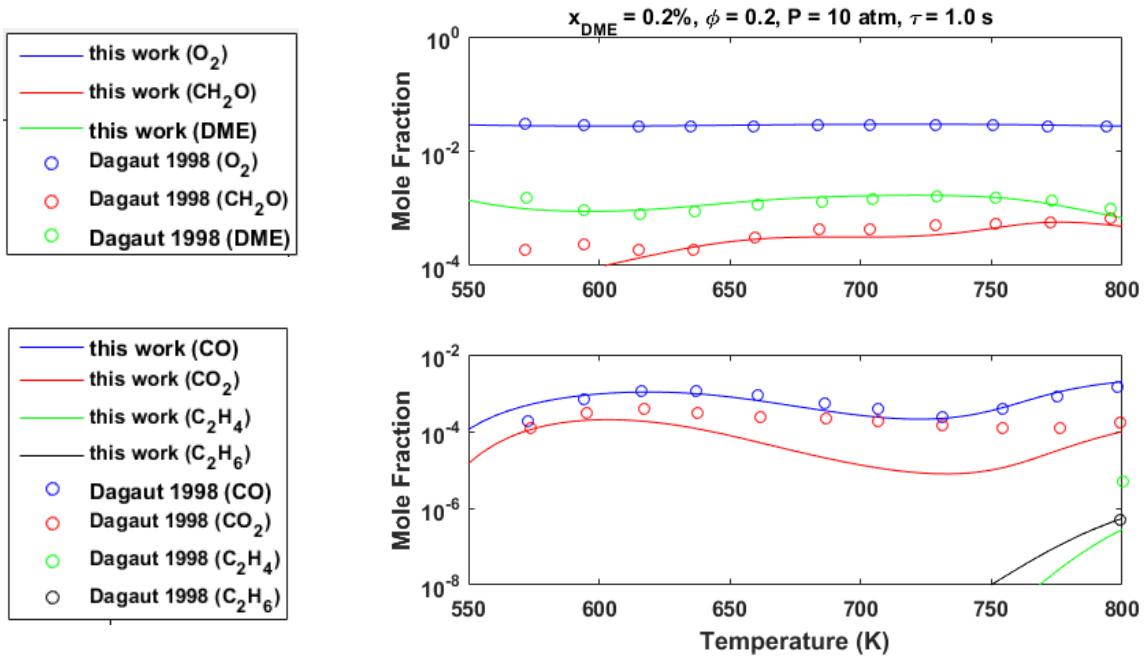

Figure S21. Species profile data for the Dagaut et al. 1998 *[2]* jet-stirred reactor conditions of 0.2% DME, 3% O_2, and an equivalence ratio of ϕ = 0.2, pressure of 10 atm, and residence time of 1.0 s. The mole fractions shown in the top panel are O_2 (blue), CH_2O (red), and DME (green); the mole fractions shown in the bottom panel are CO (blue), CO_2 (red), C_2H_4 (green), and C_2H_6 (black). The experimental data is plotted as open symbols, and the simulated data using the model from this work is shown as solid lines.

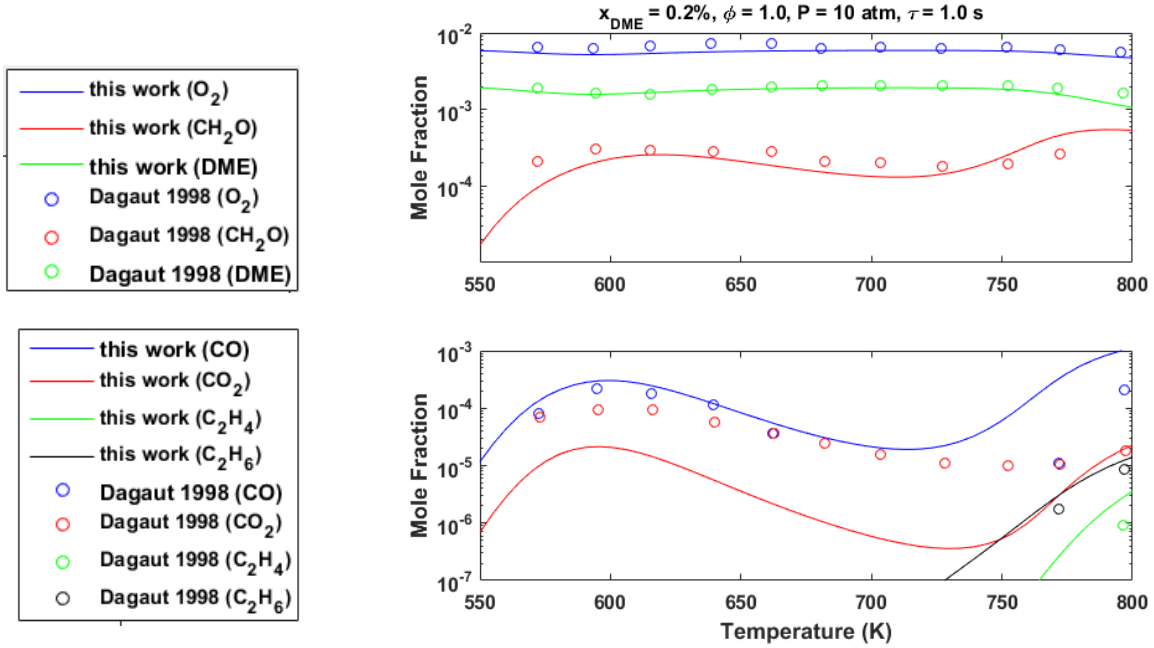

Figure S22. Species profile data for the Dagaut et al. 1998 *[2]* jet-stirred reactor conditions of 0.2% DME, 0.6% O_2, an equivalence ratio of ϕ = 1.0, pressure of 10 atm, and residence time of 1.0 s. The mole fractions shown in the top panel are O_2 (blue), CH_2O (red), and DME (green); the mole fractions shown in the bottom

panel are CO (blue), CO_2 (red), C_2H_4 (green), and C_2H_6 (black). The experimental data is plotted as open symbols, and the simulated data using the model from this work is shown as solid lines.

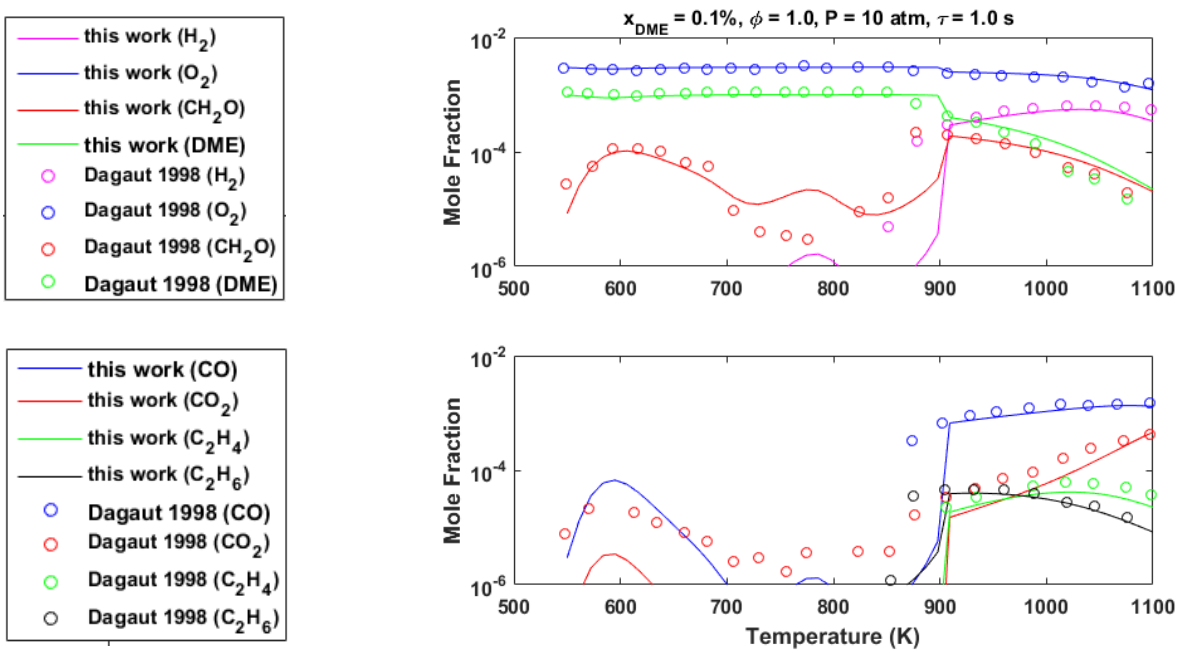

Figure S23. Species profile data for the Dagaut et al. 1998 *[2]* jet-stirred reactor conditions of 0.1% DME, 0.3% O_2, an equivalence ratio of ϕ = 1.0, pressure of 10 atm, and residence time of 1.0 s. The mole fractions shown in the top panel are H_2 (pink), O_2 (blue), CH_2O (red), and DME (green); the mole fractions shown in the bottom panel are CO (blue), CO_2 (red), C_2H_4 (green), and C_2H_6 (black). The experimental data is plotted as open symbols, and the simulated data using the model from this work is shown as solid lines.

3. Rodriguez et al. 2015

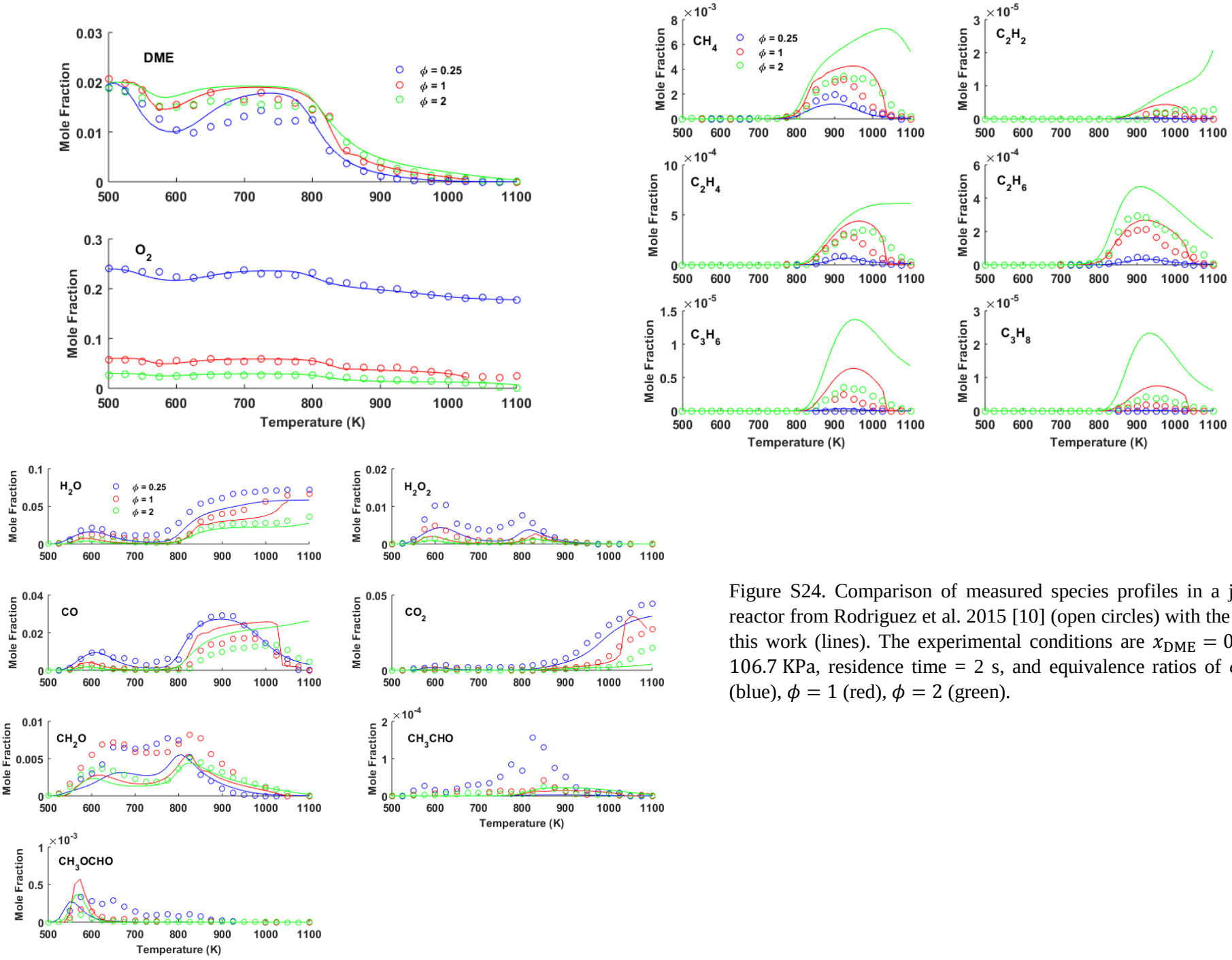

Figure S24. Comparison of measured species profiles in a jet-stirred reactor from Rodriguez et al. 2015 [10] (open circles) with the model in this work (lines). The experimental conditions are $x_{\mathrm{DME}} = 0.02$, $P =$ 106.7 KPa, residence time = 2 s, and equivalence ratios of $\phi = 0.25$ (blue), $\phi = 1$ (red), $\phi = 2$ (green).

C. Rapid Compression Machine

1. Mittal et al. 2008

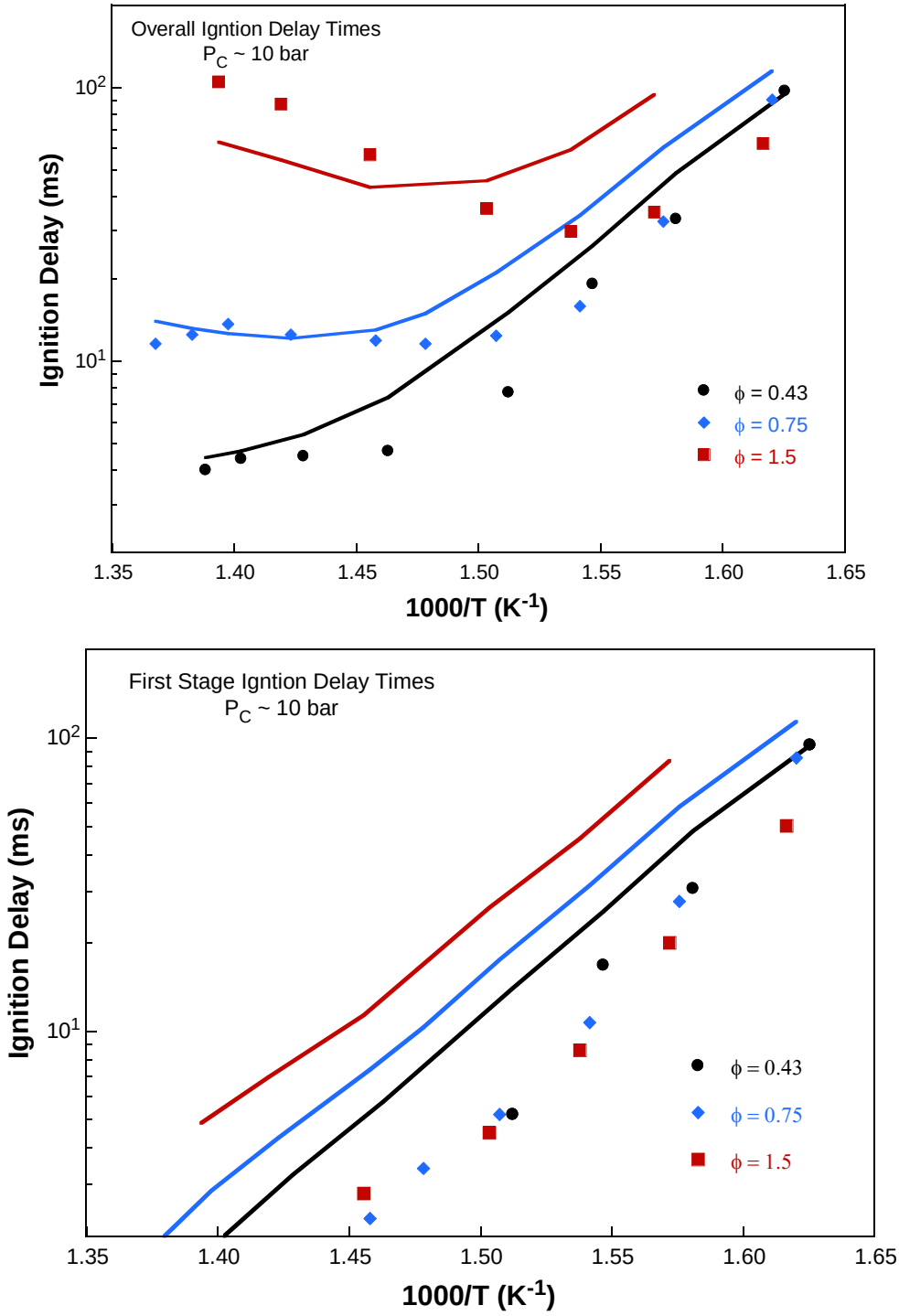

Figure S25. Ignition delay time data for the Mittal et al. 2008 *[11]* rapid compression machine conditions of DME mixtures at P = 10 bar and varying equivalence ratios of ϕ = 0.43 (black), ϕ = 0.75 (blue), and ϕ = 1.5 (red). The experimental data is plotted as open symbols, and the simulated data using the model from this work is shown as solid lines.

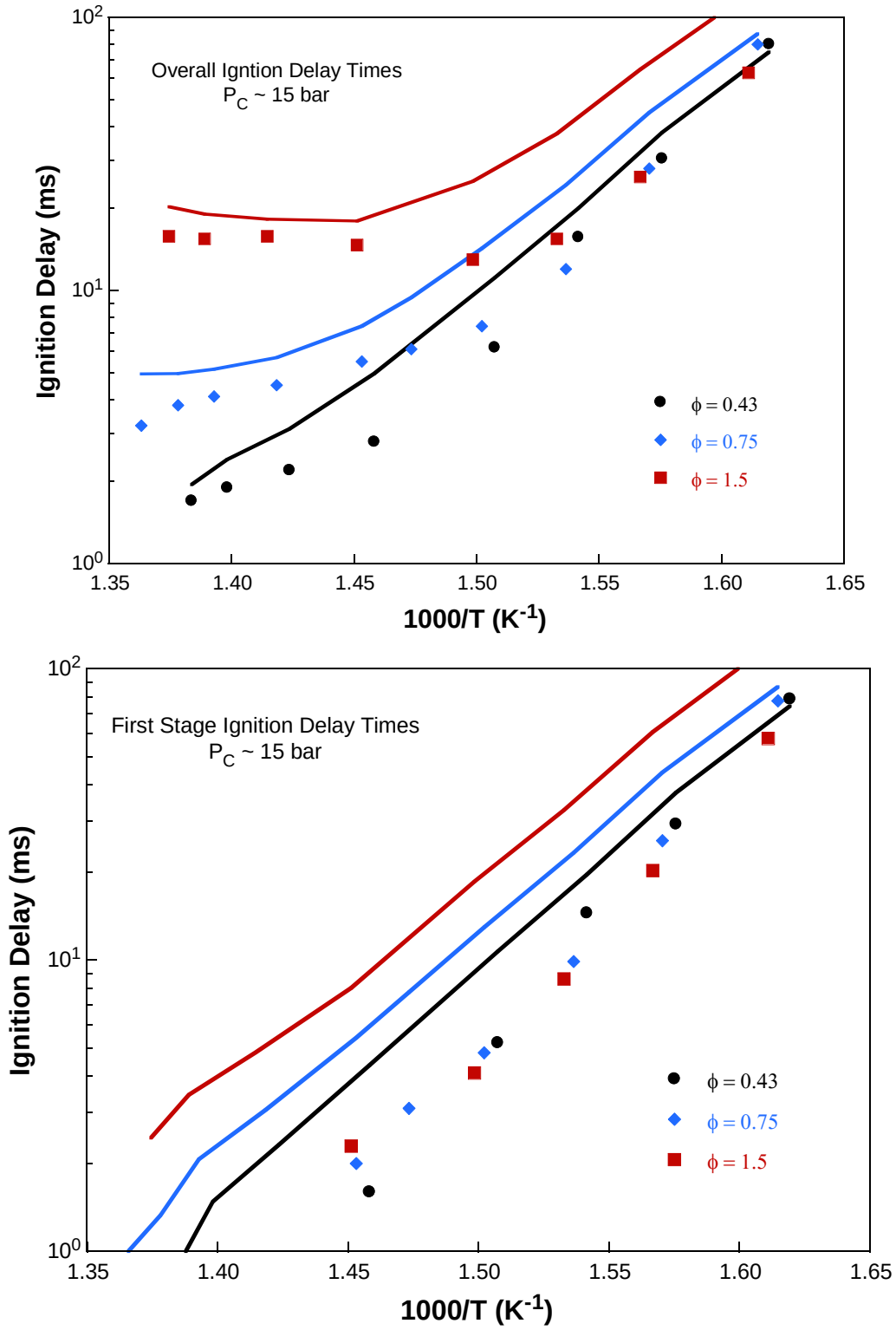

Figure S26. Ignition delay time data for the Mittal et al. 2008 *[11]* rapid compression machine conditions of DME mixtures at P = 15 bar and varying equivalence ratios of ϕ = 0.43 (black), ϕ = 0.75 (blue), and ϕ = 1.5 (red). The experimental data is plotted as open symbols, and the simulated data using the model from this work is shown as solid lines.

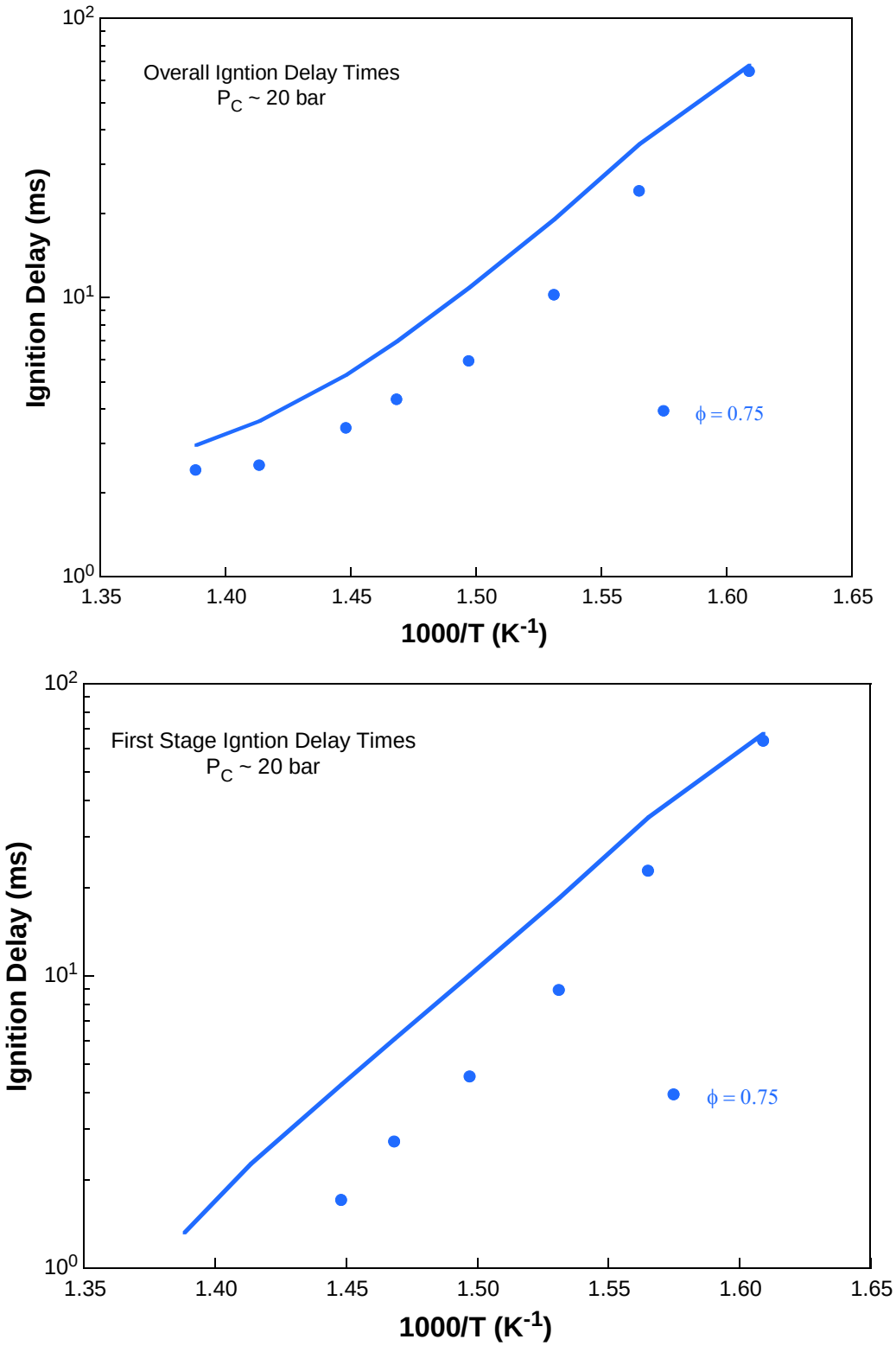

Figure S27. Ignition delay time data for the Mittal et al. 2008 *[11]* rapid compression machine conditions of DME mixtures at P = 20 bar and an equivalence ratio of ϕ = 0.75 (blue). The experimental data is plotted as open symbols, and the simulated data using the model from this work is shown as solid lines.

2. Burke et al. 2015

See Section II.A.7

3. RCM data of this work

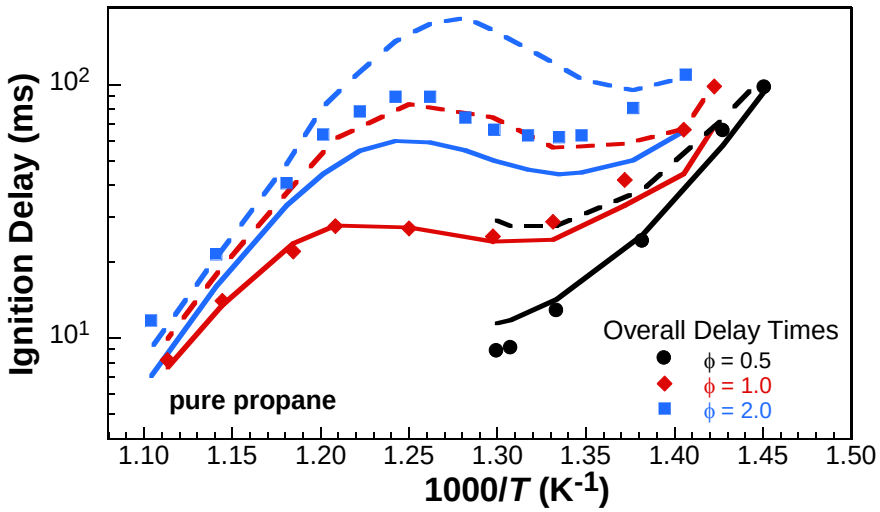

Figure S28. . Experimental propane RCM data (closed symbols: $\boldsymbol{\tau}$, open symbols: $\boldsymbol{\tau_1}$) compared with the model constructed in this work for varying $\boldsymbol{\phi}$. See **Error! Reference source not found.** for mixture compositions. Solid lines: current model; dashed lines: model before rate adjustments. Predictions only span the temperature range of the experimental data because experimental pressure traces are used in simulations; see text for discussion.

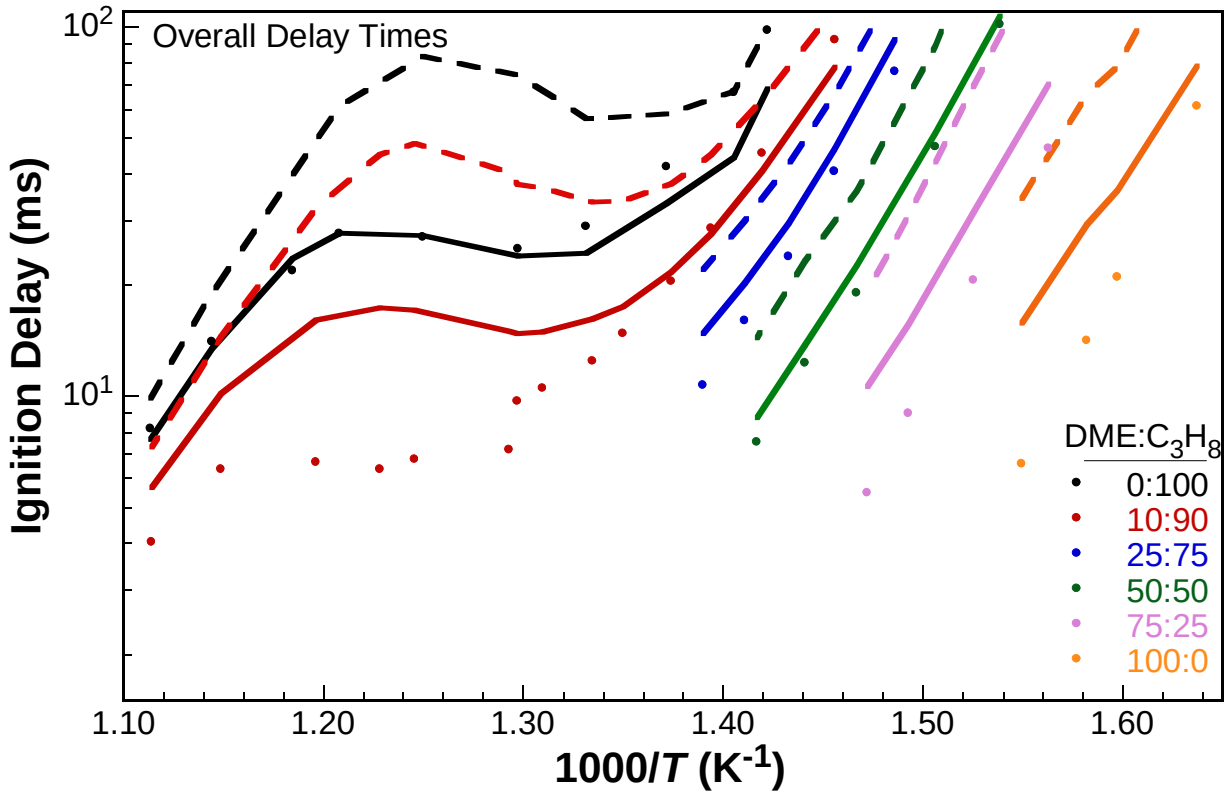

Figure S29. Comparison of RCM data with the model in this work for varying DME/propane blend ratios (P_C~ 30 bar, $\phi = 1.0$). Blending ratio is defined within plot; solid lines: simulations of overall ignition delay with final model of this work; dashed lines: model before rate adjustments.

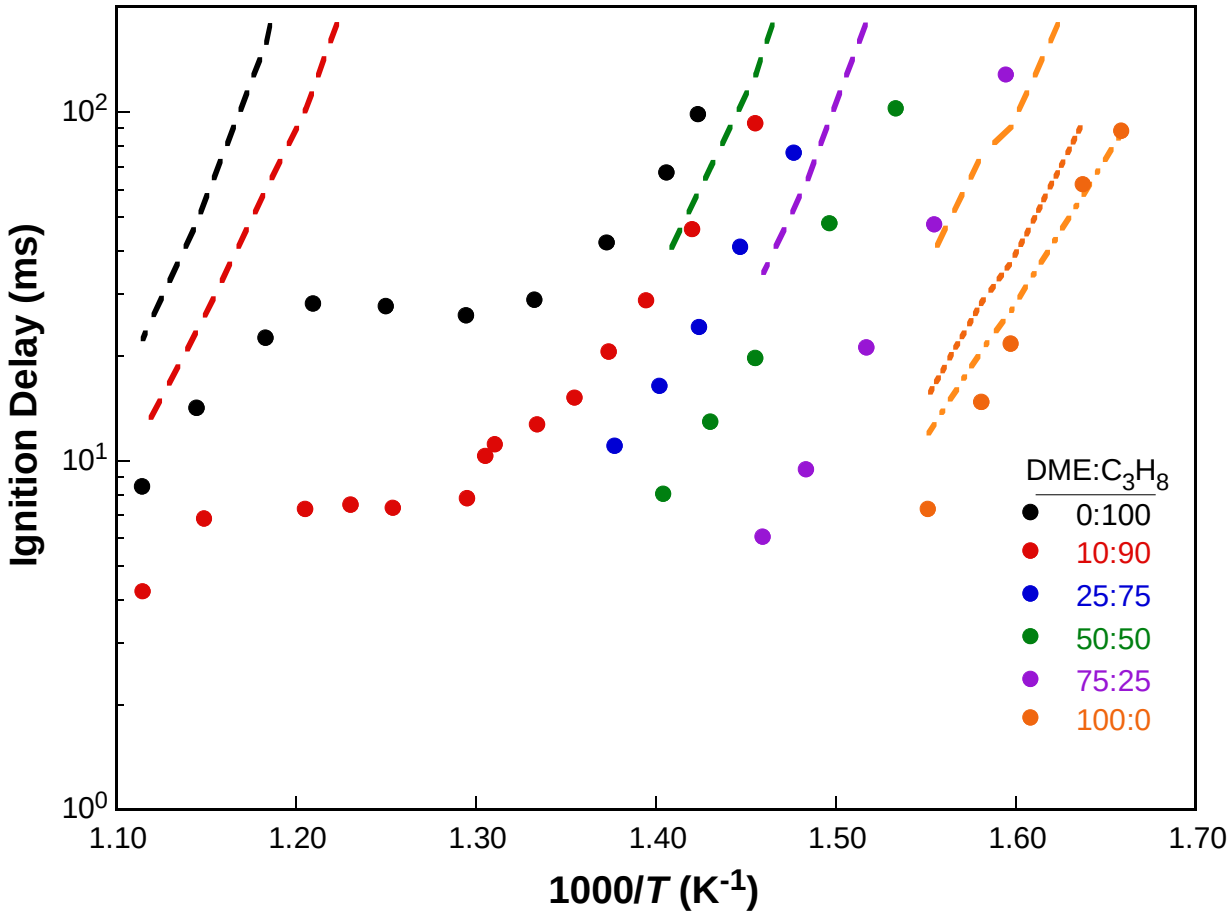

Figure S30. Comparison of RCM data (solid circles) with other mechanisms available in the literature for $P_{comp} \approx 30$ bar and $\phi = 1$. The DME:propane ratios are the following: 0:100 (black), 10:90 (red), 25:75 (blue), 50:50 (green), 75:25 (purple), 100:0 (orange). The dashed lines represent simulations using the model from Rodriguez et al. [10] for varying DME/propane blend ratios. The 25:75 DME:propane simulation using the Rodriguez et al. mechanism is not shown on the plot due to the particularly high predicted ignition delay times (e.g., at $1000/T = 1.38$, the value of τ is 836 ms). Simulations using the mechanisms from Liu et al. [12] (dotted lines) and Wang et al. [13] (dot-dash lines) are performed only for pure DME (i.e., 100:0) since the mechanisms do not contain the necessary propane chemistry.

D. Premixed Flame

1. Liu et al. 2013

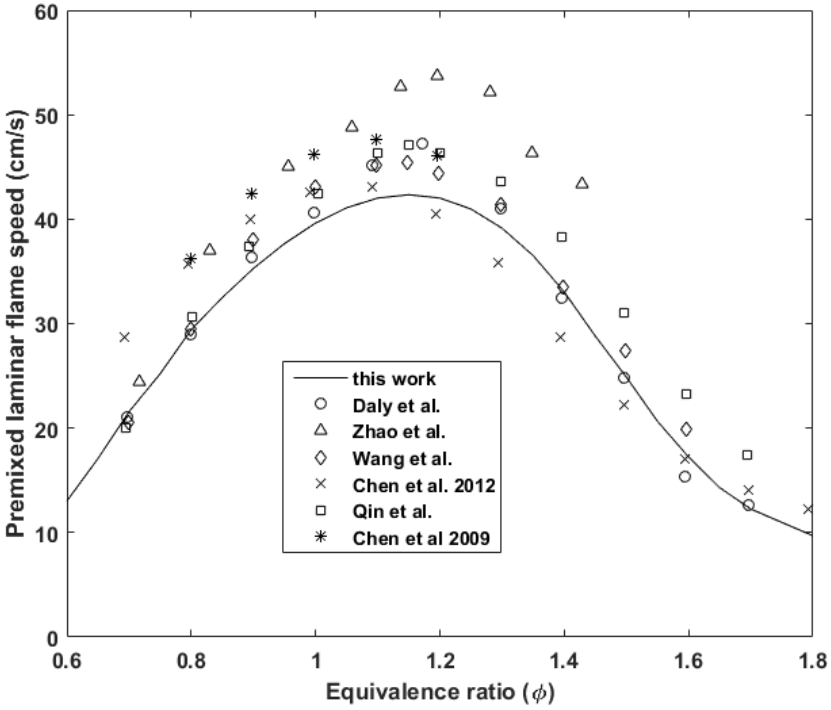

Figure S31. Premixed laminar flame speeds as a function of equivalence ratio for a mixture of DME/air at 1.01 bar. The experimental data is plotted as symbols, and the simulated data using the model from this work is shown as a solid line. The circles are from Daly et al. [14], the triangles are from Zhao et al. [15], the diamonds are from Wang et al. [16], the x's are from Chen et al. [17], the squares are from Qin et al. [18], and the *'s are from Chen et al. [19].

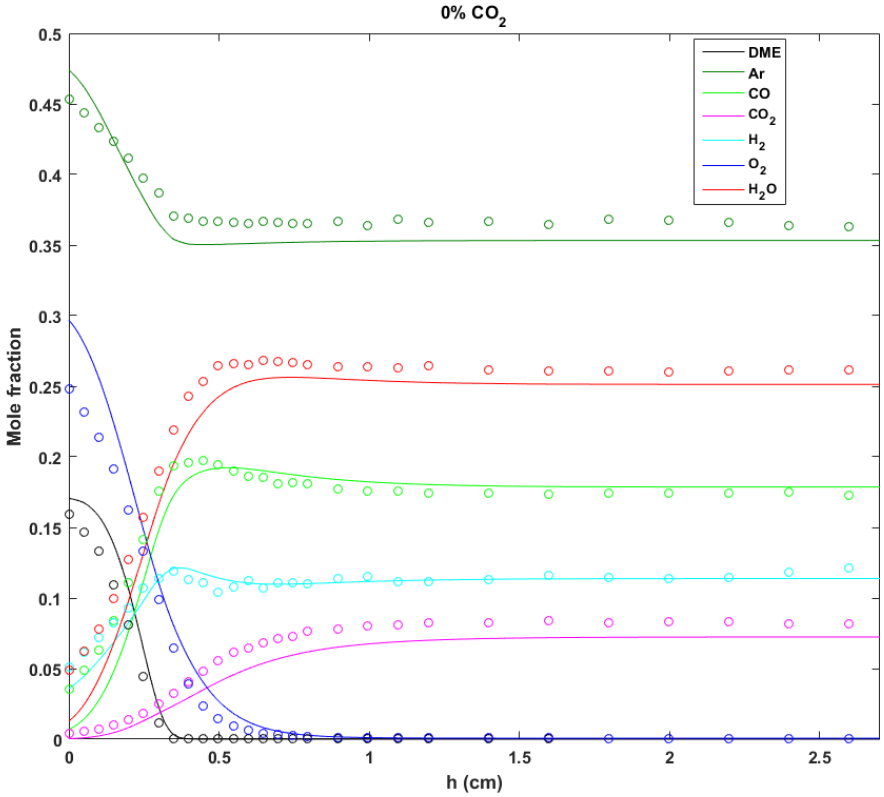

Figure S32. Species mole fraction data as a function of height for the Liu et al. 2013 *[12]* burner-stabilized DME flame conditions P = 50 mbar, equivalence ratio of ϕ = 1.63, 50% dilution in Ar, and an unburned gas temperature of 298 K. The experimental data is plotted as open symbols, and the simulated data using the model from this work is shown as solid lines.

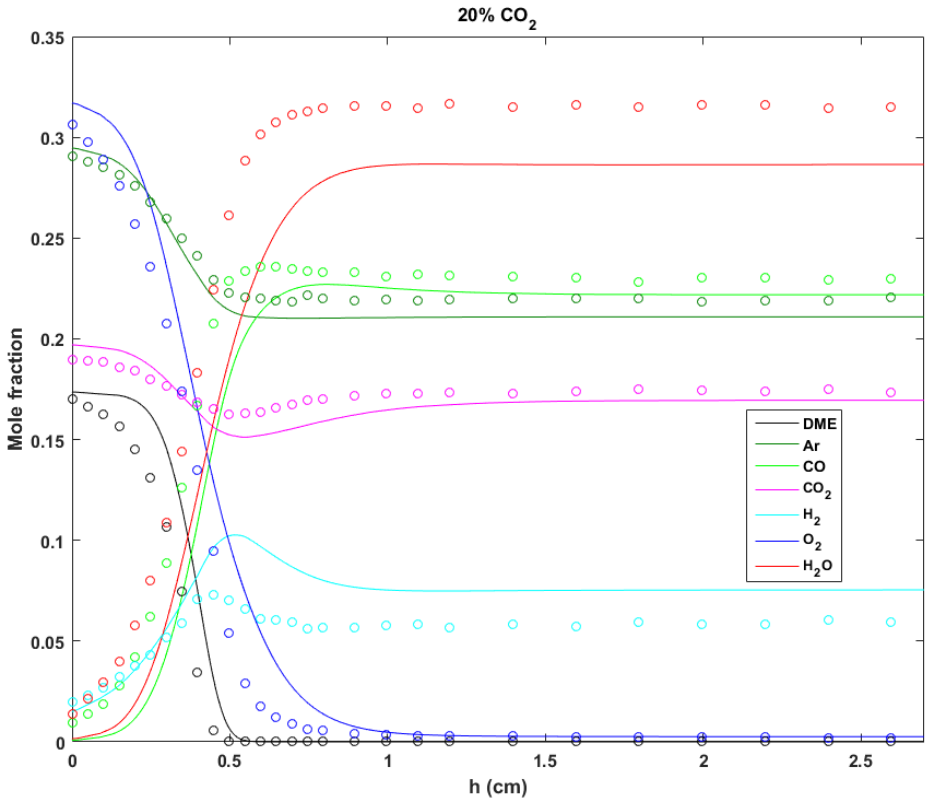

Figure S33. Species mole fraction data as a function of height for the Liu et al. 2013 *[12]* burner-stabilized DME flame conditions P = 50 mbar, equivalence ratio of ϕ = 1.63, 50% dilution in 20% CO_2 and 30% Ar, and an unburned gas temperature of 298 K. The experimental data is plotted as open symbols, and the simulated data using the model from this work is shown as solid lines.

II. References

[1] Pfahl U, Fieweger K, Adomeit G. Self-ignition of diesel-relevant hydrocarbon-air mixtures under engine conditions. vol. 26, Elsevier; 1996, p. 781–9.

[2] Dagaut P, Daly C, Simmie JM, Cathonnet M. The oxidation and ignition of dimethylether from low to high temperature (500–1600 K): Experiments and kinetic modeling. vol. 27, Elsevier; 1998, p. 361–9.

[3] Cook RD, Davidson DF, Hanson RK. Shock tube measurements of ignition delay times and OH time-histories in dimethyl ether oxidation. Proc Combust Inst 2009;32:189–96.

[4] Tang C, Wei L, Zhang J, Man X, Huang Z. Shock Tube Measurements and Kinetic Investigation on the Ignition Delay Times of Methane/Dimethyl Ether Mixtures. Energy Fuels 2012;26:6720–8.

[5] Pyun SH, Ren W, Lam K-Y, Davidson DF, Hanson RK. Shock tube measurements of methane, ethylene and carbon monoxide time-histories in DME pyrolysis. Combust Flame 2013;160:747–54.

[6] Pan L, Hu E, Zhang J, Zhang Z, Huang Z. Experimental and kinetic study on ignition delay times of DME/H2/O2/Ar mixtures. Spec Issue Altern Fuels 2014;161:735–47. doi:10.1016/j.combustflame.2013.10.015.

[7] Burke U, Somers KP, O'Toole P, Zinner CM, Marquet N, Bourque G, et al. An ignition delay and kinetic modeling study of methane, dimethyl ether, and their mixtures at high pressures. Combust Flame 2015;162:315–30.

[8] Gallagher S, Curran H, Metcalfe W, Healy D, Simmie J, Bourque G. A rapid compression machine study of the oxidation of propane in the negative temperature coefficient regime. Combust Flame 2008;153:316–33.

[9] Dagaut P, Boettner J-C, Cathonnet M. Chemical kinetic study of dimethylether oxidation in a jet stirred reactor from 1 to 10 ATM: Experiments and kinetic modeling. vol. 26, Elsevier; 1996, p. 627–32.

[10] Rodriguez A, Frottier O, Herbinet O, Fournet R, Bounaceur R, Fittschen C, et al. Experimental and Modeling Investigation of the Low-Temperature Oxidation of Dimethyl Ether. J Phys Chem A 2015.

[11] Mittal G, Chaos M, Sung C-J, Dryer FL. Dimethyl ether autoignition in a rapid compression machine: Experiments and chemical kinetic modeling. Fuel Process Technol 2008;89:1244–54.

[12] Liu D, Santner J, Togbé C, Felsmann D, Koppmann J, Lackner A, et al. Flame structure and kinetic studies of carbon dioxide-diluted dimethyl ether flames at reduced and elevated pressures. Combust Flame 2013;160:2654–68.

[13] Wang Z, Zhang X, Xing L, Zhang L, Herrmann F, Moshammer K, et al. Experimental and kinetic modeling study of the low-and intermediate-temperature oxidation of dimethyl ether. Combust Flame 2015;162:1113–25.

[14] Daly CA, Simmie JM, Würmel J, DjebaÏli N, Paillard C. Burning velocities of dimethyl ether and air. Combust Flame 2001;125:1329–40. doi:10.1016/S0010-2180(01)00249-8.

[15] Zhao Z, Kazakov A, Dryer FL. Measurements of dimethyl ether/air mixture burning velocities by using particle image velocimetry. Combust Flame 2004;139:52–60. doi:10.1016/j.combustflame.2004.06.009.

[16] Wang YL, Holley AT, Ji C, Egolfopoulos FN, Tsotsis TT, Curran HJ. Propagation and extinction of premixed dimethyl-ether/air flames. Proc Combust Inst 2009;32:1035–42. doi:10.1016/j.proci.2008.06.054.

[17] Chen Z, Tang C, Fu J, Jiang X, Li Q, Wei L, et al. Experimental and numerical investigation on diluted DME flames: Thermal and chemical kinetic effects on laminar flame speeds. Spec Sect ACS Clean Coal 2012;102:567–73. doi:10.1016/j.fuel.2012.06.003.

[18] Qin X, Ju Y. Measurements of burning velocities of dimethyl ether and air premixed flames at elevated pressures. Proc Combust Inst 2005;30:233–40.

[19] Chen Z, Wei L, Huang Z, Miao H, Wang X, Jiang D. Measurement of laminar burning velocities of dimethyl ether− air premixed mixtures with N2 and CO2 dilution. Energy Fuels 2009;23:735–9.